DEVELOPMENT AND INVESTIGATION OF ELECTROCHEMICAL PROPERTIES OF LEAN DUPLEX STAINLESS STEEL ALLOYS

BY

FARID MUNIR ABDALLAH

A Thesis Presented to the
DEANSHIP OF GRADUATE STUDIES

KING FAHD UNIVERSITY OF PETROLEUM & MINERALS

DHAHRAN, SAUDI ARABIA

In Partial Fulfillment of the
Requirements for the Degree of

MASTER OF SCIENCE

In

MATERIAL SCIENCE AND ENGINEERING

MAY 2017

KING FAHD UNIVERSITY OF PETROLEUM & MINERALS

DHAHRAN- 31261, SAUDI ARABIA

DEANSHIP OF GRADUATE STUDIES

This thesis, written by **FARID MUNIR ABDALLAH** under the direction his thesis advisor and approved by his thesis committee, has been presented and accepted by the Dean of Graduate Studies, in partial fulfillment of the requirements for the degree of **MASTER OF SCIENCE IN MATERIALS SCIENCE & ENGINEERING**

Dr. IHSAN UL HAQ TOOR
(Advisor)

Dr. ZUHAIR M. GASEM
Department Chairman

Dr. ZUHAIR M. GASEM
(Member)

Dr. Salam A. Zummo
Dean of Graduate Studies

Dr. SAHEB NOUARI
(Member)

30/11/17

Date

*This work is dedicated to my beloved parents (****Munir Abdallah & Naila Munir****) who gave me knowledge and teach me to have big ambitions and pursue big dreams in my early childhood. Since the day they left us (may ALLAH have mercy on them and grant them forgiveness) their words and teachings have been my assets which bring the best of me and drive me to have big ambitions always in my life.*

ACKNOWLEDGMENTS

I would like to put my foremost praise to Allah Almighty for giving me the chance and courage to accomplish my Ms. Studies. May peace and blessings be upon our beloved Prophet Mohammad (pbuh).

Firstly, my sincere appreciation and gratitude go to my advisor Dr. Ihsan ul-Haq Toor for his support, patience, motivation, and advice during my Master's studies and research works. His supervision and guidance helped me to learn and accomplish my research works and in thesis writing. Besides my advisor, I would like to thank Dr. Zuhair Gasem who showed his support and guidance since I joined Ms. Program as a Chairman of Mechanical engineering department as well as my thesis committee member. I would also like to thank Dr. Saheb Nouari, for his insightful comments, advice, and encouragement in my research. I am grateful to Mechanical Engineering department and KFUPM for giving me a chance to pursue my Ms. Program in the Kingdom of Saudi Arabia.

My sincere thanks also go to Mr.Latif Hashmi (Material laboratory technician) and Junaid Ahmed (a senior student), who helped me in laboratory works and taught me different techniques used for the accomplishment of my research. I would also like to appreciate the help of my closest friends Abdi Talib, Ahmed Hassan, Mohamed Alasow, Ibrahim Momohjimo, Sharif Adeniy, Adil Eliyar and Abdulhakim Bake who through their company and discussions I was able to carry out my research smoothly. Also, my thanks go to all friends from East Africa, Ghana, Nigerian, Pakistan and Sudanese communities. I would also like to thank and express my deep and profound gratitude to my beloved parents, my wife, my guardian uncles, and aunts, my brother and sister for supporting me mentally, emotionally and spiritually throughout my education and my life in general.

TABLE OF CONTENTS

RESULTS AND DISCUSSION

CHAPTER 6 POWDER METALLURGY DUPLEX STAINLESS STEEL …………………….79

LIST OF TABLES

LIST OF FIGURES

LIST OF ABBREVIATIONS

DSS	:	Duplex Stainless steel
PM	:	Powder Metallurgy
SSs	:	Stainless Steels
MA	:	Mechanical Alloying
B.P.R	:	Ball to powder ratio
RPM	:	Revolution per min
XRD	:	X-ray diffraction
SEM	:	Scanning electron microscope
BS-SEM	:	Backscattered SEM
FE-SEM	:	Field emission SEM
SCE	:	Saturated calomel electrode
PDP	:	Potentiodynamic polarization
LPR	:	Linear polarization resistance
EIS	:	Electrochemical impedance spectroscopy
ENA	:	Electrochemical noisy analysis
E_{corr}	:	Corrosion potential
i_{corr}	:	Corrosion current density
E_{pit}	:	Pitting potential
i_{pass}	:	Passive current density
XPS	:	X-ray photoelectron spectroscopy

SBF : Simulated body fluid

ABSTRACT

Full Name : [FARID MUNIR ABDALLAH]

Thesis Title : **[DEVELOPMENT AND INVESTIGATION OF ELECTROCHEMICAL PROPERTIES OF LEAN DUPLEX STAINLESS STEEL ALLOYS]**

Major Field : [Master in Material Science and Engineering]

Date of Degree : [May 2017]

Duplex stainless steels (DSS) are commonly used stainless steel’s material in many industrial applications owing to their outstanding mechanical and corrosion properties in contrary to their counterpart ferritic and austenitic stainless steels. Recently the development in DSS has mainly focused on economizing its production without the expense of their outstanding properties. Nickel is an alloying element for SS which improves its corrosion resistance, however, its price volatility is the main concern. Therefore, Nickel has been replaced by Manganese and Nitrogen which are also austenite forming elements in DSS without compromising the precipitation of intermetallic phases such as Sigma, Chi, MnS and nitride compounds which are detrimental to corrosion and mechanical properties. Through controlling and optimization of alloying elements while selecting appropriate processing parameters will be able to improve and successfully enable to produce a DSS with better mechanical and corrosion properties at a lower cost through casting and powder metallurgy technique.

In this work, we investigated the electrochemical properties of cast and sintered DSS alloys. The cast alloys were developed in a vacuum melting furnace while P/M DSS alloys were developed through a combination of mechanical alloying and spark plasma sintering technique.

The results showed that the corrosion properties of cast DSS alloys were similar in pitting corrosion resistance in both NaCl and H_2SO_4. The passive current density (i_{pass}) of Alloy 2

(Bal.Fe-18Cr-5Mn-1Mo-1Si-1Cu-0.22N) showed lower value than other DSS alloys. There was no much difference in corrosion current density (i_{corr}), however, the corrosion potential (E_{corr}) of Alloy 2 and 304SS were higher than for other alloys. There was no much variation observed in critical current density (i_{crit}) for all alloys.

Further, results from simulated body fluid SBF showed that Alloy 2 and Alloy 3 (Bal.Fe-18Cr-4Mn-1Mo-1Si-2Cu-0.22N) of cast samples showed similar corrosion resistance properties in comparison to AISI 304SS. Further experiments on the effect of agitated condition at different rotation speeds (rpm) showed that, corrosion resistance properties such as pitting potential decreased with an increase in rotation speed probably due to the shear stresses acting on the passive film.

Phase evolution and powder morphology were studied during mechanical alloying. Microstructure characterization, hardness, density, temperature optimization during SPS and corrosion properties were further investigated for powder metallurgy prepared specimens. Temperature optimization was conducted on Alloy D2 (Bal.Fe-18Cr-6Mn-1Mo-1Si-1Cu-0.22N) at 900^{o}C, 950^{o}C and 1000^{o}C and a 1000^{o}C and Spark plasma sintering temperature was selected. The maximum percentage density achieved by P/M sample was 96.73% at 1000^{o}C sintering temperature compared to their respective theoretical values. The XRD spectra revealed the presence of sharp crystalline peaks of ferrite and austenitic phases and no secondary phases such as Sigma, Chi, and nitrides were observed.

Electrochemical properties of sintered alloys were investigated in 0.2M NaCl solution. In PDP, Alloy D4 (Bal.Fe-18Cr-3Mn-1Mo-1Si-0Cu-5Ni-0.22N) showed better corrosion properties such as higher pitting potential (E_{pit}) and higher polarization resistance due to higher Ni content. Alloy D2 showed active behavior due to the negative effect of Cu on its composition.

EIS results showed that Alloy D4 exhibited better polarization resistance than other Alloys. The polarization resistance values for the alloys were calculated by fitting the EIS spectra with an appropriate equivalent circuit.

ملخص الرسالة

الاسم الكامل:فريد منير عبدالله

عنوان الرسالة: تطويرودراسة الخصائص الكهروكيميائية لسبائك الفولاذ ذي الطورين

التخصص: ماجستير في علوم المواد والهندسة

تاريخ الدرجة العلمية: يونيو 2017

الفولاذ المقاوم للصدأ ذي الطورين يستخدم عادة في العديد من التطبيقات الصناعية بسبب خصائصه الميكانيكية المتميزة إلى جانب مقاومته للتآكل على عكس نظيره الفولاذ المقاوم للصدأ أحادي الطور. أبحاث تطويرالفولاذ المقاوم للصدأ ذي الطورين تركزت على الإقتصاد في عملية إنتاجه دون الإهتمام بخصائصه المتميزة. النيكل هو عنصر سبائكي للفولاذ المقاوم للصدأ، ويحسن بدوره مقاومة التآكل، ولكن تقلب أسعاره يظل الشاغل الرئيسي ، ولذلك تم استبدال النيكل بالمنجنيز والنيتروجين، التي هي أيضاً عناصر تشكيل الأوستنيت في الفولاذ المقاوم للصدأ، دون المساس بعملية ترسيب الأطوار السبائكية مثل: سيغما، تشي، كبريتيد المنجنيز ومركبات النيتريد التي تضر بالتآكل والخصائص الميكانيكية. من خلال التحكم والتحسين في عناصر السبائك، مع إختيار معاملات المعالجة المناسبة، يمكن إنتاج فولاذ مقاوم للصدأ ذي الطورين محسن وذو خواص ميكانيكية وتآكلية أفضل بتكلفة أقل من خلال عمليات السباكة ومسحوق المعادن.

في هذا العمل، قمنا بالتقصي عن الخصائص الكهروكيميائية لسبائك الفولاذ المقاوم للصدأ ذي الطورين. وقد تم تطوير السبائك في فرن ذوبان فراغي، في حين تم تطوير مسحوق الفولاذ المقاوم للصدأ ذي الطورين بإستخدام التلبيد عن طريق شرارة البلازما. أظهرت النتائج أن خصائص التآكل لسبائك الفولاذ المقاوم للصدأ ذي الطورين مشابهة لمقاومة التآكل التنقري في كل من كلوريد الصوديوم و حمض الكبريتيك. وجد أن كثافة التاكل للسبيكة الثانية المتكونة من (18كروم، 5 منجنيز، 1 ملبيديوم، 1 سيليكون، 1 نحاس، 0.22 نتروجين، والمتبقي حديد) أقل من سبائك الفولاذ المقاوم للصدأ ذي الطورين الأخرى. لذا لم يكن هناك فرق كبير في الكثافة الحالية للتآكل، ومع ذلك وجد أن إحتمالية التآكل للسبيكة الثانية وسبيكة SS304 أعلى من غيرهم من السبائك. ولم يكن هناك اختلاف كبير في الكثافة الحالية الحرجة لجميع السبائك. أظهرت نتائج محاكاة سائل الجسم للعينة من السبيكة الثانية والسبيكة الثالثة المتكونة من

(18كروم، 4 منجنيز، 1 ملبيديوم، 1 سيليكون، 2 نحاس، 0.22 نتروجين، والمتبقي حديد) أن خصائص مقاومة التآكل مشابهة لسبيكة الفولاذ المقاوم للصدأ ذي الطورين ذات النوع SS304. تم إجراء تجارب أخرى عن تأثير الظرف الحرج عند سرعات دوران مختلفة، وأظهرت النتائج أن خصائص مقاومة التآكل مثل إمكانية التنقر إنخفضت مع زيادة سرعة الدوران ربما بسبب إجهادات القص التي تعمل على الغشاء غير الفعال.

تم دراسة تحول الطور ومورفولوجيا المسحوق خلال عملية الخلط الميكانيكي. وتمت دراسة الخصائص المجهرية، والصلابة، والكثافة. تم إجراء نمذجة لدرجة الحرارة على السبيكة الثانية (د) المتكونة من (18كروم، 6 منجنيز، 1 ملبيديوم، 1 سيليكون، 1 نحاس، 0.22 نتروجين، والمتبقي حديد) عند درجات حرارة مختلفة: 900، 950 و 1000 درجة مئوية. وتم إختيار درجة حرارة 1000 مئوية لعملية التلبيد عن طريق شرارة البلازما. النسبة المئوية القصوى للكثافة حققتها عينة المسحوق المعدني لتكون ذات قيمة 96.73% عند نفس درجة الحرارة أعلاه. مقارنة مع القيم النظرية للعينات المعدة، أظهرت أطياف حيود الأشعة السينية وجود قمم بلورية حادة لأطوار الفيرايت والأوستنايت ولم يلاحظ أي أطوار ثانوية مثل سيغما، تشي، أو نيترايد .

تم فحص الخصائص الكهروكيميائية للسبائك الملبدة في محلول كلوريد الصوديوم (0.2 م)، إختبار الإستقطاب الديناميكي للسبيكة الرابعة (د) المتكونة من (18كروم، 3 منجنيز، 1 ملبيديوم، 1 سيليكون، 0 نحاس، 5 نيكل، 0.22 نتروجين، والمتبقي حديد) أظهر خصائص أفضل للتآكل مثل ارتفاع جهد التنقر، ومقاومة إستقطاب أعلى بسبب ارتفاع محتوى النيكل. كما أظهرت السبيكة الثانية (د) سلوك نشط بسبب التأثير السلبي للنحاس على مكوناتها الداخلية. أظهرت نتائج مطياف الممانعة الإلكتروكيميائي للسبيكة الرابعة (د) مقاومة إستقطاب أفضل مقارنة بالسبائك الأخرى. تم حساب قيم مقاومة الاستقطاب لجميع السبائك من خلال مطابقة الأطياف المأخوذة من مطياف الممانعة الإلكتروكيميائي بإستخدام دائرة مكافئة ومناسبة.

CHAPTER 1

INTRODUCTION

1.1. Fe-Cr alloys

Fe-Cr alloys are among the family groups of stainless steels which are mainly distinguished by their unique characteristics and ability in corrosion resistance. They have emerged to be widely used for different application in vast environmental conditions, thanks to their ability to passivate which give them outstanding properties against corrosion. Their ability to form a chromium-rich passive thin layer which is resistant to corrosion made them be widely used for various industrial applications including pharmaceuticals, aeronautics, chemical, food manufacturer, oil and gas, petrochemical and automotive industries. Fe-Cr alloys include the common stainless steels material such as ferritic and austenitic stainless steels. Stainless steels are considered to have a composition which contains at least 9% Cr and other essential alloying elements.

Stainless steels SSs are classified based on their microstructure. The commonly known groups of stainless steels (SSs) family are;

1. Ferritic SSs
2. Austenitic SSs
3. Duplex SSs

All these groups of SSs are classified based on their difference in metallurgical properties such as chemical properties, microstructures and physical properties which are strongly influenced by their crystal structures. Crystal structure of alloys depends on the chemistry of material and their thermal history. The structure of pure iron does exist at room temperature consist of a ferritic structure of which is a body-centered cubic structure (bcc) known as alpha phase (α). However, based on the iron phase diagram shows, this structure is transformed to the face-centered cubic structure of austenitic structure (fcc), gamma phase (γ), when heated above 910°C. On further heating up to 1400°C the austenitic structure of fcc transforms to ferritic bcc structure called delta phase (δ). [**1,2,3**]

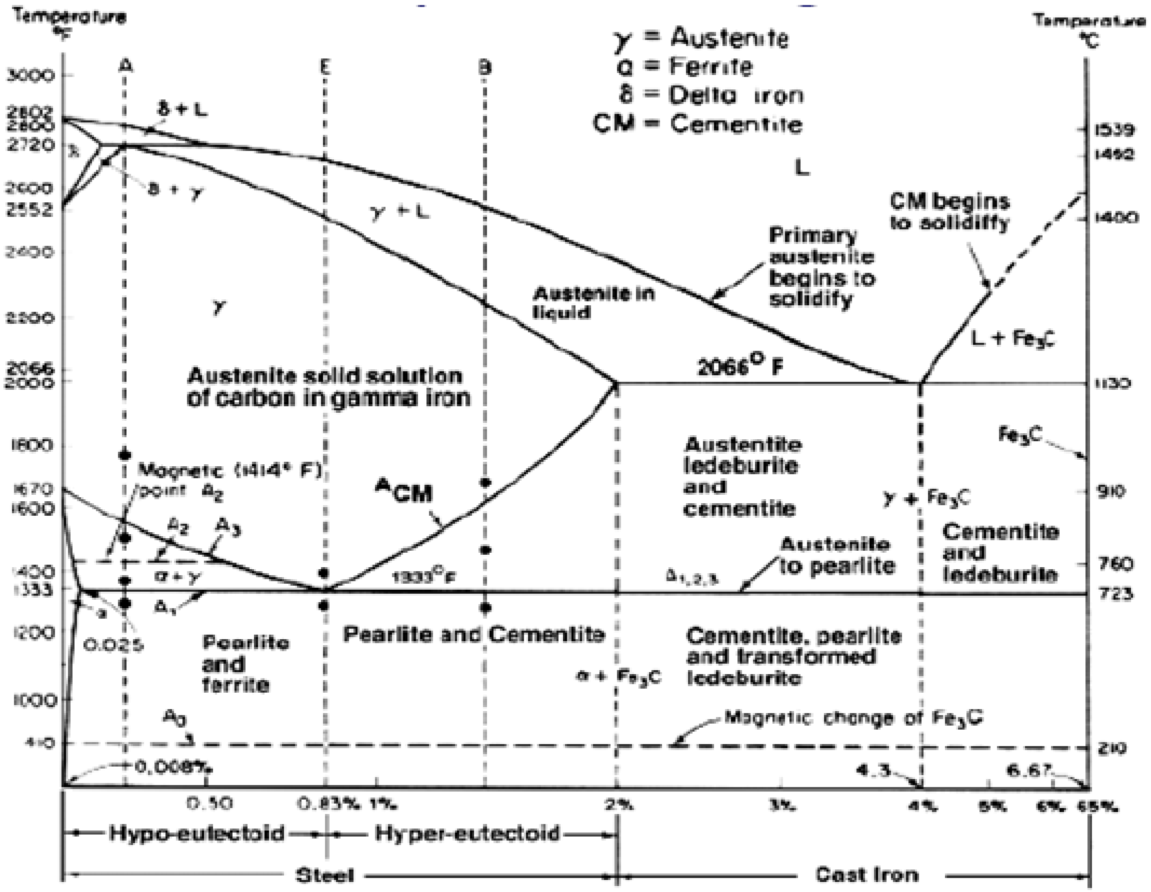

Fig.1. Iron-carbon equilibrium phase diagram [1]

1.2. Duplex stainless steels and their applications

Duplex stainless steels join the families of stainless steel which were discovered in early 1900’s. Developments in Duplex stainless steel were more advanced in during early 1970’s due to the shortage of nickel and it's price volatility which increased the price of austenitic stainless steel. On the other hand, technological advancement in different fields such as oil and petroleum industries which requires higher strength material than austenitic steel with better corrosion properties led to its popularity. However, it was until the discovery of vacuum and argon-oxygen decarburization (VOD and AOD) refining technology which made Duplex stainless steel popular in late 19th century. Due to the introduction of this technique which helped in production of steel with low carbon and with a controlled amount of Nitrogen content which led to manufacture of a material with good chemical combination that improved the good corrosion resistance properties as well as good mechanical such as toughness properties at minimal cost, hence the birth of duplex stainless steel **[4, 5, 6].**

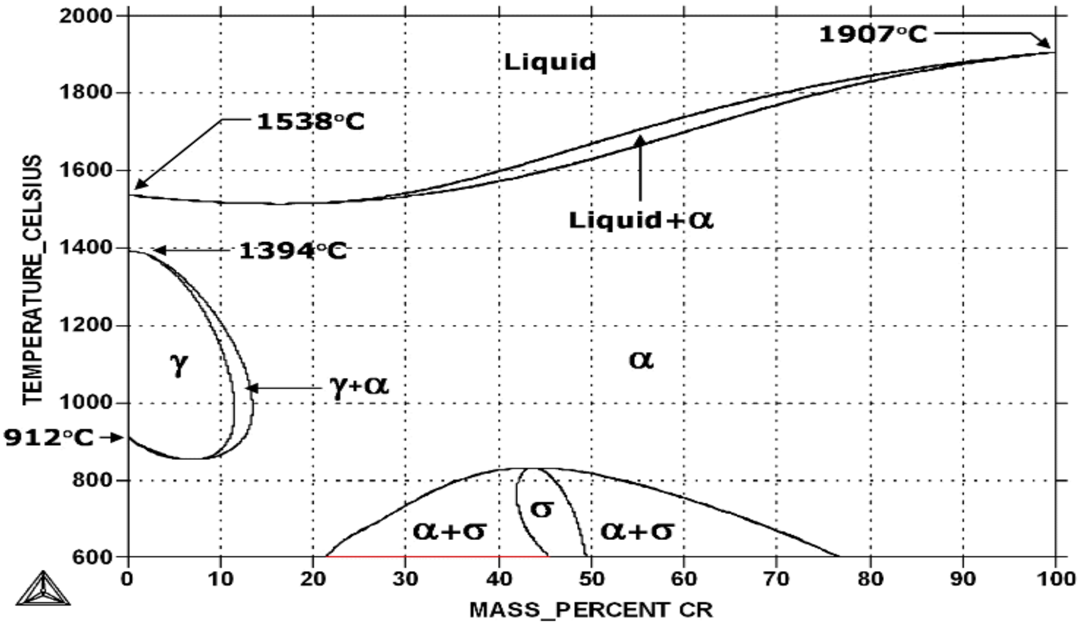

Fig.2 (a). Binary iron-chromium equilibrium phase diagram [1]

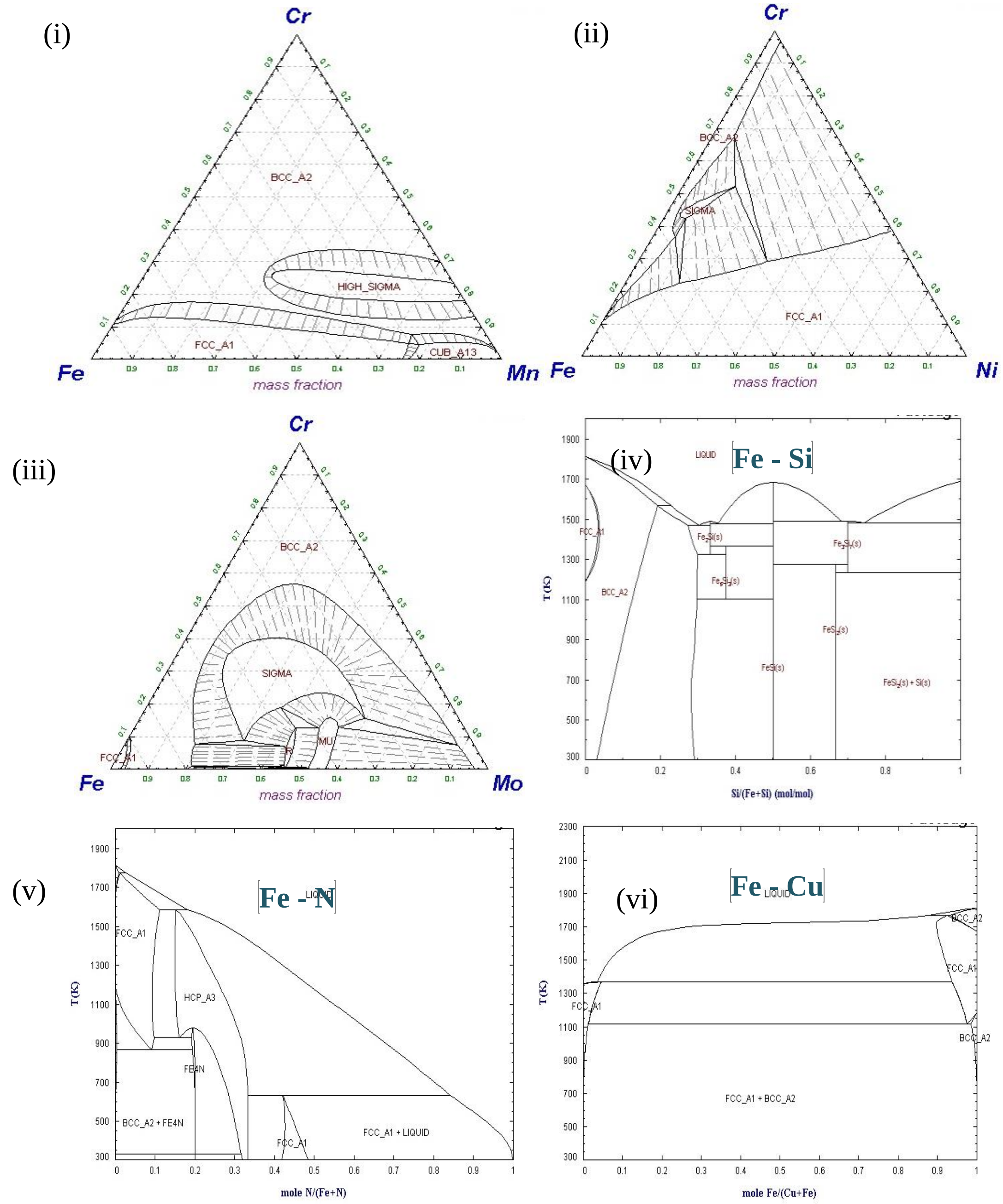

Fig.2(b). Phases present in the phase diagram of (i) Fe-Cr-Mn system at 1100^{o}C (ii) Fe-Cr-Ni system at 900^{o}C (iii) Fe-Cr-Mn system at 1200^{o}C (iv) Fe – Si system(v) Fe-N system and (vi)Fe-Cu system calculated from FactSage software.

Duplex stainless steels are biphasic stainless-steel materials which consist of nearly equivalent ferritic and austenitic phase structure which plays a vital role to their outstanding corrosion resistance and mechanical properties in comparison to their counterpart ferritic and austenitic stainless steel. It comprises the features of the major categories of stainless steel that made it a choice for numerous applications. It is characterized by high toughness, high strength, high corrosion resistance properties, low thermal expansion and good weldability which increase its demand in wide applications areas in which there is elevated temperature and corrosive environments such as oil and petrochemical, chemical, marine, nuclear power and automotive industries **[7, 8].**

The term economical duplex stainless steel refers to the cost reduction during manufacturing of duplex stainless steel in comparison to other series. Most of these series have reduced the amount of expensive alloying element in duplex stainless-steel composition and replacing it with the elements with similar functions or offer the same characteristics in duplex stainless steel. Nickel is the most expensive alloying element used in the manufacturing of duplex stainless steel. The volatility of Ni price has led to more efforts on developing new duplex stainless steel with less or Ni-free in their elemental compositions. The main reason for Ni replacement is for the cost reduction whereby the common Ni alloying element which is expensive is reduced in amount or completely being replaced by Mn and N which are also austenite phase former **[8, 9].** Mn is not a good austenite stabilizer as Ni though is 8 times cheaper to Ni. The combination of Mn and N can be a good replacement since N is also a good austenite former and can improve pitting corrosion resistance as well as the strength of the material. Mn introduction also helps to increase the solubility of N in stainless steel however if not controlled can lead to the formation of secondary phases thus decreases the corrosion resistance properties **[9, 10].** However, this evolution has mainly targeting to achieve duplex stainless steel with better or similar corrosion resistance properties to that of standard austenitic stainless steel AISI 304

1.3. Development of Duplex stainless steel

1.3.1. Cast Duplex stainless steel

Economical duplex stainless steel consolidated by casting technique has been reported by researchers with different composition in which the common Ni have been lowered or replace by Mn and N as well as the addition of other alloying elements. Li et al. **[11]** developed an economical duplex stainless steel alloy with less Ni and an addition of Cu and W. Microstructure, mechanical and corrosion properties were studied in comparison with 304 stainless steel. It was observed that the alloys had better corrosion properties than 304 when tested in ferric chloride solution. The DSS alloy with composition 19Cr-6Mn-1.3Ni-1.0Mo-0.5W-0.5Cu-0.2N was found to be optimum alloy with better corrosion resistance properties. No sigma phase precipitation was found after solution treatment of the alloys from 750^{o}C to 1250^{o}C. Jiang et al. **[12],** also developed an economical DSS and replacing Ni with Mn-N and the optimum alloy with Ni of 2% (22Cr-8.0Mn-2.0Ni-1.0Mo-0.7Cu-0.7W-0.3N) was found to have better corrosion properties than AISI 304SS. No sigma phase or Cr-nitride phase was observed after solution treatment at 750^{o}C to 1300^{o}C for 30min. Toor Ihsan-ul- Haq et al. **[13],** developed a high Mn and free Ni DSS with the composition of 18Cr-6Mn-1Mo-0.2N examining the effect of manganese on corrosion and mechanical properties of DSS. Zhang et al. **[14]** developed a Mo free DSS alloy with a variation of W and its effect on corrosion resistance properties and mechanical properties were investigated. The corrosion properties of the alloys increased as the content of W were increased. Chen et al. developed an economical DSS with sigma free and investigated the microstructure, mechanical and corrosion properties in comparison to standard AISI 304SS.The alloy consists of 19Cr-6Mn-1.0Mo-0.5Ni-0.5W-0.5Cu-0.2N composition was found with no sigma phase, however, Cr-nitride compound was observed after aging for 8 hours at 750^{o}C **[15].** Qingxuan Ran et al. **[16]** developed Cu-bearing economical DSS to examine the effect of Cu on the microstructure and properties of these alloys. 21Cr–2 Ni–1.0Mo–0.2N–1.0Cu alloy was found to be optimum with better mechanical and corrosion properties than AISI 316L austenitic SS. However, some precipitates such as sigma, Cr-nitride, and ϵ-Cu were observed when solution treated at 780^{o}C for 30min.

1.3.2. Powder Metallurgy Duplex stainless steel

Recently, many researchers have tried to develop and investigate on the properties PM duplex stainless steels (DSS) group through different combination of alloy elements and processing route to acquire better mechanical and corrosion properties. Garcia et al. **[17]** investigated on the corrosion behavior of DSS alloys sintered in nitrogen. He used pre-alloyed ferritic (AISI 430L) and austenitic (AISI 316L) SSs powder as a raw material and sintering atmosphere as N_2-H_2 (95% and 5%). Observation shows that the increase in austenite/ferritic phase ratio had a positive impact on the corrosion properties where corrosion potential shifted to more noble and decrease in passive current density. Dobrzanski et al. **[18]** studies the corrosion properties of vacuum sintered DSS alloys by mixing austenitic (AISI 316L) and martensitic (AISI410) pre-alloyed powder and controlling amount of alloying elements such as Cr, Ni, Mo, and Cu to obtain a biphasic structure of DSS alloy. He consolidated the powder sample at 800MPa and sintering temperature of 1260^{o}C. The results showed an alloy with better pitting corrosion resistance had a balance of austenite/ferrite phase. However, the microstructure of DSS alloy influenced the corrosion propertied due pore morphology and density properties. Shashanka and Chaira **[19]** developed a nanostructured DSS alloy of composition consist of Fe-18Cr-13Ni by planetary milling for 40h and sintering at 1400^{o}C for 1h. He observed that, at 300rpm, ball to powder ratio of 6:1, 1400^{o}C sintering temperature the density of 90% and Vickers microhardness of 550HV was achieved. They also **[20]** studied the phase transformation of ferritic and austenitic powders prepared from elemental milling of Fe, Cr and Ni at different atmosphere of nitrogen and argon. They concluded that nitrogen atmosphere stabilizes austenite phase formation. They further investigated the optimum parameters for synthesizing nanostructured duplex and ferritic stainless steel by high energy planetary milling **[21].** They found that process control agent (PCA), ball to powder weight ratio (BPA) and milling speed, all have an influence on the particle size and morphology as well as phase transformation during the milling process. Amini et al. **[22]** also, studied the microstructure phase evaluation of high nitrogen Fe-18Cr-8Mn alloy powder prepared by mechanical milling. It was found that the quantity of nitrogen increases as the milling time increase together with grain refinement and phase transformation from α-phase to γ-phase and an amorphous phase. However, the study revealed that under argon atmosphere the predominant phases were the α-phase and amorphous phase. It was also concluded that the grain refinement and phase transformation occurs more under nitrogen than in argon atmosphere during mechanical alloying (MA). Tehran et al. **[23]** conducted a study on the effect of particle size on the transformation of α to γ during mechanical alloying of Fe-18Cr-10Mn-4Mo alloys under nitrogen atmosphere. The alloy was successfully produced through mechanical alloying without any heat treatment to elemental powder of an alloy. It was observed that there are more phase transformation and decrease in particle size as the rate of nitrogen absorption increases. Initial powder particle size shows an influence on phase transformation during mechanical alloying. The solubility increases as milling time increases due to increase in the lattice defect and development of nanostructure during milling of an alloy. A similar investigation was conducted by Haghir et al. **[24]** on the austenitic stainless steel Fe-18Cr-11Mn where it was found that the nitrogen solubility increases with milling time and formation of austenite phase is favorable in a nitrogen atmosphere while ferrite phase in argon atmosphere during mechanical alloying. Brytan et al. **[25]** prepared duplex stainless steel from ferritic powder and mixing of alloying element powders. He observed the effect of sintering time at 1250^{o}C and concluded that sintering time has influenced the increasing density, mechanical properties, and microstructure balance. Enayat and Bafandeh **[26]** investigated on the phase transition of Fe-Cr-Ni alloys during mechanical alloying following by annealing of the powder. It was observed that single phase nano-structured bcc α-phase was obtained after annealing at 700^{o}C which differ from the predicted result from the phase diagram.

CHAPTER 2

LITERATURE REVIEW

2.1. Role of alloying elements and their characteristics

Alloying elements in DSS design play a pivotal role in describing their mechanical as well as corrosion resistance properties of these alloys. Alloy elements help in the formation of ferrite and austenite phase as the main microstructure of DSS alloys. The content and characteristics of alloying elements also may result in secondary phases as the previous discussion reported. However, secondary phases can be minimized or eliminated by the appropriate control of alloying elements and selection of proper fabrication methodology. DSS alloy elements comprise of Cr, Mn, Mo, N, Ni, Si, Cu and others [**27**]. Each element plays a significant role in the metallurgy of DSS alloys.

2.1.1. Chromium

Chromium is a strong ferrite former which implies that the addition of Cr stabilizes the bcc structure of iron. It is also a good alloying element for improving localized corrosion resistance in DSS alloys. Cr forms a passive film of oxy-hydroxide nature which protects the metal from localized corrosion under atmospheric condition. The increase of Cr content increases the corrosion resistance of duplex stainless steel [**27, 28**, **30**]. However, a higher amount of Cr causes the formation of detrimental phases which affect corrosion resistance properties of DSS alloys [**27**]. Cr equivalent formula in DSS alloys is given as [**27, 31],**

$$\text{Cr eq} = \%\text{Cr} + \%\text{Mo} + 0.7 \cdot \%\text{Nb}$$

2.1.2. Nickel

Nickel is an austenite stabilizing element which changes the bcc structure to fcc structure of stainless steel when added to ferritic stainless steel [**28**]. Nickel control phase partitioning in DSS alloys to balance the ferrite and austenite phase. The proper amount of Ni should be balanced to have an approximately equivalent phase in DSS structure. Ni equivalent formula is given as [**27**, **31, 32**].

$$\text{Ni eq} = \%\text{Ni} + 35\cdot\%\text{C} + 20\cdot\%\text{N} + 0.25\cdot\%\text{Cu}$$

Nickel helps to increase toughness and increase the corrosion resistance of DSS alloys by pushing the electrode potential in the noble region and reduces values of current density as well as it improves pitting corrosion resistance **[30, 32].**

2.1.3. Nitrogen

Nitrogen is an austenite former element which also helps to improve pitting corrosion resistance and strength of DSS alloys [**27, 30, 32, 34].** The increase in nitrogen content improve the pitting corrosion resistance and have a positive impact on DSS structure stability at elevated temperature [**29**]. Nitrogen helps to improve the crevice corrosion resistance especially in acidic solution, however, in neutral and basic condition has no such effect [**34**]. Nitrogen delays the formation of intermetallic compounds in DSS [**28**]. The solubility of nitrogen is limited as an austenite former hence Mn or Mo are added to increase its solubility. However, the higher amount of these elements may lead to the formation of secondary phases [**32].**

2.1.4. Manganese

Manganese is an austenite former and increases wear and abrasion resistance, tensile strength without any loss of ductility. The austenite phases increase with an increase in Mn and decrease with an increase in solution temperature. Due to the higher price of Ni, Mn as an austenite former and Nitrogen are used to replace Ni for cost reduction of DSS alloys [**35**]. Mn increases the solubility of nitrogen in the stainless steel and it increases pitting corrosion resistance, however, it may cause secondary phases such as MnS if its amount is not controlled. MnS are usually acting as an initiation site for pit formation which may result in the reduction of pitting resistance [**27, 28**, **35**].

2.1.5 Molybdenum

Molybdenum is a ferrite stabilizer element and protects the DSS alloys from pitting and crevice corrosion by forming a protective film of molybdate ion or an oxy-hydroxide layer [**27**]. Mo protects the DSS alloys 3.3 more than Cr as represented in the pitting resistance equivalent number (PREN) equation [**27**]. However, a higher amount of Mo may cause detrimental secondary phases such as sigma and chi phases which affects the properties of DSS alloys [**33**]. Therefore, Mo content is restricted to less than 4% in order to avoid the formation of secondary phases [**29**].

2.1.6. Copper

Copper is an austenite former element and can be added to enhance corrosion resistance properties of stainless steel in acid environments. The addition of Cu helps to suppress the anodic dissolution by enrichment of noble Cu on the surface film [**35**]. The higher amount of Cu may cause the formation of secondary phases; therefore, its amount is restricted to 2%wt [**27**].

2.1.7. Silicon

Si element is a ferrite former and known to improve pitting resistance in stainless steel. When Si increases, it increases the Cr_{eq} / Ni_{eq} ratio. Thus, it increases the delta ferrite when added as the ferrite former in DSS alloys which can be achieved as by the increase in Cr_{eq} / Ni_{eq} ratio [**36**].

2.2. Secondary phases in DSS alloys

2.2.1. Metallurgical process of DSS

Duplex stainless steel comprises of different alloying elements that enhance its outstanding properties mechanically as well as corrosion resistance. On the metallurgical point of view, solidification process of DSS alloys can simply be represented by a ternary phase diagram at the section of 70% iron **[36]** as shown in the Fig.1**.**

The metallurgical behavior of Duplex stainless steel is well represented by Fig.1 above of which shows ternary phase diagram. At elevated temperature, DSS alloys solidify as ferrite and then transforms to austenite as temperature decreases depending on the alloy composition. The approximately balanced phase of ferrite and austenite phase is achieved when water quenching process is applied from solution annealing temperature. In addition, the ferrite and austenite phase can be predicted by Cr and Ni equivalent calculation together with Schaeffler's diagram can also be useful [**36, 37].**

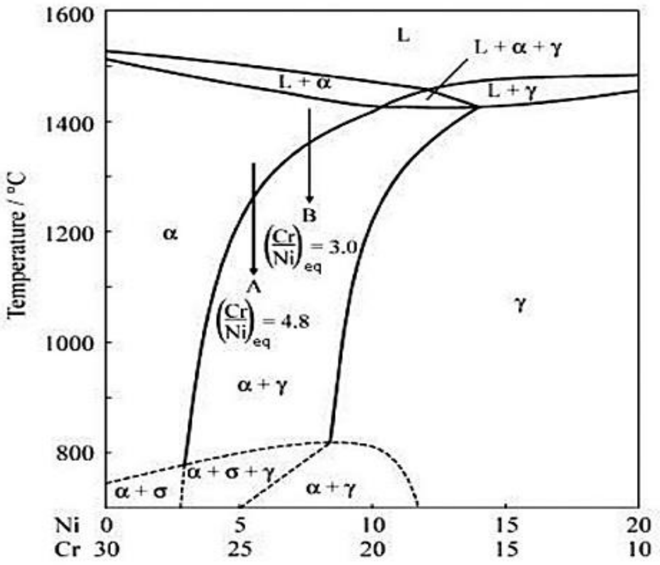

Fig.3. Phase diagram showing the section of 70% iron at Fe-Cr-Ni system **[36].**

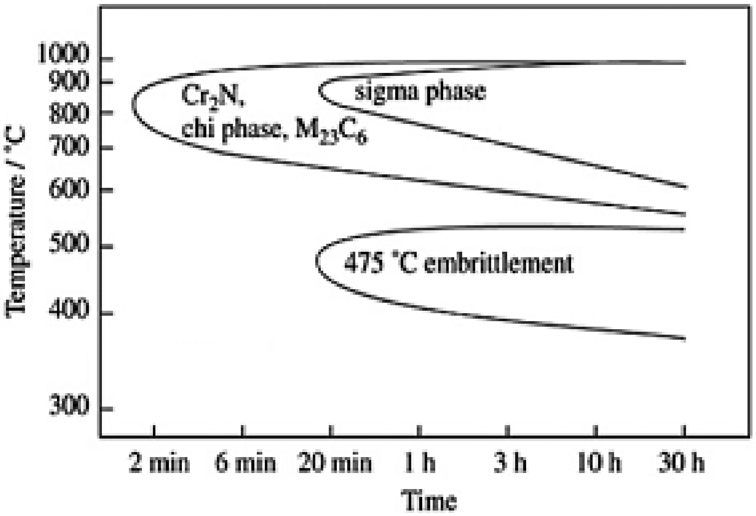

Fig.4. Formation of different secondary phases at elevated temperature **[38].**

During solid-state transformation at elevated temperature, DSS alloys have a tendency of forming secondary or intermetallic phases that are detrimental to their outstanding mechanical and corrosion resistance properties. These phases include sigma (σ), chi (χ), R, Pie (Π), carbides, α prime and others **[33, 36].** Paulraj et al. **[38]** reported that formation of secondary phases such as sigma (σ) phase, chi (χ) phase, chromium nitride and carbide phases occur at a temperature range of 500°C to 1000°C as shown in Fig.2. It was reported by N.Llorca Isern et al. [**27]** that, the exposure of duplex stainless steels at an elevated temperature in the range of 600°C to 1000°C lead to precipitation of secondary phases such as sigma (σ) phase, chi (χ) phase, chromium nitride and carbide phases.

2.2.2. Sigma phase

Sigma phase is formed during aging of DSS alloys between temperature ranges of 750°C-900°C **[33].** Sigma phase is a nonmagnetic intermetallic phase with a crystallographic tetragonal structure which consists of 32 atoms per unit cell. It has a side effect on the mechanical properties of DSS alloys such as increase of hardness and decrease of toughness and elongation [**38].** It is a Cr-Mo rich phase in which its formation is enhanced by Cr, Mo, Si, Mn, and Ni. **[27, 33].** Due to a higher rate of elemental diffusion from ferrite than austenite phase, Cr and Mo diffuse from ferrite to sigma phase. Mo act as controlling element in the formation of this intermetallic phase which diffuses from ferrite phase to sigma phase **[33].** The diffusion of chromium is the primary thermodynamic process during formation of sigma phase. This phase results when ferrite phase is transformed to sigma and secondary austenite at eutectoid reaction **[27, 39].** Sigma phase is usually nucleating at ferrite/ferrite boundary or ferrite/austenite boundary due to high energy at these nucleation sites **[27, 38].**

Sigma phase formation can well be explained by time-temperature-transformation (TTT) diagram obtained by isothermal heat treatment followed by quenching process and continuous cooling transformation diagram (CCT) as shown in Fig.3. In TTT diagram the time for other phase decomposition to another phase at isothermal temperature is described. CCT shows a time for a phase decomposition to another phase at a different cooling rate **[33].**

Sigma phase formation rate is different for tempering and quenching process, for tempering the rate of formation is higher than quenching process. The cooling rate for sigma phase formation in quenching process is less than 1K/s. Sigma phase precipitation can be minimized by high cooling rate or adjustment in chemical composition **[27]**. Sigma phase has detrimental effects on the properties of stainless steel alloys such as the formation of the brittle region and depletion of Cr which results in the reduction of corrosion properties such as resistance to intergranular corrosion in Cr depleted areas **[40].**

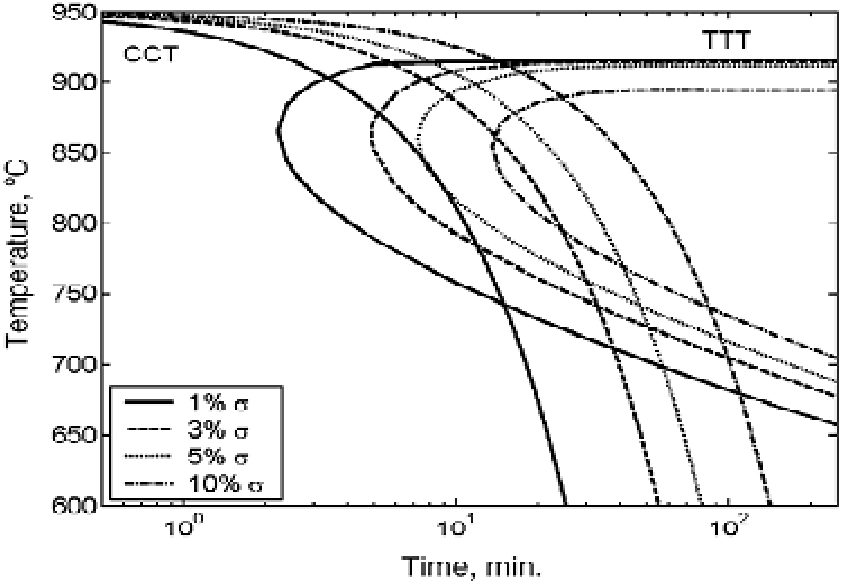

Fig.5. TTT and CCT curve showing sigma phase formation during quenching **[33]**

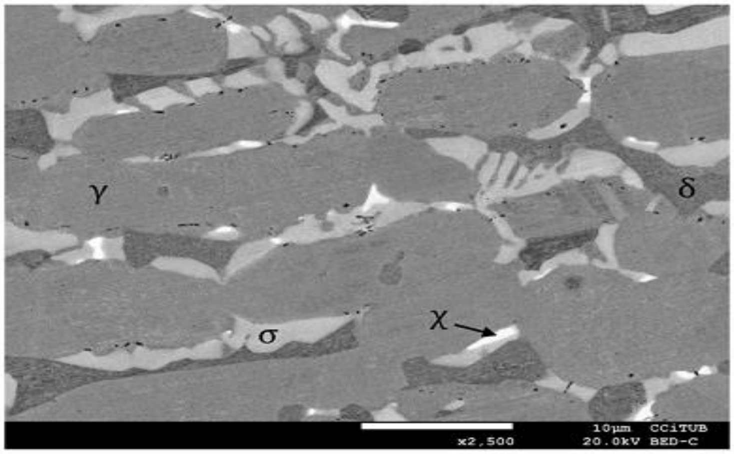

Fig.6. Sigma phase (σ- light gray) and chi phases (χ-brighter) in DSS 2205 with ferrite phase (darkest), austenite (dark gray) phase which can be clearly seen after aged for1 h at 830°. [**38**]

2.2.3. Chi phase

Chi phase is a phase which forms prior to sigma phase formation at a temperature range of 750°C – 850°C. This phase is thermodynamically unstable and belongs to topological closed packed phase formed from Fe, Mo and Cr elements **[27, 38].** It contains more of Mo element than sigma phase and it forms due to the eutectoid reaction of ferrite phase into sigma, chi and nitride compound. Chi phase transforms into ferrite phase after prolonged heating despite the early formation prior to sigma phase **[27, 33].**

2.2.4. R phase

R phase consists of the higher amount of Mo which enhance their stability. The formation of R phase occurs at the temperature range of 550°C to 650°C during the early stages of tempering. It later transforms into sigma phase as tempering time increases [**27, 41**]. R phase precipitates at the interface of ferrite and austenite phase as well as inside ferrite phase as shown in the Fig.5. Hwang et al. reported that R phase has a significant impact on the toughness of DSS alloys at the early stage of its formation [**41**].

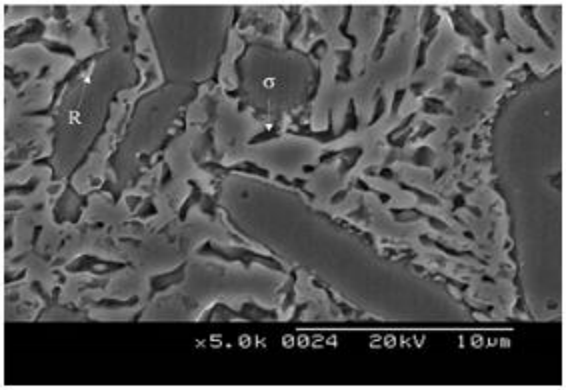

Fig.7. Precipitation of R phase at ferrite/austenite phase and inside ferrite phase [**41**].

2.2.5. Pie phase

Pie (Π) phase is in rich of Mo and Cr which is the same composition with sigma phase. However, it can be clearly differentiated from sigma since it is formed after a long time of isothermal aging at 600°C [**27**].

2.2.6. Nitride phase

Nitride compounds such as Cr_2N trigonal structured compounds are formed at the temperature range of 700-900°C when fast cooling from high annealing temperature. Cr_2N forms at the intergranular site due to saturation of ferrite with nitrogen at elevated temperature [**42, 43**]. CrN phase is commonly found during welding operations at heat affected zone [**27**]. It was reported by Maetz et al. [**43**] that the precipitation of Cr_2N is usually found at delta/delta interface or in the delta ferrite grains and it forms due to the eutectoid reaction of delta ferrite to Cr_2N and secondary austenite phase during aging.

2.2.7. Alpha prime phase

Alpha prime phase consists of Fe and Cr elements and forms at the temperature range of 280-500°C. This phase cause embrittlement at this temperature range due to decomposition of ferrite phase into an alpha phase which is rich in Cr content. The embrittlement is due to miscibility gap and leads to this decomposition at a temperature of 280-500°C in iron chromium binary system [**44**].

2.3. Mechanical alloying (MA) and Ball milling process

Mechanical alloying MA is defined as the solid-state processing technique of powder metals where it involves several repeatedly stages such as welding, fracturing, and re-welding during ball milling. It has emerged to be a widespread technique used to synthesize equilibrium and non-equilibrium alloys through the blending of elemental or pre-alloyed powders to achieve better and improved material than the ones produced through conventional route. MA was discovered in 1966 in aerospace industries due to the demand for oxide dispersion strengthened (ODS) iron and nickel-based super-alloy material used as gas turbine applications. This technique is simple, viable and economical for production of different alloys material, also possesses a technical advantage as well. The common know advantages of MA over other technique such as rapid solidification processing (RSP) is that immiscible material or element can be combined during milling. **[45]**

MA processing includes loading the powder in the stainless-steel container with milling balls, i.e. hardened stainless steel or tungsten carbide balls, which is later sealed during milling. There are several factors and parameters (process variables) which are to be considered during MA. Stainless steel containers are sealed in a certain atmosphere such as argon, nitrogen-hydrogen or toluene in order to prevent any oxidation that might take place during MA. Milling is conducted under the desired duration of time and process control agent PCA usual steric acid is added to the container to prevent any contamination and cold welding among the powder particles especial when powders of ductile metals are milled. The commonly known process variables during MA are the type of mill, milling container, milling speed, milling time, type, size, and size distribution of the grinding medium, ball-to-powder weight ratio BPR, the extent of filling the vial, milling atmosphere, process control agent PCA, and temperature of milling. [**46**]

Mills used during MA are selected based on the quantity demand for instance when the powder is of 10g in weight SPEX mills are used and time for processing is shorter, however, for few pounds processing at a time Attritors or Fritsch Pulverisette are used and duration for processing is longer than the later. **[45, 46]**

MA achieves maximum equilibrium and extension of supersaturation of solid solubility at room temperature. However, based on Hume-Rothery rules, which shows that the increase in solubility depends upon relative atomic sizes, crystal structures, and electronegativity of the solvent and solute. During MA of the powder mixture, amorphous phase occurs after a certain duration and condition during of milling as well as during contamination. However, the mechanisms for amorphization is not yet clearly suggested and understood. The common route for the occurrence of the amorphous phase is suggested to be as ordered phase → disordered phase (loss of long-range order) → fine-grained (nanocrystalline) phase → amorphous phase. However, in other condition, the chain might be different or contain intermetallic phase **[45, 46]**.

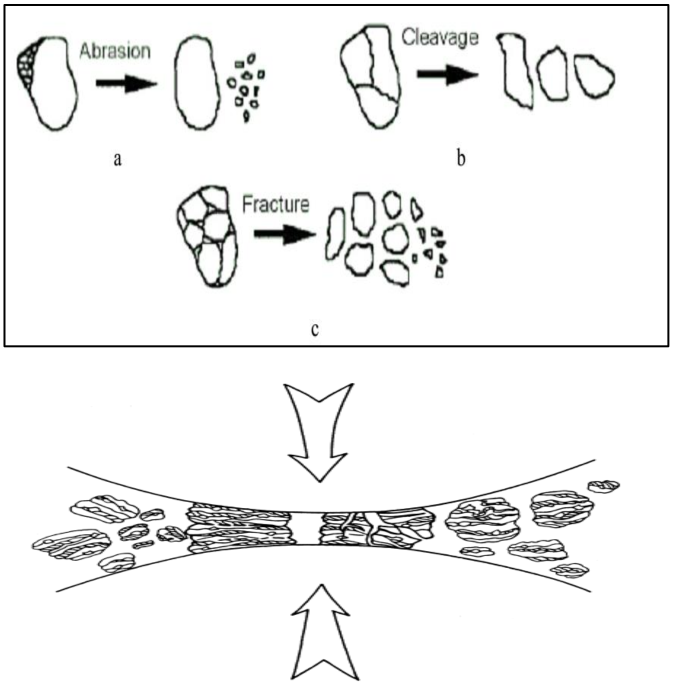

Fig.8. Working principle of powder size reduction in a ball mill. [**47**]

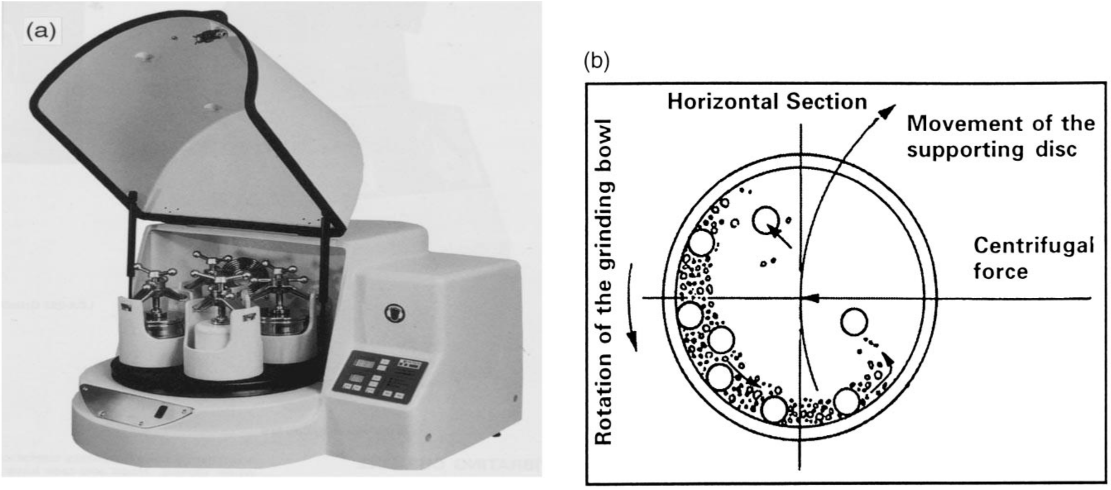

Fig.9. (a) Fritsch Pulverisette P-5 type of ball milling. (b) Schematic presentation of the motion of balls and powder during milling.

2.4. Spark Plasma Sintering (SPS)

Spark plasma sintering SPS is the latest technology in sintering or compaction of ultra-fine grain sample which emerges to be more convenient and time efficient than the conventional sintering technique such as furnace sintering. SPS provides less time for sintering as well as to help in controlling microstructure and grain growth of a material during sintering of their respective powders [**4**]. It was commonly used for ceramic material however, it has emerged to be used in sintering of metals such as stainless steel, aluminum alloys and nickel alloys [**48-50**]. Spark plasma sintering equipment consists of compaction section through which load is applied to the powder material to be sintered in a graphite die by upper and lower punches. SPS system includes sintering, joining, growth and reaction through generated sparks. It is one of the modern technology which is rarely used in the sintering of stainless steels alloys. SPS works by generating a pulse from DC current which helps consolidation of powder through uniaxial pressure [**4,49,50**]. There are several microstructure properties advantages on material by employing SPS techniques over conventional sintering techniques such as effortless operation, rapid sintering, high densely packed powder, rapid cooling, high heat efficiency and uniformity during sintering as well as cost-efficient. However, the common parameter implemented to attain and retain the nano-crystalline structure of material are processing temperature and holding time during sintering [**4**].

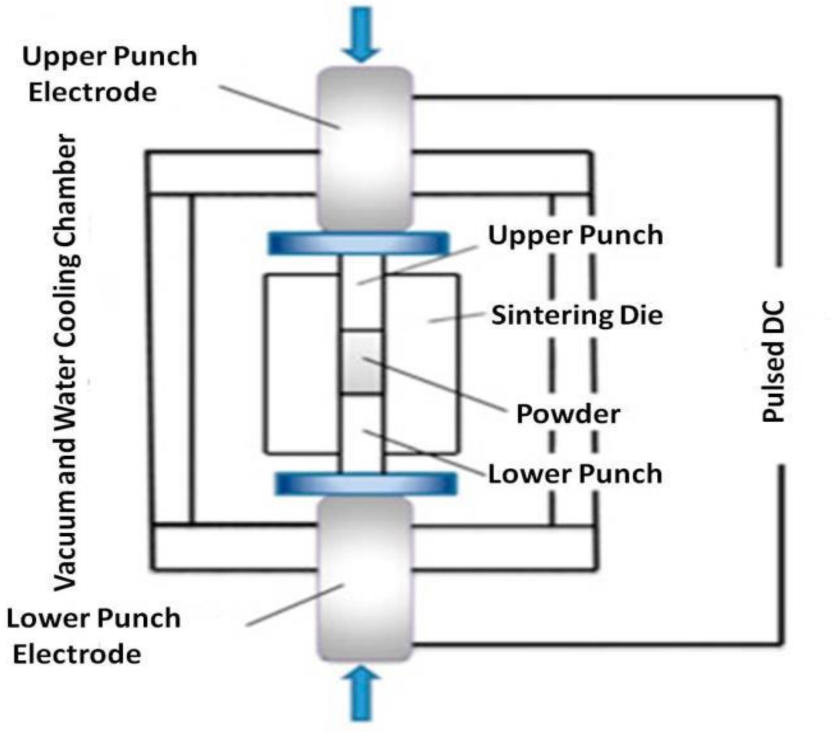

Fig.10. Schematic of Spark plasma sintering process [**50]**

Table 1. Shows different spark plasma sintering parameter from different literatures.

REFERENCE	**Sintering temperature (º C)**	**Holding time (min)**	**Heating rate (ºC/min)**	**Applied pressure (MPa)**
Optimization of process parameters for spark plasma sintering of nano-structured ferritic Fe-18Cr-2Si alloy. (*I.-H. Toor et al. / Powder Technology 299 (2016)) [4]*	900, 1000, 1100	5, 10, 15	50, 100	50, 60
Processing of Nanostructured High Nitrogen Stainless Steel by mechanical alloying... *Cisnores et. al 2005 Metallurgical and Materials Transactions; [60]*	600 - 13 min 700-15min 800 -7 min 1000- 7 min			
Effect of Sintering Holding Time on the Corrosion Properties of Nano-Structured Fe-18Cr-2Si Alloy Prepared by SPS... *Ihsan-ul-Haq Toor Int. J. Electrochem. Sci., 11 (2016) [61]*	1100C	5, 10, 15		50
Harmonic Structure Design of a SUS329J1 Two-Phase Stainless Steel and Its Mechanical Properties. *Ciuca et.al. (2013). Materials Transactions, Vol. 54, No. 9 (2013) [62]*	850 C	10		50
Preparation of high-performance bulk Fe-N alloy by spark plasma sintering...*Cui et.al (2016). Materials and Design, [63]*	600, 650, 700, 750	5	140	50
Fabrication of Nano-Yttria Dispersed Duplex and Ferritic Stainless Steels by Planetary Milling Followed by Spark Plasma Sintering and Non-Lubricated Sliding Wear Behaviour Study... *Shashanka et.al (2016) Journal of Materials Science and Engineering B 6 (5-6) (2016) [88]*	1000	5		50
Evolution of structure in austenitic steel powders during ball milling and subsequent sintering ...*Oleszak et.al. 2007 Journal of Alloys and Compounds [89]*	1050	5		40

Mechanism of SPS comprised of discharge of DC current pulse which acts as cleaning and surface activation of powder. Consequently, the electric discharge forms between powder particles resulting in a local high-temperature state which causes vaporization and melting of the powder surface. Thereafter, neck forms around the particles and gradually developing while plastic transformation progresses during sintering. The density of the material achieved ranges between 95-99%. During sintering, particle growth is under control due to the fact that the surface temperature of the particle rises rapidly by self-heating phenomenon [**51**].

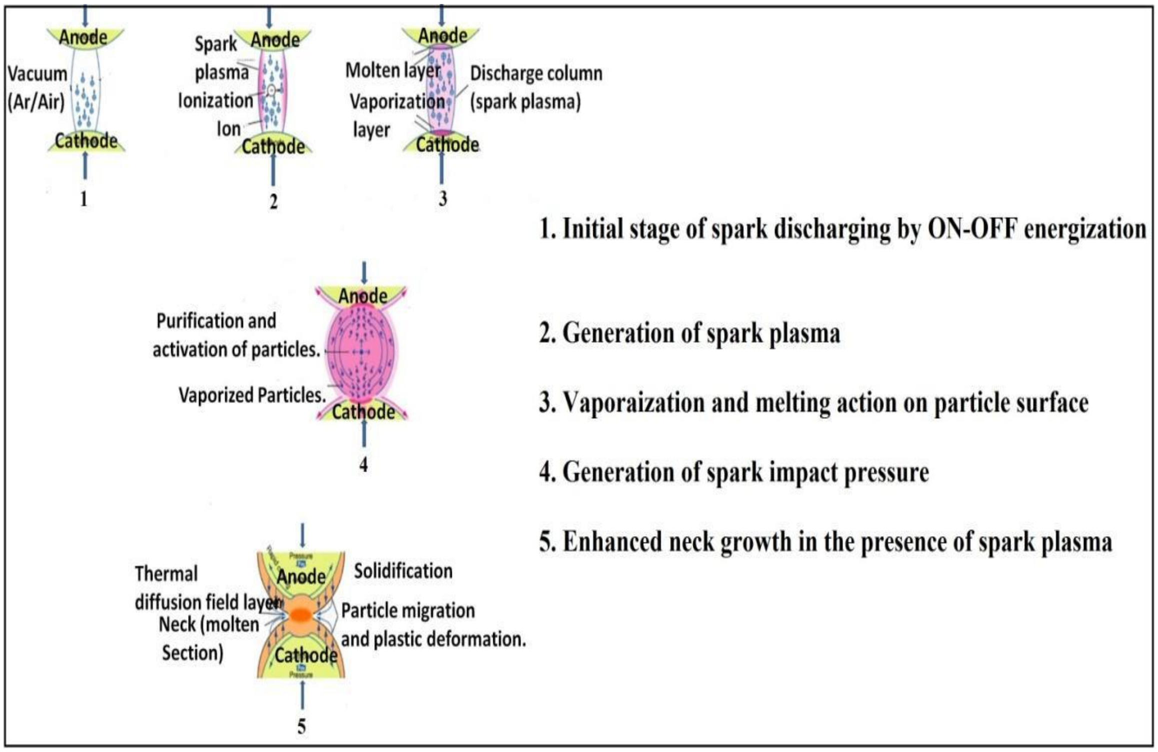

Fig.11. Mechanism of Spark plasma sintering process [73].

2.5. Critical review of the corrosion performance of existing CAST and Powder Metallurgy Duplex Stainless Steel Alloys

Corrosion resistance behavior is most highly prioritized property in the manufacturing of PM stainless steels SSs. However, many PM industries and researchers have worked on the requirement for optimization of corrosion resistant behavior of SSs [**1**]. PM SSs has been reported to have no uniform corrosion resistance properties in comparison to wrought

SSs due to the nature of microstructure which consists of many pores [**1, 17**]. However, other researchers have presented that PM SSs with porosity have exhibits better corrosion properties than wrought SSs **[1].** Microstructure properties such as porosity and density have a vital influence on the corrosion properties of PM stainless steels SSs. The fact that lower dense PM material with porosity may result into penetration of electrolyte through the interconnected pore and lead corrosion proceedings, also the opening pores increases the surface which is exposed to corrosive environments **[17, 18].** It has been also reported that some forms of corrosion such as crevice corrosion are initiated through pore presence where stagnant electrolyte can be found, hence concentration cells occur, and passivity nature of material decline gradually [**7, 17, 18**]. SSs can also undergo chromium depletion from their microstructure due to the formation of intermetallic phases or when exposed to a certain temperature. This phenomenon of chromium depletion especially at grain boundaries is regarded as sensitization [**51**]. Chromium depletion and presence of porosity in microstructure form synergetic corrosion resistance deterioration of SSs.

DSSs have found wide applications in many industrial sectors due to the ability to resist corrosion in different environments and operating conditions as well as offering good mechanical properties to sustain high loads **[17,18,53**]. Many researchers have investigated on the corrosion properties of these alloys in comparison to other alloys corrosion with good corrosion properties such as AISI 304 and 316L austenitic SSs. Corrosion resistance properties of DSS alloys is strongly influenced by microstructure and phase balance of which is the mixture of ferrite and austenite phase [**17,53**]. The ferrite-austenite phase ratio plays a big role in the determination of good corrosion resistance of DSS alloys. It was reported that **[7]** a DSS alloy made from premises of 316L and 434L SSs powder of ferrite-austenite phase ratio of 40%-60% has shown good corrosion resistance when tested in 1M H_2SO_4 solution. It has also been reported that sintering cooling rate of DSS affects the corrosion resistance by forming intermetallic precipitate [**54**]. Sintering cooling rate is related to phase balancing in DSS by forming appropriate ferrite/austenite phase ratio which exhibits maximum corrosion resistance properties [**38, 40, 54]**. Corrosion properties of DSS alloys have been also reported to improve when DSS alloys are sintered in a nitrogen atmosphere. Nitrogen element is an austenite phase stabilizer which provides good duplex structure stability and improves pitting corrosion resistance properties in DSS alloy.

However, nitrogen cases of forming Cr-nitride precipitation have been detrimental to corrosion resistance properties in DSS alloys [**17, 22, 29**]. In DSS manufactured by addition of alloying elements, good corrosion resistance was achieved due to a fine intermixed microstructure which consists of ferrite and austenite mix phase [**17, 55].** Alloying elements such as Cr, Mo, and N which have been used in the consolidation of DSS have a strong impact on pitting corrosion resistance. These alloying elements provide special characteristic known as pitting corrosion resistance equivalent number known as PREN. DSS alloys are usually classified based on the composition and PREN values [**28, 57**]. The commonly used PREN formula for calculation have been reported by Morello et al. [**29, 57**] are as written here below:

$$\mathrm{PREN}_{16} = \%\mathrm{Cr} + 3.3\%\mathrm{Mo} + 16\%\mathrm{N}$$

$$\mathrm{PREN}_{30} = \%\mathrm{Cr} + 3.3\%\mathrm{Mo} + 30\%\mathrm{N}$$

It has been reported that pitting resistance (PREN) basically depend on the alloying element Cr, Mo and N. PREN_{16} has an exponential correlation with DSS alloy with low Ni and high Mn-N content. However, PREN_{30} is also considered when the effect of nitrogen in pitting is to be analyzed **[29].**

2.6. Biomedical applications of Stainless steel

Stainless steel materials have been used for biomedical applications to replace and functions as the body parts in human anatomy. The applications of SSs materials in the human body structure includes implants in the dental structures, shoulder, knee, elbow, artificial valves in the ventricles of the heart, hip bone as well as stents in the blood vessels **[73,74].** The use of stainless steel in biomedical applications is attributed to their unique characteristics of passivation due to Cr content, load bearing capacity due to their appropriate density and biocompatibility, good toughness and workability [**74,75**]. Other requirements for biomedical material includes the absence of ferromagnetic properties of the material which implies that the only material compatible with this application is austenitic structured stainless steel [**74-77**]. However, due to the harmful effect of nickel ions release of austenitic stainless steel, there is an urgency to produce a new material with no nickel content to avoid any risk associated with nickel ions. Many cases have reported on the harmful effect of nickel ions released in a human body which when in contact with tissue leads to genotoxic, cancer as well as skin allergy [**75,76].**

The developments of newly stainless steels material with nickel free have been a target for biomedical application. The replacements of Nickel element can be done by utilizing Manganese and Nitrogen element which are all enhancing the formation of austenitic structure in SS material [**75,76**]. Since the newly developed lean Duplex stainless steel does not consist of nickel in their composition, can be applied for biomedical application due their outstanding properties over their counterpart ferritic and austenitic SSs

CHAPTER 3

MOTIVATION AND OBJECTIVES OF THE RESEARCH

Today, corrosion is a serious issue which is being faced by many industries in the world, from oil and gas sectors to food and medical sectors. The cost of corrosion in many industrial countries is estimated to be multi-billion dollars which is a big stake from GDP (Gross Domestic Profit) of these countries. The commonly used materials in many industrial sectors are stainless steels (SSs) which have good corrosion resistance properties. However, corrosion has still been regarded as the serious issue in these industries.

Duplex stainless steel has emerged to be an outstanding stainless-steel material due to its enhanced mechanical and corrosion properties contributed from dual phase structure of ferritic and austenitic stainless steel. It's properties such as high strength and high toughness gives DSS more superiority in comparison to their austenitic and ferritic counterparts respectively. Thanks to its excellence in pitting corrosion resistance and mechanical properties which have made DSS popular in many industrial applications such as automotive, marine, oil and gas, petrochemical and naval industries**.**

DSS alloys performance has been hindered by the formation of intermetallic phases at an elevated temperature which results in degradation of its corrosion resistance properties. The formation of intermetallic phases depletes alloying elements from DSS alloys composition such as Cr, Mo, N, Mn, Si, and Cu which are essential for corrosion resistance properties. Never the less, these phases such as Sigma, Nitride, MnS or MnO act as sites for corrosion initiation and propagation. Developments of DSS alloys have been also affected by nickel price volatility, which upsurges the demand for developing new Ni-free DSS alloys grades.

DSS alloys have acquired economic advantage due to the low amount of nickel or being replaced by Mn and N as austenite formers in their composition. However, Mn is not a strong austenite stabilizer as Ni, hence the addition of nitrogen which is also an austenite phase stabilizer**.** Nitrogen addition has a positive effect on pitting corrosion resistance, strength and retarding the sensitization of stainless steel. However, the solubility of Nitrogen increases as the Mn content increase**.** Mn content should be controlled due to the formation of intermetallic precipitates such as MnS. It is reported that the Mn increase decreases pitting corrosion resistance to formation MnS inclusion which initiates pitting formation. Mo has been added to enhance corrosion resistance as well as Si and Cu.

Therefore, the purpose of this work was to ***develop an economical duplex stainless steel with free or low Ni content to acquire better corrosion resistance properties comparable to that of standard AISI 304 stainless steel***.

This work will further investigate the corrosion performance of the newly developed DSS material by performing different corrosion measurements techniques such potentiodynamic polarization (PDP), electrochemical impedance spectrometry (EIS) and electrochemical noise analysis (ENA).

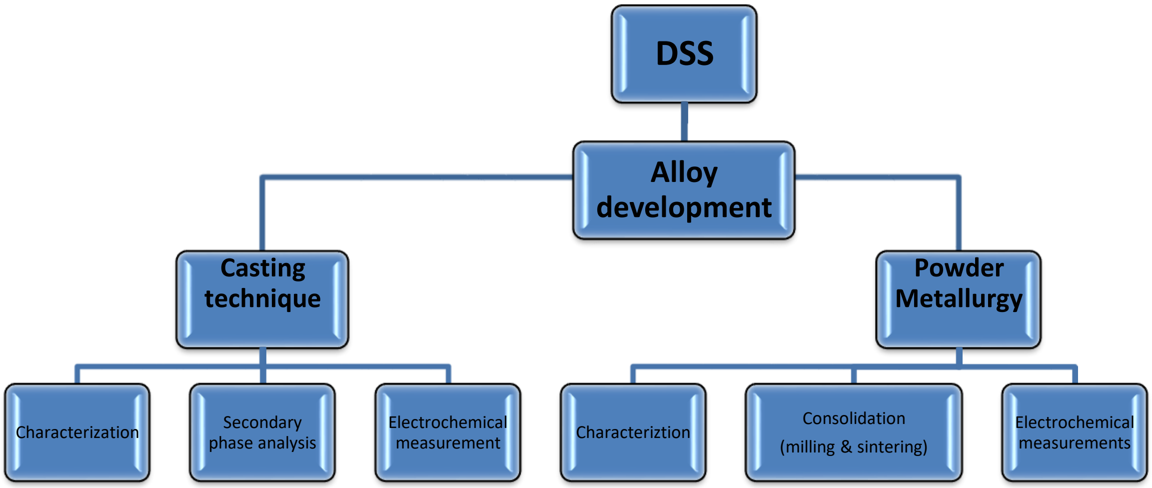

Fig.12. Flowchart showing the scope of the work.

CHAPTER 4

MATERIALS AND METHODOLOGY

4.1. Raw Materials

Cast and Powder metallurgy DSS alloys compositions begin with the mixing of pure elemental powder and pre-mixed powder of ferritic, austenitic and martensitic SSs. The mixture is then melted in furnace or mechanical alloyed to achieve homogenous mixed liquid or solid solution of the alloys. In this work, DSS composition was made from the elemental powder of Fe, Cr, Ni, Mn, Si, Mo and Cu with their respective particle size. These elements were all characterized by X-ray diffraction XRD to see properties before processing.

Table 2. Shows the alloying elements and their respective % purity and particle size

Element	**Purity (%)**	**Powder size for PM alloys**
Iron Fe	99	Fine < 100 mesh
Chromium Cr	99.95	100 mesh
Silicon Si	99	325 mesh
Nickel Ni	99.9	Fine
Molybdenum Mo	99.9	<150um
Manganese Mn	99.9	325 mesh
Copper Cu	99.9(electrolytic Cu)	Fine

4.2. Alloy design using Schaeffer’s diagram

DSS alloy design was selected based on the ferrite and austenite regions in Schaeffler’s diagrams in Fig.13 which is widely used in welding to determine ferrite and austenite phase content of the weld joint. This technique has been found to be more useful in welding to predict ferrite-austenite ratio in the in the composition of the designed DSS alloy [**21, 25,**

58]. The composition of DSS was calculated from the Ni equivalent and Cr equivalent in Schaeffer's diagram. Nickel is an austenite phase stabilizer which is added to help the formation of austenite phase in DSS by the help of the commonly used equation here below **[27, 31, 32**]. Other elements which enhance austenite phase formation includes Nitrogen, Manganese, and Copper

$$\text{Ni eq} = \%\text{Ni} + 0.5\%\text{Mn} + 20\cdot\%\text{N} + 0.25\cdot\%\text{Cu}$$

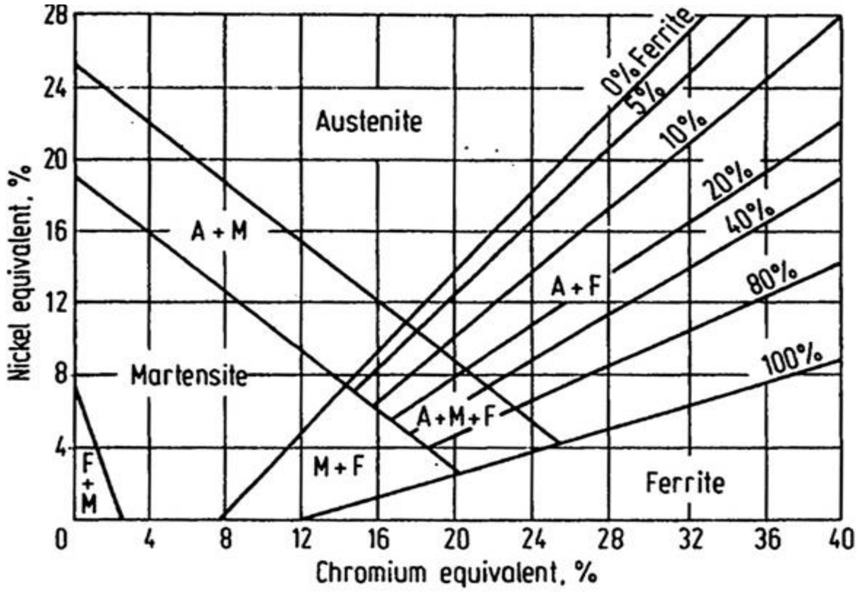

Fig.13. Schaeffer's diagram for prediction of DSS structure **[21].**

Table 3. Shows the chemical composition in wt. % of designed DSS alloys.

Designed Cast alloys	**Fe**	**Cr**	**Mn**	**Mo**	**Ni**	**Si**	**N**	**Cu**	**Cr$_{eq}$**	**Ni$_{eq}$**
Alloy 1	Bal.	18	6	1	0	1	0.22	0	18.6	8.3
Alloy 2	Bal.	18	5	1	0	1	0.22	1	18.2	8.1
Alloy 3	Bal.	18	4	1	0	1	0.22	2	18.6	7.9

Chromium equivalent which helps to stabilize ferrite phase formation is obtained by Cr equivalent formula below. The formula includes alloying elements which enhance ferrite formation such as Molybdenum Mo and Silicon Si **[27, 31].**

$$Cr\ eq = \%Cr + \%Mo + 1.5\%Si + 0.7\ \%Nb$$

$$\text{Pitting Resistance Equivalent Number (PREN)} = Cr + 3.3Mo + 30N = 27.9$$

Table 4. Shows the composition of the newly designed PM DSS alloys.

Designed PM alloys	**Fe**	**Cr**	**Mn**	**Mo**	**Si**	**Cu**	**Ni**	**N**	**Cr_{eq}**	**Ni_{eq}**
Alloy 1 (D1)	Bal.	18	6	1	1	0	0	0.22	19.5	8.5
Alloy 2 (D2)	Bal.	18	6	1	1	1	0	0.22	21	9
Alloy 3 (D3)	Bal.	18	3	1	1	0	3	0.22	21	10
Alloy 4 (D4)	Bal.	18	3	1	1	0	5	0.22	21	12

4.3. Cast alloy developments

Cast alloys were developed by casting technique in which the alloys named alloy 1, 2 and 3 were produced. The compositions of these alloys were designed with the help of Schaeffer diagram to get a duplex structured composed of ferrite and austenite structure **[64, 65].** The alloys were produced to obtain ingots through melting process conducted in vacuum arc melting furnace.

The ingots of 10mm were hot rolled to a thickness of 6mm and then followed by solution annealing, water quenching, cold rolling (35%) and subsequently solution annealed to release residual stresses and cold rolled again. To obtain microstructure of 60% austenite and 40% ferrite, the DSS alloys were solution annealed at 1120^{o}C. The solution annealing temperature was obtained by using Thermocalc software **[66].**

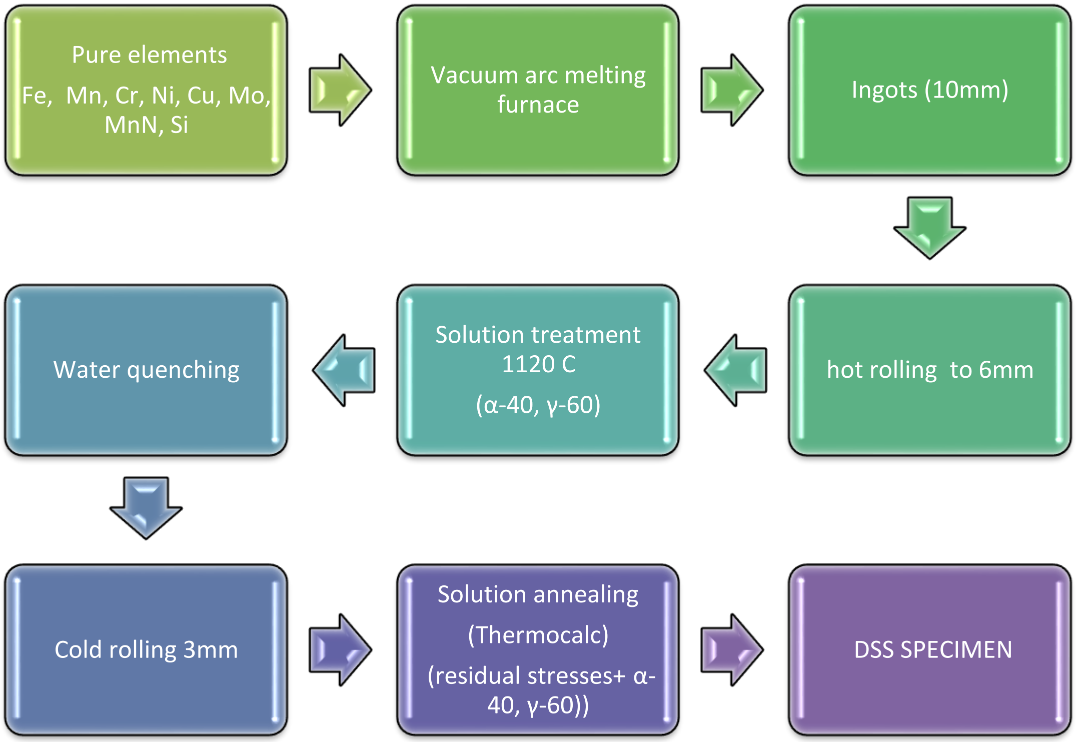

Fig.14. Shows process flow chart for cast DSS alloys production

4.4. Alloy development by Mechanical alloying (MA)

The process of Mechanical alloying involves the mixing and milling of the powder of the designed composition to achieve homogenous nano-particle sized powder alloy with a Duplex SSs structure after milling before sintering process. The alloys with nominal compositions of design 1, 2, 3 and 4 consolidated by mechanical alloying. The process variable to achieve an appropriate composition by MA were selected as shown in the table below. As explained in the previous chapter that the MA processes depend on several parameters to acquire the appropriate structure of nano-sized powder particles.

Table 5. Shows the process variables during mechanical alloying.

MILLING PARAMETERS FOR DUPLEX SS	
Milling type	Planetary ball milling
Atmosphere	Nitrogen
Process control agent (PCA-additives)	Stearic acid (1%wt)
Ball to powder weight ratio (BPR)	12 to 1
Milling time	20h
Milling speed (critical) (rpm)	300
Size of the balls used	15mm D chrome steel
Powder size after milling	Nano size (expected)

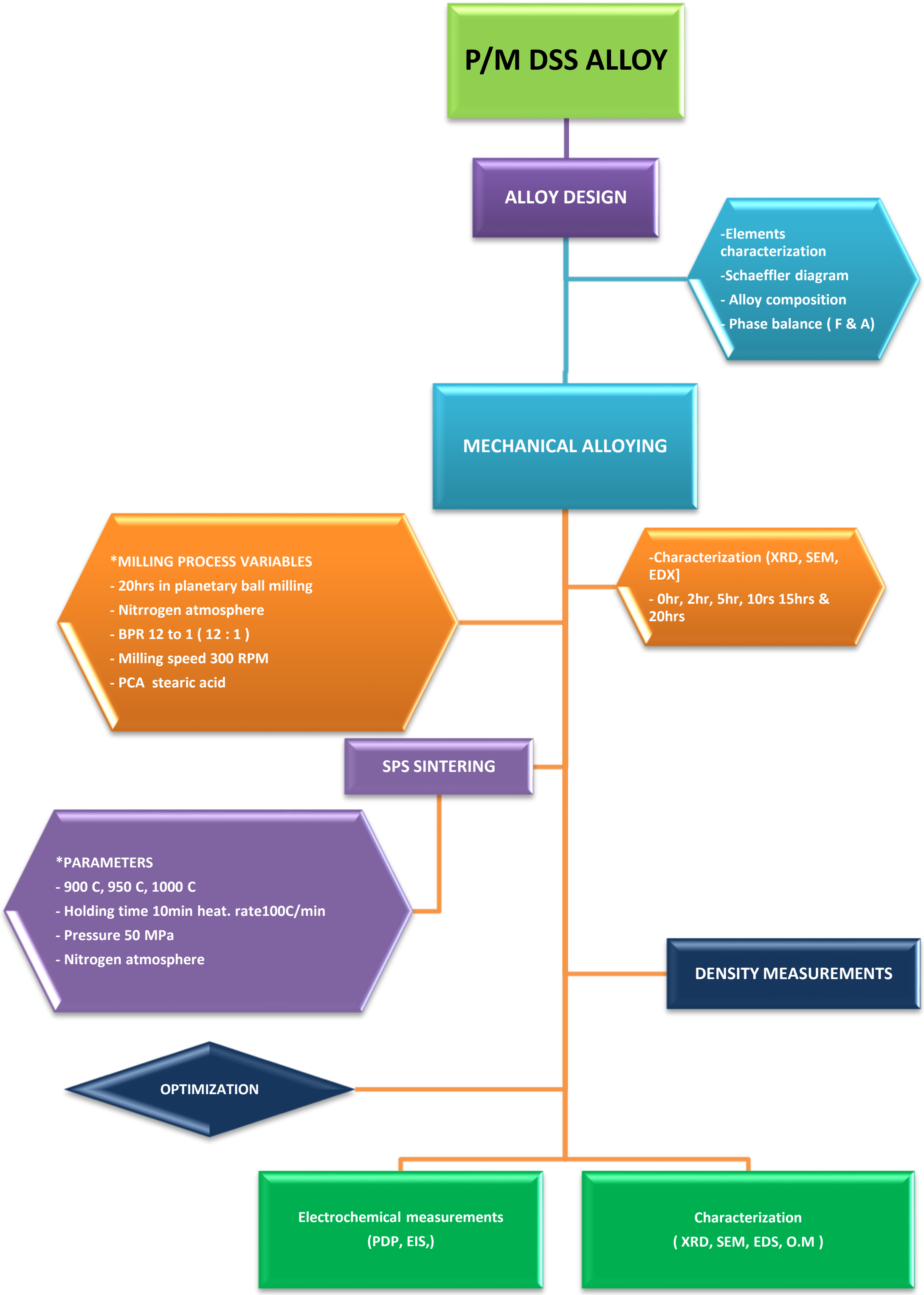

Fig.15. Schematic presentation of consolidation processes P/M DSS alloys.

The phase evolution study was then conducted after formation of a homogenous alloy of mixed powders. The study was done by XRD (X-Ray diffraction analysis) to determine the time for phase formation during MA, also the alloys compositions were determined EDS (Energy dispersive spectrometry). SEM (Scanning electron microscopy) was used to examine the morphology of the homogeneous alloy obtained from milled powder

4.5. Spark plasma sintering (SPS) technique

Spark plasma sintering technique was carried out for consolidation of ball milled powder of designed Duplex stainless steel alloys. The sintering process was conducted in a fully automated SPS machine (Type HP D-5, FCT Systeme, Rauenstein, Germany). The applied current of the SPS machine was passed through a 20mm graphite die which was used in holding the milled powders. The process parameters which influence the properties of sintered alloys includes sintering temperature, holding time, heating rate and pressure [**4, 48-51, 60-61]**

Table 6. Shows optimization parameters of spark plasma sintering of designed DSS alloys.

Temperature (^{0}C)	**Holding time(min)**	**Heating rate (degree per min)**	**Pressure MPa**
900	10	100	50
950	10	100	50
1000	10	100	50

For optimization, the SPS was carried out in a different range of temperature, holding time and pressure as reported in the literature review table 1. The parameters selected for SPS of milled powder of designed Duplex stainless steel alloys are presented as shown in the optimization table 6.

During spark plasma sintering, parameters were set, and the cycle of sintering started from the preparation of sample by adding and pressing alloys powder in the graphite die. The sintering circle starts from heating of powder in a graphite die at a selected heating rate. Then followed by holding time which sintering mechanisms such as necking and bonding occur for a specific time selected. Usually holding time varies from 5 to 15 minutes after reaching a selected sintering temperature. Lastly, a cooling process which takes a maximum of five minutes is taking place. The cooling process is performed with the help of inert gas, most of the time N_2 is preferred. The gas enters sintering chambers and provides cooling atmosphere around the graphite die. The chamber is then purged with air to release the vacuum and the sample is taken from graphite die.

4.6. Characterization of ball milled and Sintered specimen

Characterization of cast and powder metallurgy prepared sample were conducted by several techniques.

a. *Optical Microscope,*

FE-SEM, EDX, and XRD were used during to investigate the microstructure of sintered sample. The samples were firstly mounted, grinded, polished and then etched with glyceregia reagent to analyze the microstructure by an optical microscope.

b. *Scanning Electron Microscope and XRD*

Jeol FE-SEM equipment was used to study the microstructure phases through image analysis and later quantifying elemental composition by EDX technique. XRD (Bruker D8 advance) equipment was used to investigate the phases formed during ball milling and after sintering by SPS (spark plasma sintering). XRD spectrums were obtained over radiation 20-100° with a step size of 0.02°/min at 20Kv.

c. *Phase fraction analysis;*

Phase counting in the microstructure of duplex stainless steel was done by using standard manual point count method (ASTM E562). The etchant used during phase analysis was 40% KOH Electrolytic. Assessment magnification was conducted at 400X from the optical micrographs. The procedure includes merging of transparent grid over the image and the number of points which fall within the desired phase or microconstituent are counted. By the statistical analysis, the fraction of points which fall within the desired phase is revealed and the volume fraction is then calculated.

d. Lattice parameter and Crystalline size;

Lattice parameter and crystalline size calculations were later performed for ball milled powder and density for the sintered specimen. Lattice parameter was calculated for each ball milled powder picked for XRD (X-ray Diffraction) in a certain time interval of milling. Lattice parameter (a) of ball milled powder of DSS alloys were calculated by determining the d-spacing of highest Bragg's angle peak (110) and then using the equation $a = d^*\sqrt{(h + k + l)}$. h, k, and l are the Miller indices of Bragg's angle.

Crystallite size calculations were done for the highest diffraction peak using Scherrer equation as ($D = 0.94\lambda / \beta\cos\theta$) where β is a full-width half maxima (FWHM), D is the crystallite size, λ is the wavelength of the X-ray source
Density measurement was calculated by Archimedes principle through weight measurements with the help of density measurement kit provided by Mettler Toledo shown in the Fig.16. The weight of the sample in air and in water was calculated six times to ensure the reproducibility of the data.

e. Micro-hardness measurements;

The hardness of sintered sample was calculated the sintered samples which were hot mounted in Bakelite using Bhuler hot mounting machine and then ground and polished with alumina suspension. Micro-hardness values were obtained by using Bhuler Micro-Vicker hardness tester equipped with a diamond indenter. 500gf (gram-force) was used to load the specimen for 10 seconds and the average of 7 readings were recorded for each specimen and later an average micro-hardness value was calculated

4.7. Electrochemical investigations

Initially, the samples sintered by varying the sintering temperature, holding time was investigated to analyze the effect of sintering conditions on the corrosion properties of the designed Duplex stainless alloys. The effects of alloying elements in the composition on the corrosion behaviors of the alloys were investigated.

The Following are electrochemical techniques that were used to investigate the corrosion resistance of the designed DSS alloys produced by casting and sintering in 0.2M NaCl and 0.2M H_2SO_4 solution.

- Potentiodynamic polarization (PDP)/Tafel analysis
- Electrochemical impedance spectroscopy (EIS)
- Electrochemical Noise Analysis (ENA)

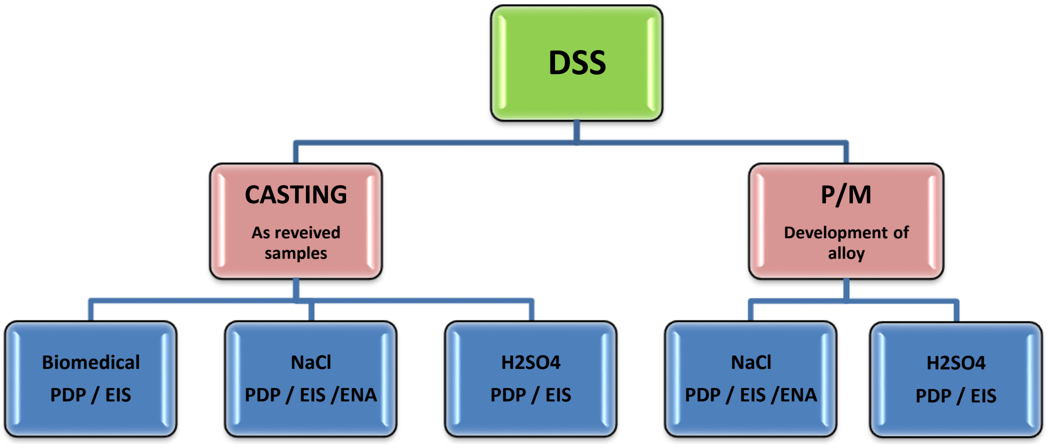

Fig.16(a). The flow chart of electrochemical investigations techniques

Fig.16 (b). Shows the schematic of the instrument using Archimedes principle to calculate density.

CHAPTER 5

CAST DUPLEX STAINLESS STEEL

5.1. Metallographic characterization of Cast DSS alloys

The microstructures of the designed alloys were analyzed through an Optical microscope and SEM images captured from SEM model: JEOL JSM-6064LV-80MM equipment at 20kV as shown in the Fig.16 and Fig.17 after being etched by glyceregia reagent (15 wt. % HCl, 10 wt. % HNO_3 & few drops of glycerin) for 2 minutes. Glyceregia reagent provides a good contrast of ferrite phase by using an optical microscope to examine the microstructure **[27]**. The ferrite and austenite content was calculated by the help of an image analyzer.

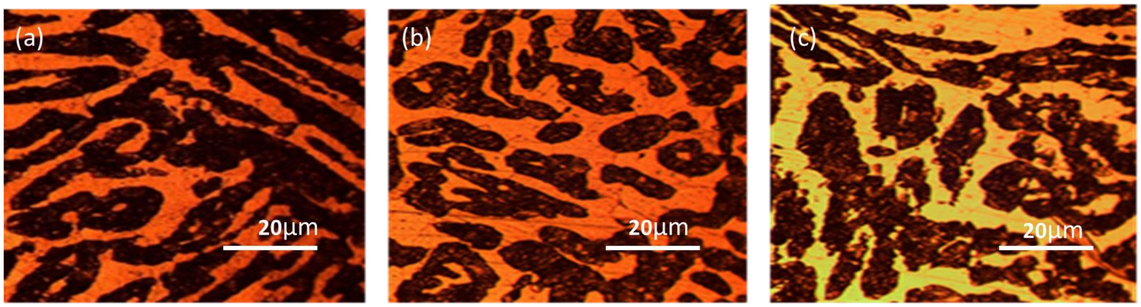

Fig.17(i). Shows the optical microstructure images of designed alloys, ferrite (dark) phase, and austenite (grey) phase (a) Alloy 1 (b) Alloy 2 (c) Alloy 3

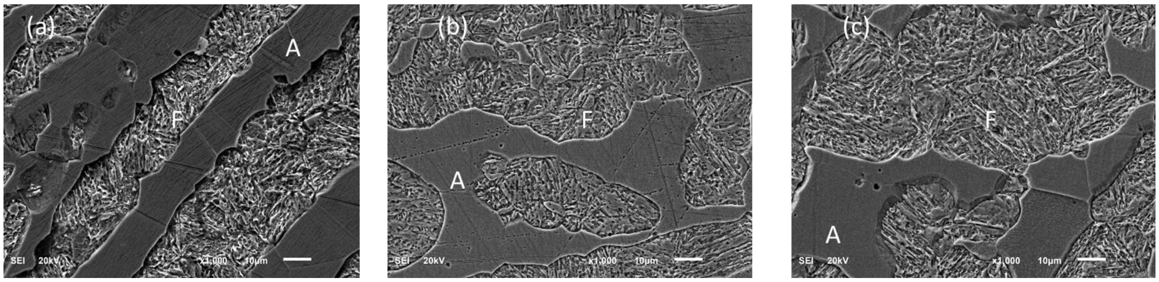

Fig.17(ii). Shows the optical images of designed DSS alloys, ferrite (F) phase and austenite (A) phase (a) Alloy 1 (b) Alloy 2 (c) Alloy 3

Optical microscope images showed ferrite and austenite phases were present in the alloys. The letter F which shows that the ferrite phase was etched by glyceregia reagent used while the austenite phase with letter A was not affected.

The microstructure phase count for the duplex structure was done by using standard manual point count method (ASTM E562). The sample was polished and etched with 40% KOH electrolytically. Assessment Magnification was selected at 400X from the optical micrographs before the counting. The counting was done by superimposing a transparent grid and later counts and percentage phase volume fractions were calculated.

Table 7. Showing calculated ferrite content in the DSS structure

Phase (%) in microstructure	Alloy 1	Alloy 2	Alloy 3
Ferrite (%)	39.1	36.8	36.3
Austenite (%)	60.9	63.2	63.7

5.2. Analysis of secondary phases in Cast DSS alloys

To analyze the precipitation of secondary phases in the designed DSS alloys, heat treatment (aging) at different temperature of 600°C, 700°C, 800°C, and 900°C were conducted in a furnace for 3 hours. Then the alloys were investigated by XRD (X-Ray Diffraction technique) to observe any presence of secondary phases such as sigma, chi, nitride etc.

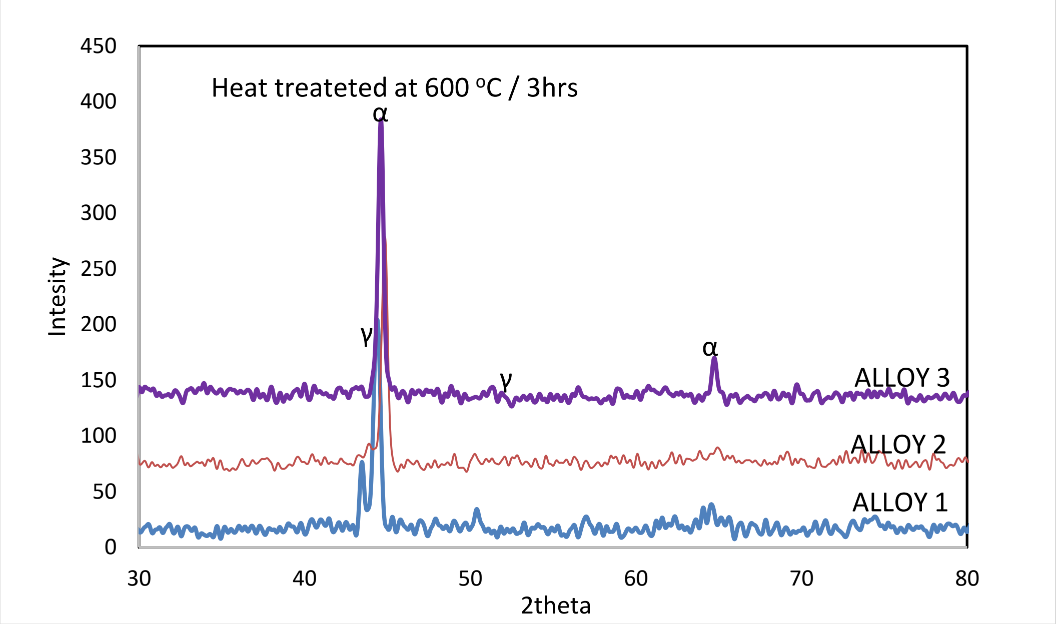

Fig.18. XRD results of designed cast DSS alloys after aged at 600°C.

The presence of any precipitate in DSS alloys contribute to the deterioration of corrosion properties as well as its mechanical properties. XRD results showed that no sigma phase was present in all DSS alloys in the Fig.18-21 at the temperature range of 600 to 900°C / 3hrs. The temperature range for studying the presence of Sigma phase occurrence is mentioned to be between 750°C and 900 °C [**4,33,39**]. Sigma phase is Cr-Mo rich phase which formed when a diffusion of Cr and Mo occurs from ferrite [**4].** Nucleation of sigma phase occurs between the ferrite-ferrite boundary and ferrite austenite boundary [**27,39**]. The depletion of Cr from ferrite phase cause deterioration of corrosion properties. The reason behind no formation of sigma phase can be attributed to the less amount of Cr and Mo incorporated in the composition of the alloy.

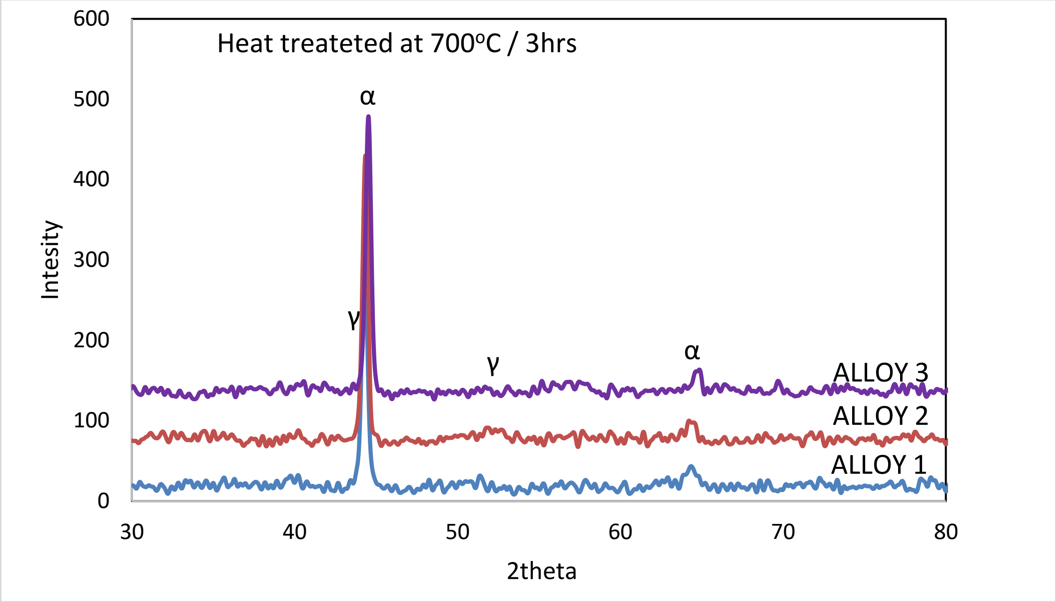

Fig.19. XRD results of designed cast DSS alloys after aged at 700^{o}C.

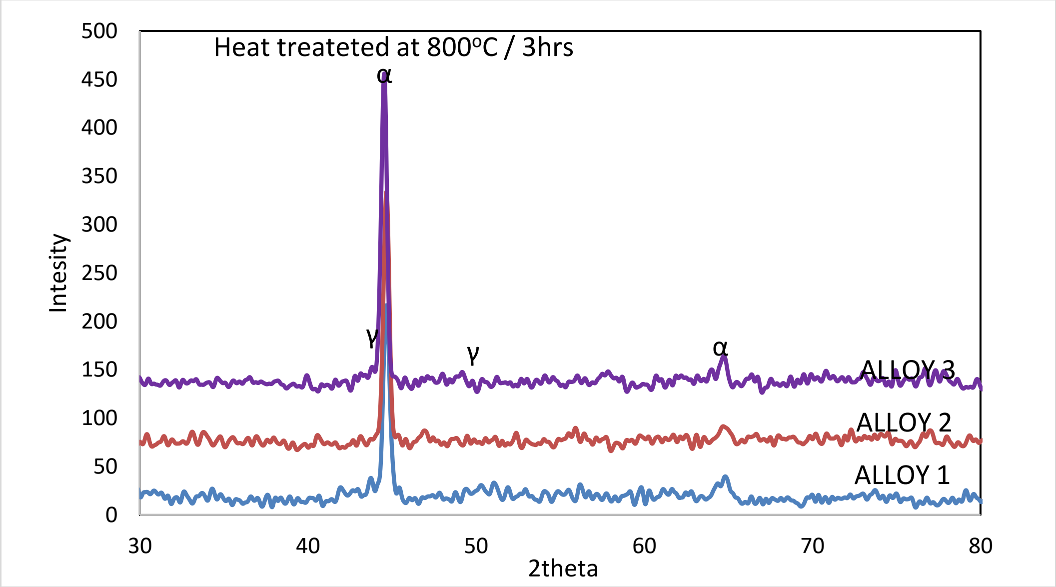

Fig.20. XRD results of designed cast DSS alloys after aged at 800^{o}C.

Chi precipitation occurs in mostly DSS alloys when exposed to high-temperature range between 700 ^{o}C and 850 ^{o}C. It is associated with negative influence on corrosion and mechanical properties as well **[33, 71]**.

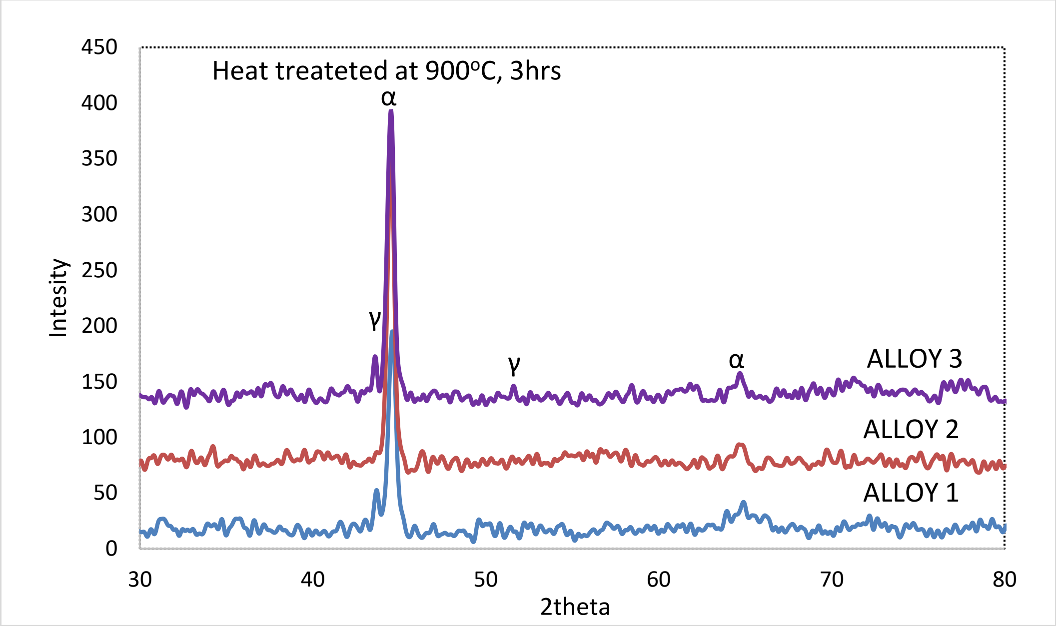

Fig.21. Shows XRD results of designed cast DSS alloys after aged at 900°C.

Fig.19-21 show the XRD results of designed DSS alloys aged at 700 °C, 800 °C, and 900 °C for 3 hours and no peak correspond to chi precipitates was observed on all DSS alloys. Chi phases also formed due to eutectoid reactions of ferrite phase into sigma, chi, and nitride precipitate. Chi phase composition structure consisting of Fe, Cr, and Mo, however, it has more of Mo amount than Cr [**27, 33, 39**]. The amount of chi phases is less than that of sigma phase during precipitation [**71**]. It can also be commented that the absence of Chi phase is due to less amount Mo and an appropriate amount of Cr as alloying elements in the DSS alloys.

The precipitation of nitride compound such as Cr_2N has been associated with the deterioration of corrosion properties of DSS alloys [**4,72].** Cr_2N compound in the DSS alloys is reported to be formed between 700 °C - 900 °C **[42,43]**. In the Fig.19-21 the XRD results show no nitride precipitates were formed such as Cr_2N when aged for 3 hours at 700 °C, 800 °C, and 900 °C. The formation of nitride occurs due to the high amount of nitrogen at elevated temperature. [**42,43**]. The absence of Nitride compound such as Cr_2N is attributed to the low amount of nitrogen in these designed DSS alloys.

5.3. Electrochemical measurements of Cast DSS alloys

The specimens soldered by using an electric gun; mounted, grinded up to 600 grit emery paper, then polished by alumina particles of 50 microns and later sealed in silicon tape for electrochemical analysis. The experiments were performed in a three-electrode cell (a specimen as a working electrode, a graphite counter electrode, and a saturated calomel reference electrode) was used during the tests. To remove the primary oxide film formed on the surface exposed the specimens were cathodically cleaned for 10 min at - 0.8 V_{SCE} . All the electrode potentials are referred to the SCE scale.

Potentiodynamic polarization tests were performed per ASTM G 5 at a scan rate of 0.5 mV/s. Metastable pitting events density at a passive region was determined in terms of electrochemical noise analysis (ENA) and electrochemical impedance investigations were performed using a GAMRY reference 3000 potentiostat /galvanostat /ZRA controlled by a personal computer at ambient temperature (25^oC).

The formation of Passive films on AISI 304 stainless steel and designed DSS alloys were performed potentiostatically at DC potentials selected based on the passive region of the anodic curve for 15min and then impedance measurements were conducted. Each electrochemical measurement was repeated at least three times. An excitation voltage of 10 mV (peak-to-peak) and an applied frequency ranging from 10 kHz to 10 mHz have been used. All the potential values in the text are relative to the SCE.

To minimize the external noise during electrochemical noise analysis (ENA), experiments were performed in a Faraday cage. E_{pit} is notoriously irreproducible and sensitive to specimen size, so experiments were performed 3–5 times to determine E_{pit} under exactly similar experimental condition. The critical pitting temperature of the alloys was measured per ASTM G48A.

The specimens with an exposed surface area of 0.2 cm^2 were used for polarization tests. The solutions used were 0.2M NaCl and 0.2M H_2SO_4 solutions which were de-aerated for 2h before the experiment started and then continuous de-aeration was performed throughout the experiment.

5.3.1. Potentiodynamic polarization (PDP)

Potentiodynamic polarization in H_2SO_4 solution;

The pitting resistance behavior of the alloy 1, 2 and 3 was studied in comparison with AISI 304SS in de-aerated 0.2M H_2SO_4 solution at room temperature. Fig.22 shows the comparison polarization curve of 304 SS and designed alloy 1, 2 and 3 with Cu content of 0, 1 and 2 wt% respectively. The potentiodynamic curve shows the pitting potential E_{pit} values of the designed DSS alloys similarly to that 304SS. In Fig.22 the passive current density i_{pass} for 304SS and 1wt% Cu of alloy 2 observed to be less in value than other alloys 1 and 3. Then 0 wt% Cu of alloy 1 showed less i_{pass} than alloy 3 of 2wt% Cu which showed the highest i_{pass} value. This indicates that 1 wt% Cu (Alloy 2) showed a good general corrosion resistance similar to that of 304SS by having low i_{pass} in comparison to Alloy 1 and 3. The i_{pass} for Alloy 3 with 2 wt% Cu showed an increase in i_{pass} which indicate that higher amount of Cu decreases corrosion resistance.

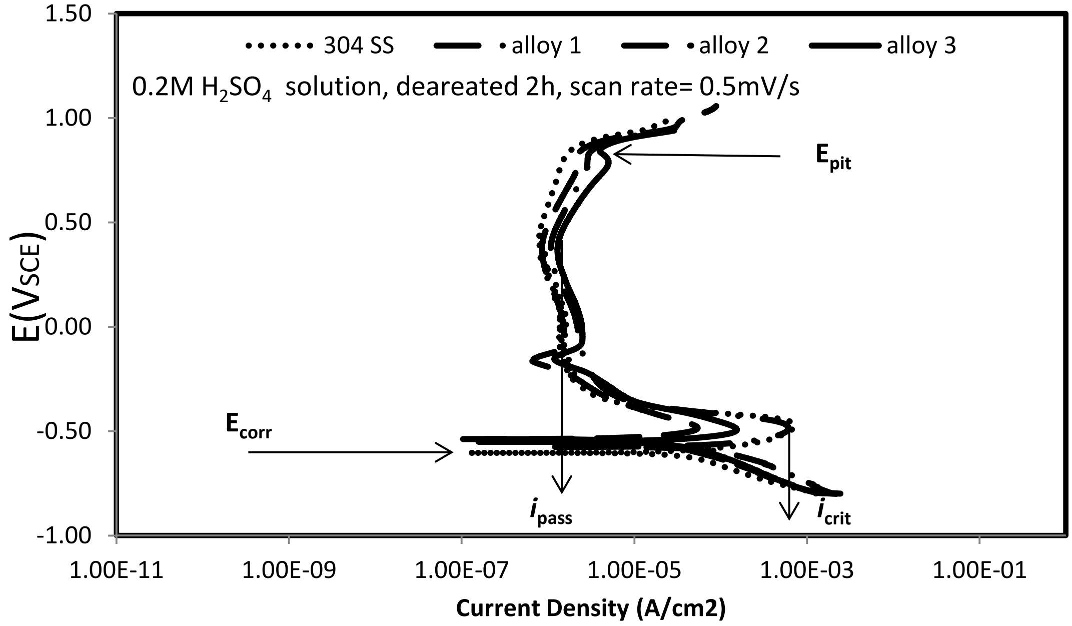

Fig.22. Polarization curve of designed alloys with 304SS in 0.2M H_2SO_4 solution.

The trend of corrosion potential E_{corr} was observed to have slightly increased as the Cu wt% content increases in the alloys. These results are in agreement with other literature [**35,67**]. Fig.23 shows the critical current density i_{crit} to be higher for Alloy 1 which has no

Cu and Alloy 3 with 2 wt% Cu showed higher i_{crit} than Alloy 2 with 1 wt % Cu. Alloy 2 observed to be good in general corrosion resistance than other designed DSS alloys in 0. 2M H_2SO_4 solution at room temperature. Addition of Cu decreases corrosion rate and improve corrosion resistance properties of an alloy [**68**]. In Fig.23 the critical current density decreases as the Cu was added to the composition.

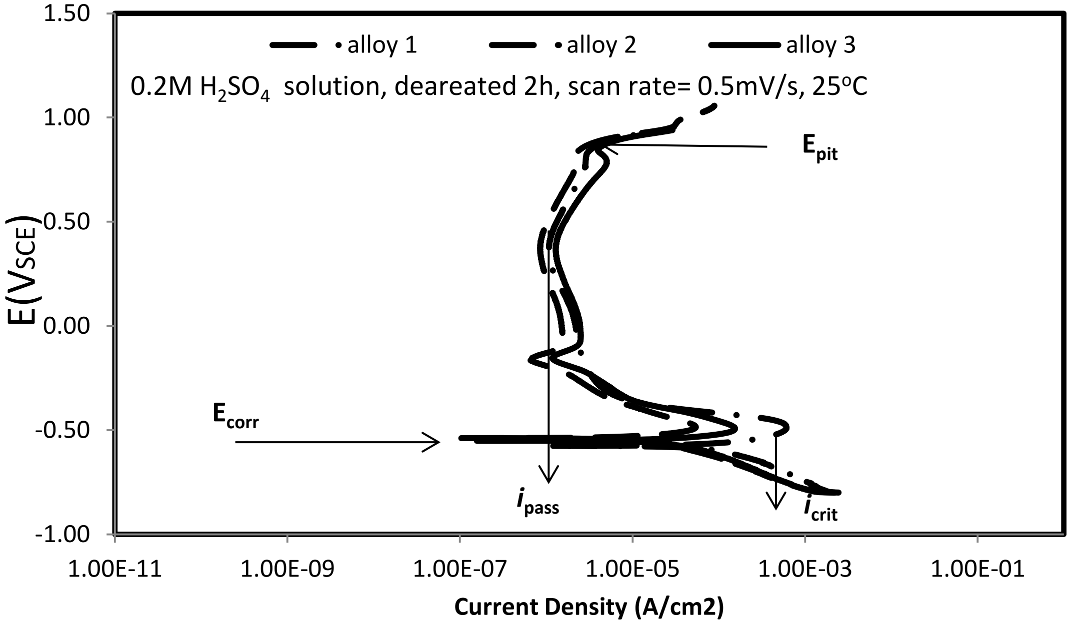

Fig.23. Polarization curve of designed alloys in 0.2M H_2SO_4 solution.

Potentiodynamic polarization in NaCl solution;

The polarization curve on the Fig.24 shows the pitting resistance behavior of the alloy 1, 2 and 3 were studied in comparison with AISI 304SS in de-aerated 0.2M NaCl solution at room temperature. The E_{pit} of 304 SS is slightly higher than designed DSS alloys and the variation of Cu content had no effect on the E_{pit} of the DSS alloys. The passive current density of Alloy 2 observed to be less than other alloys which indicates its better corrosion resistance than other alloys in Fig.25. Alloy 3 with a higher amount of Cu content shows higher passive current density which indicates decreases in its corrosion properties due to increase in Cu content. The corrosion potential E_{corr} values seem to increase as the Cu content increases. It is reported that **[68, 69]** the effect of Cu on the stainless steel exposed in chloride environment is not clear. Cu has been reported to increase the pitting corrosion resistance, crevice corrosion as well as reducing corrosion rate, however, other researchers have been reported on the negative of Cu on pitting corrosion resistance and corrosion rate.

The tendency of Cu to have both undesirable and beneficial on the corrosion properties of stainless steel have been associated with the different role of Cu in the chloride media. During corrosion of steel anodic dissolution occurs and Cu deposits appear to be on the surface of the corroded area.

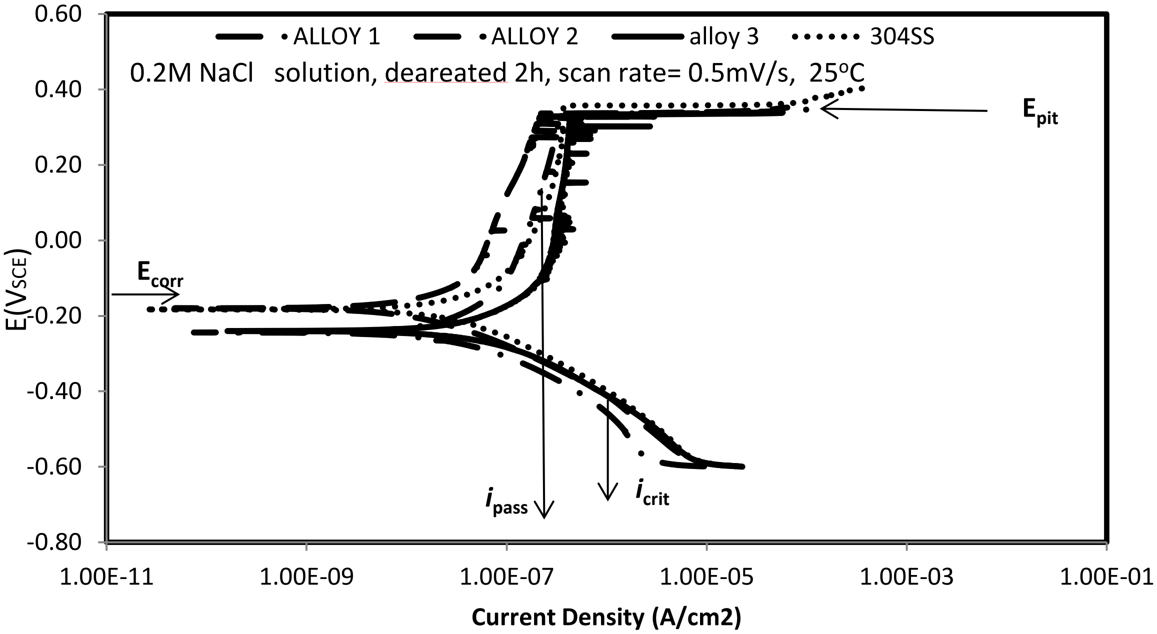

Fig.24. Polarization curve of DSS alloys with 304SS in 0.2M NaCl solution.

These deposits of Cu tend to suppress further dissolution of metal, however, the stability of Cu deposits is yet to be clarified due to the formation of complex ions such as $CuCl_2^-$in a chloride media [**68-70**]. However, it has been reported that Cu alloying element has undesirable properties which make it act as a cathode when deposited on the steel surface during anodic dissolution hence increases corrosion rate [69].

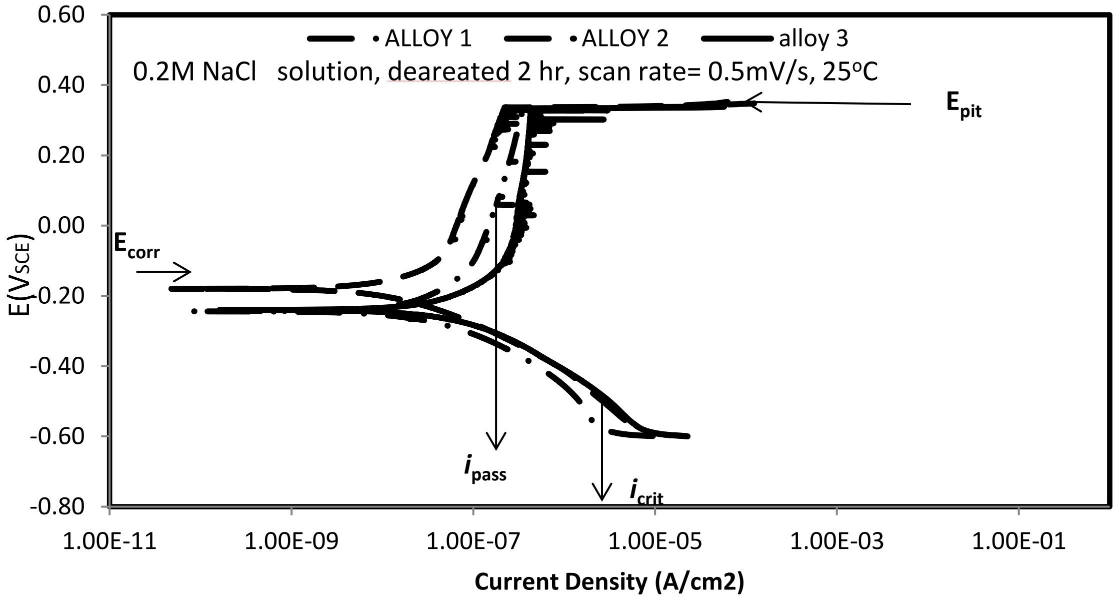

Fig.25. Polarization curve of designed DSS alloys in 0.2M NaCl solution.

Table 8. Values of E_{corr}, $E_{pit,}$ and i_{corr} from potentiodynamic polarization test in 0.2M acidic and chloride solution

Designed alloys	**0.2M H_2SO_4 solution**					**0.2M NaCl solution**			
	E_{corr} (mV_{SCE})	**E_{pit} (mV_{SCE})**	**i_{corr} (A/cm^2)**	**i_{pass} (A/cm^2)**	**i_{crit} (A/cm^2)**	**E_{corr} (mV_{SCE})**	**E_{pit} (mV_{SCE})**	**i_{corr} (A/cm^2)**	**i_{pass} (A/cm^2)**
Alloy 1	-578	835	1.0 E-04	9.1 E-07	4.0 E-04	-222	334	7.5 E-08	1.6 E-07
Alloy 2	-538	850	2.4 E-05	8.6 E-07	8.9 E-05	-192	340	4.8 E-08	8.3 E -08
Alloy 3	-550	840	2.8 E-05	1.3 E-06	1.2 E-04	-220	336	1.61 E-07	3.6 E-07
304SS	-610	855	1.1 E-05	8.0 E-07	4.3 E-04	-195	358	2.4 E-08	2.0 E-07

5.3.2. Electrochemical Impedance Spectrometry

Fig.26 and Fig.28 represent the EIS Nyquist plots of designed DSS alloys and 304SS obtained at open circuit potential in the deareted 0.2M H_2SO_4 and 0.2M NaCl solution respectively. The experiments were performed in one minute at open circuit delay after cleaning of the oxide layer at a negative potential at - 0.8 V_{SCE} for 5 minutes. The curve of Nyquist plots provides useful information of electric double layer formed between the substrate of material when in contact with solutions. The details obtained from the curve includes capacitance, charge transfer resistance while the magnitude of the charge transfer is presented by the diameter of the curve [**93**]. The spectra diameter is directly proportional to the magnitude of polarization resistance of the material.

The results of EIS in 0.2M H_2SO_4 solution for designed alloys and 304SS shows that the alloy 1 and 3 has lower arc diameter than alloy 2 and 304SS which describe that the later have good corrosion resistance than the former. Alloy 2 and 304SS have shown a similar magnitude of polarization resistance which was larger than alloy 1 and 3. The value of polarization resistance was obtained by the simplex fitting method in Fig.26 (b) as shown in table 9 and equivalent circuit in Fig.27. The results are in agreement with the potentiodynamic polarization curve (Fig 22) in 0.2M H_2SO_4 solution. The passive film stability of stainless steel in acidic medium is attributed to the slower dissolution of chromium-rich oxide [**94].** However, the effect of Cu content has been reported to have an influence on the passive behavior of stainless steels. Alloy 2 with optimum Cu content showed higher polarization resistance in comparison to alloy 1 and 3. The results point out on the positive effluence of Cu on the impedance spectra of stainless steel containing Cu which has been reported by several researchers. The presence of Cu on the passive film suppresses the anodic dissolution which in turn increases the polarization resistance **[95,96]**

In the Fig.28 the EIS response of the designed alloys and 304SS in deareted 0.2M NaCl solution at open circuit potential was obtained as shown by the spectra. The Nyquist plot exhibit a one-time constant capacitive behavior of the alloys represented as a semicircle. The polarization resistance gives a measure of corrosion resistance in the solution which is inversely proportional to the corrosion rate. In the Fig.28 the spectra of 304SS appear to be larger compared to designed alloys which indicate that, 304SS shows higher polarization resistance R_p than designed alloys. The values of R_p was obtained during fitting as shown in the Fig.28 (b) and table.9 as well as the corresponding equivalent circuit in Fig.29. The designed Alloy 2 has the highest spectra i.e higher polarization resistance than other Alloys 1 and 3. The reason Alloy 2 to have better polarization resistance is attributed to its optimum amount of Cu content in comparison to Alloy 3. Cu has been reported to increase the stability of passive film by suppressing anodic dissolution [**68-70**], however, it was reported by Ujiro [**68**] that chloride ions decrease the stability of Cu deposited on the passive film.

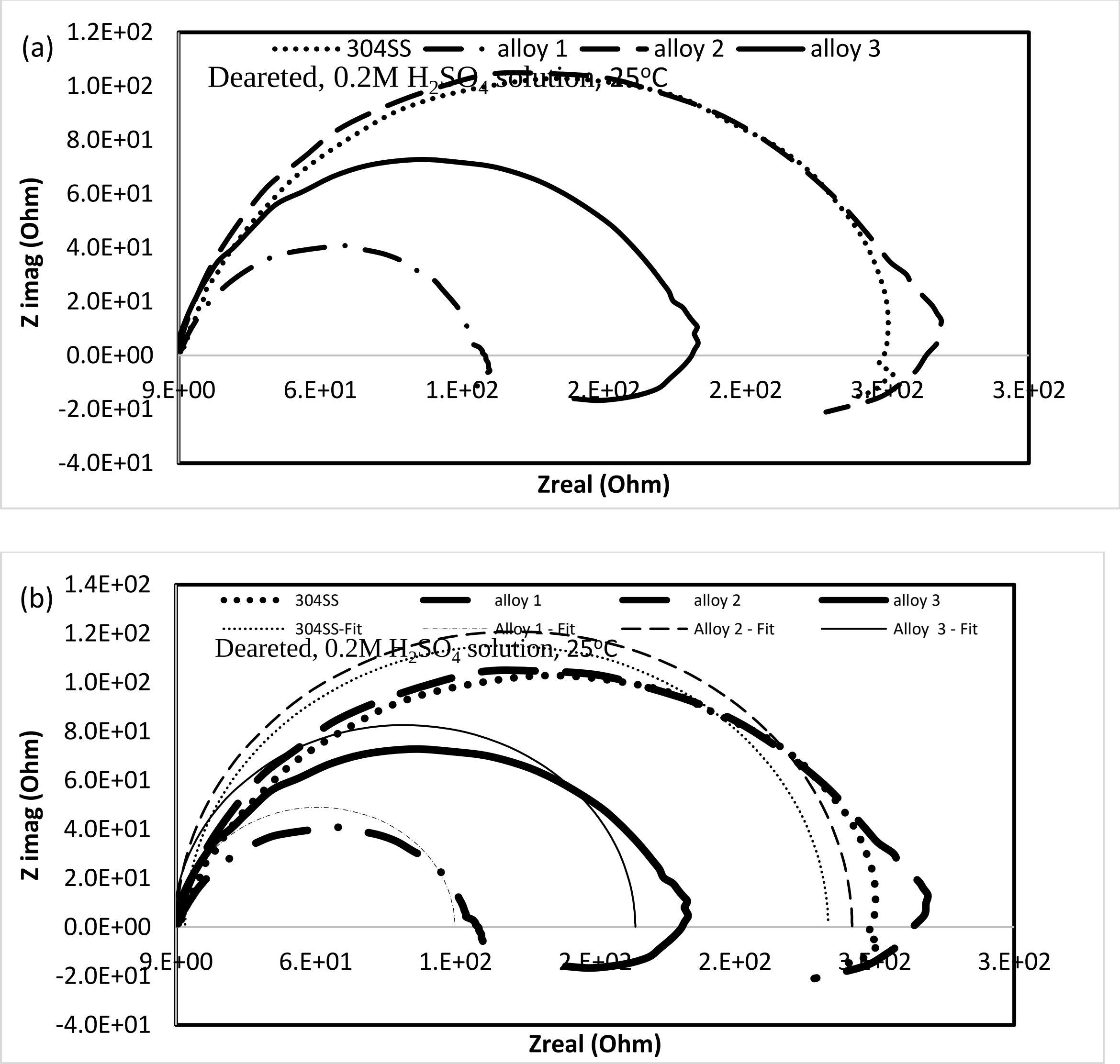

Fig.26. (a) EIS results and (b) Fitting of Designed DSS alloys with 304 SS in H_2SO_4 solution

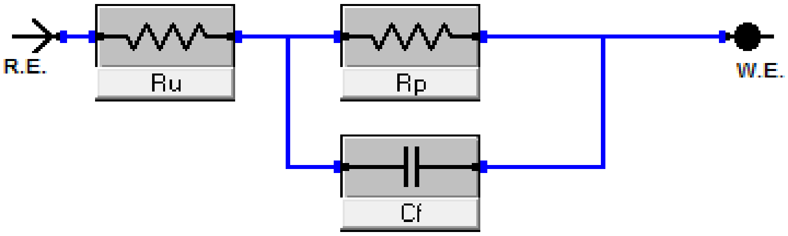

Fig.27. Equivalent circuit of the Nyquist plots of DSS alloys with 304 SS in H_2SO_4 solution

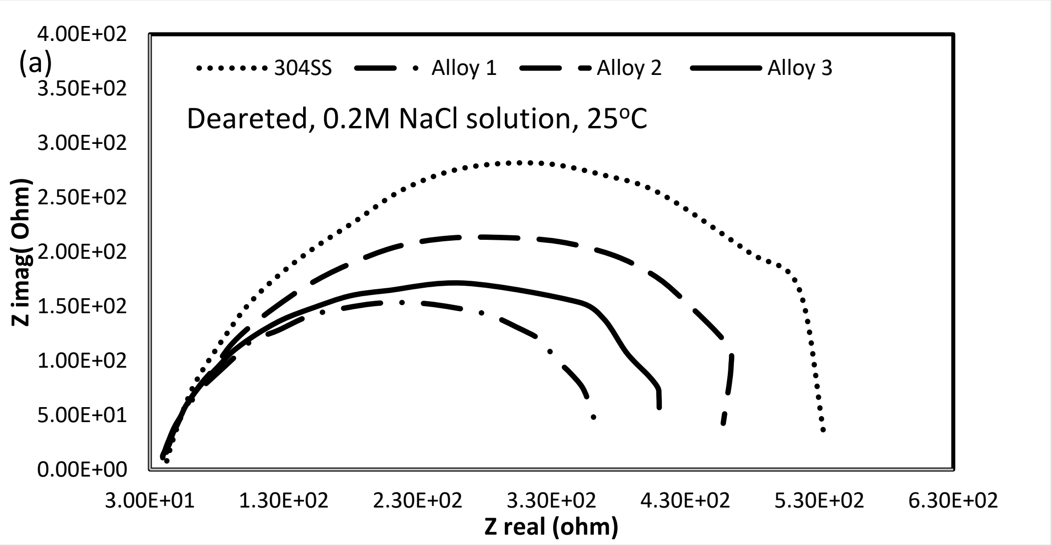

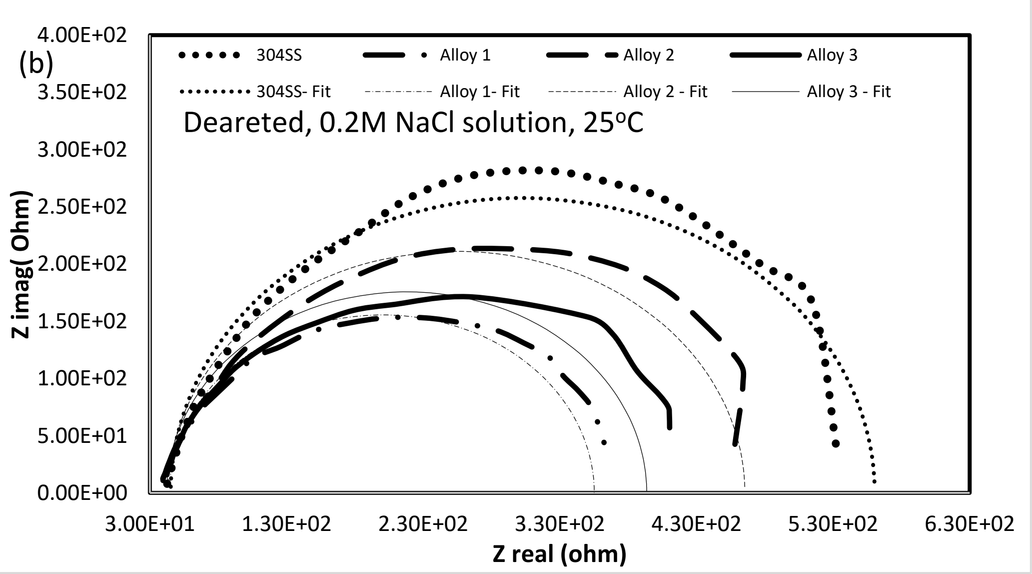

Fig.28. (a)EIS results and (b) Fitting of Designed DSS alloys with 304 SS in NaCl solution

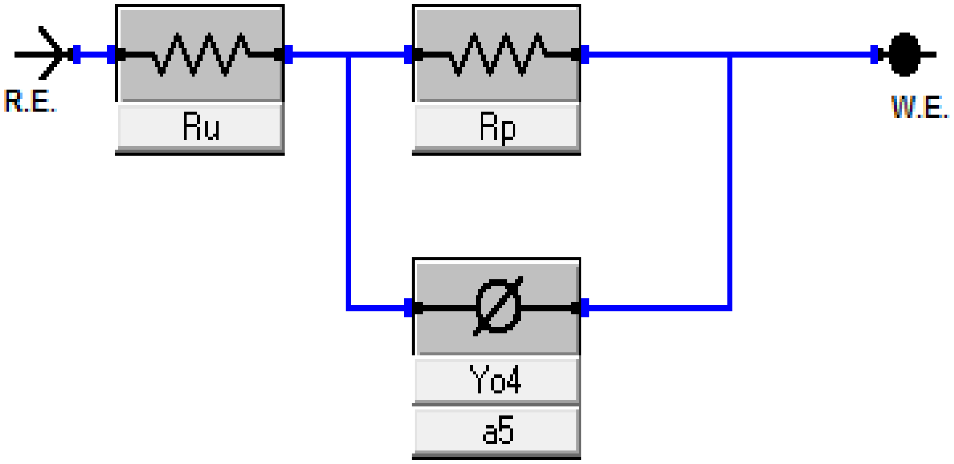

Fig.29. Equivalent circuit of the Nyquist plots of DSS alloys with 304 SS in NaCl solution

Table. 9. Polarization resistance Rp from Impedance analysis test at open circuit potential in 0.2M acidic and chloride solution

Designed alloys	0.2M H_2SO_4 solution		0.2M NaCl solution	
	Polarization resistance, Rp (Ω)	Solution resistance, Ru(Ω)	Polarization resistance, Rp(Ω)	Solution resistance, Ru(Ω)
Alloy 1	97.94	10.87	371.50	35.16
Alloy 2	231.70	9.22	492.40	36.89
Alloy 3	165.20	8.13	415.60	34.82
304SS	234.50	12.67	579.50	41.29

5.3.3. Electrochemical noise analysis

Metastable pitting was observed in the Fig.24 and 25 at anodic region during potentiodynamic polarization of designed alloys carried out in the 0.2 M NaCl solution. The current transient peaks in the anodic region were observed before pitting potential of the alloy 1, 2 and 3. Analysis of current noise was performed by ESA480 data acquisition software in Gamry. The voltage bias was set at 150mV which is the range of passive region after formation of a passive film at 150mV$_{SCE}$ potentiostatically. The noise analysis experiments were performed at a time range of 30 minutes and repeated more than 3 times to ensure the reproducibility under potentiostatic condition. During metastable pitting, current noise is generated and analyzed to investigate the pitting and microscopic pit formation, growth and their repassivation behavior [**13,69**].

The metastable pitting events appeared in the Fig.30,31,32 and 33 for 304SS, Alloy 1, Alloy 2 and Alloy 3 respectively. The current versus time graphs in the figures mentioned above show the currents spikes i.e current transients, which is considered to be formation, growth, and repassivation of a metastable pit [**13,69**]. A sharp increase in current accompanied by a sharp decrease of potential signifies pit initiation process resulted from the breakdown of a protective passive film [**69**].

In Fig.30, the metastable pitting was not clearly seen during noise analysis of 304SS. However, Alloy 2 showed less current spike (Fig.32) than Alloy 1 and 3 (Fig 31 and 33 respectively). Alloy 2 seems to be less susceptible to metastable pitting than Alloy 1 and 3. It is clear reported that higher Mn initiates pit formation [**13**] and Cu increase susceptibility to pitting in previous works [**69**]. Alloy 1 has a higher amount of Mn content compared to Alloy 1 and 2, also Alloy 3 has a higher amount of Cu compared to other two Alloys. Increase in Mn content leads to more chances for the formation of Mn (sulfide and oxide) inclusions. **[6,13,56,69].** The increase in Mn inclusions eventually decreases corrosion resistance of the alloys. Cu has been reported to have a tendency of reducing the repassivation rate by increasing the current transient’s charges [**69**]. Alloy 2 seems to have less metastable pitting events which can be attributed to the optimum amount of Mn and Cu in the alloy.

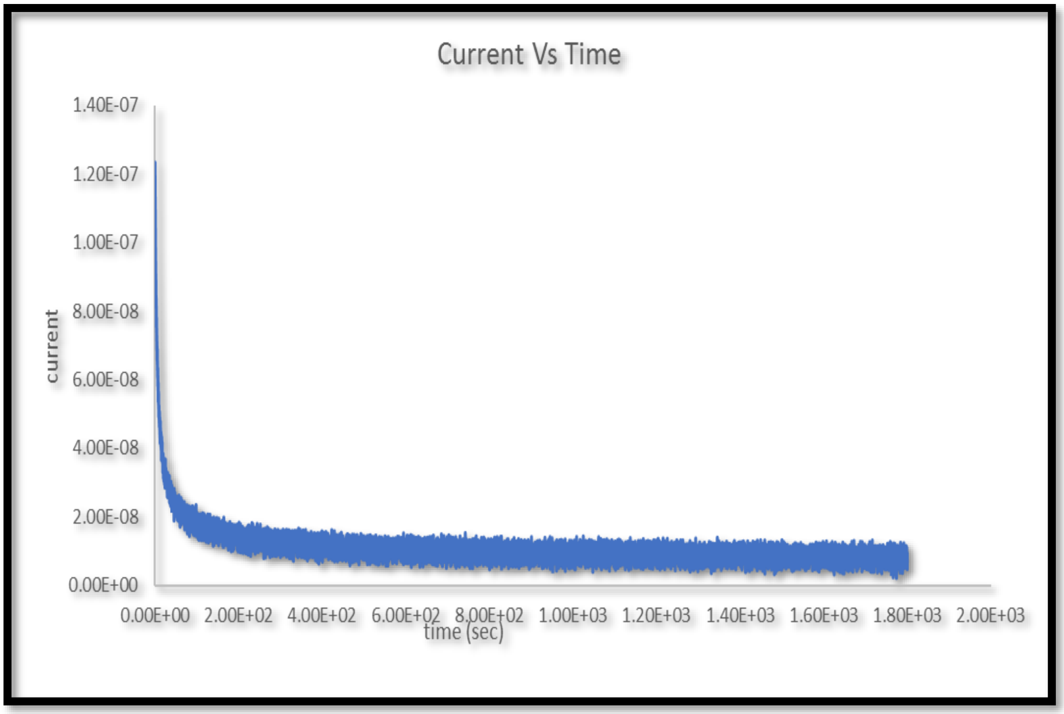

Fig.30. ENA results of film formed on 304 SS in NaCl solution

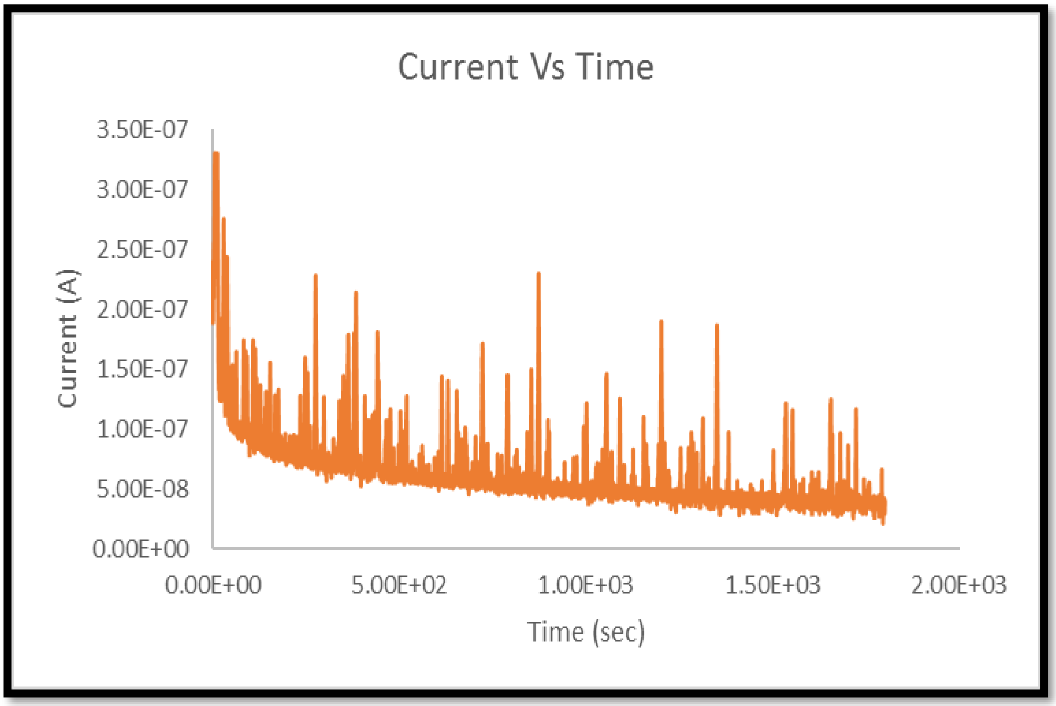

Fig.31. ENA results of film formed on Designed DSS Alloy 1 in NaCl solution

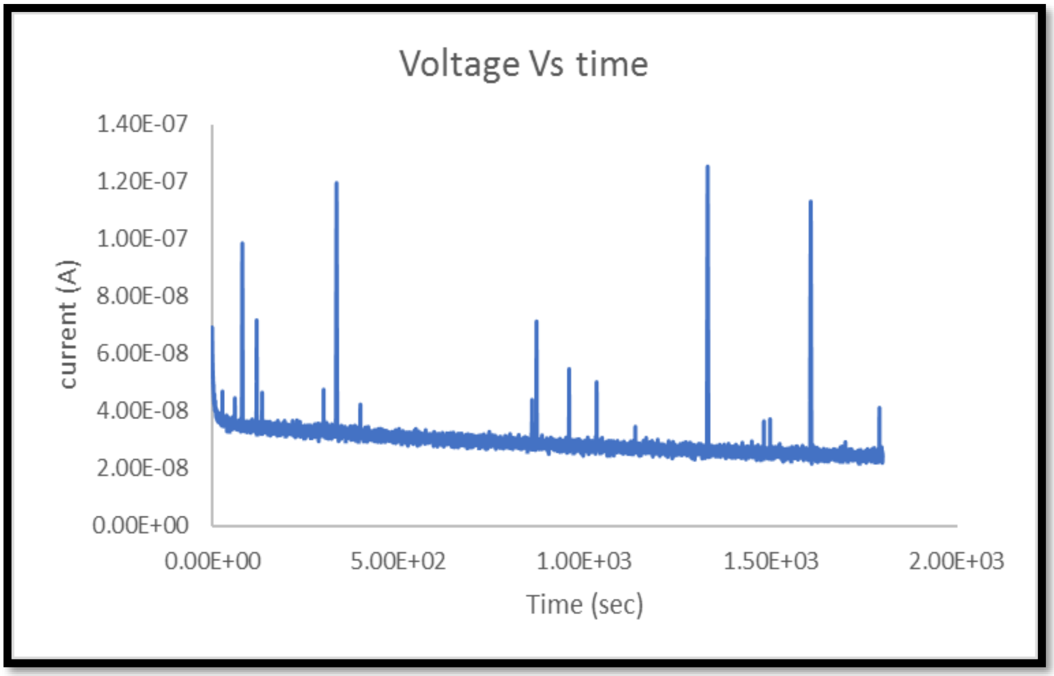

Fig.32. ENA results of film formed on Designed DSS Alloy 2 in NaCl solution

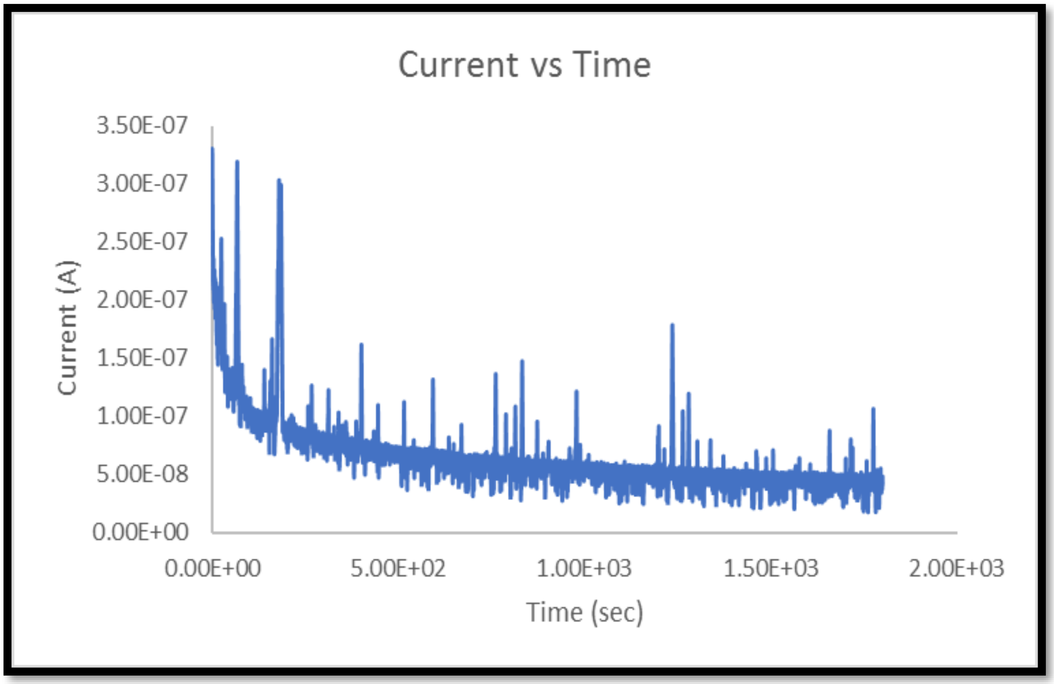

Fig.33. ENA results of film formed on Designed DSS Alloy 3 in NaCl solution

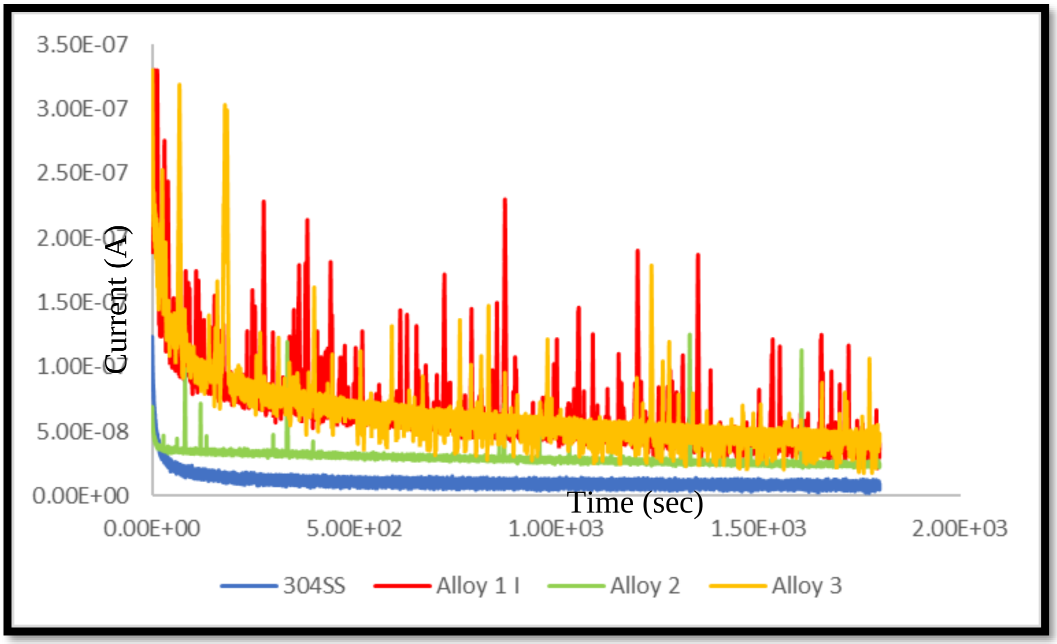

Fig.34. ENA results of the passive film formed on Designed DSS alloys with 304 SS in NaCl solution.

5.4. Analysis of Cast DSS in Simulated body fluid for Biomedical applications

Biomedical application of stainless steel has been widely used in the replacement of human body part such as the elbow, knee, dental structure, hip bone as well as valves in the ventricles of the heart [**74**]. The ability of Duplex stainless steel to passivated due to Cr content with biocompatibility properties, appropriate density, good toughness, workability as well as its non-ferromagnetic properties [**74-77**] make it among the material for biomedical applications. Due to the harmful effect of Nickel ions release [**75,76,78**]in the human body our cast DSS alloy with no nickel content emerge to be an appropriate choice for biomedical applications.

The newly developed cast DSS alloys with no amount of nickel in the composition were tested in the artificially prepared simulated body fluid (with the SBF composition in Table 10) for electrochemical corrosion behavior to ensure their compatibility in biomedical applications. The electrochemical corrosion resistance characteristics of the DSS alloys were compared to that of standard AISI 304SS. Potentiodynamic polarization (PDP) and

Electrochemical Impedance spectrometry (EIS) were performed at human body temperature 37°C and at room temperature measured at 20°C. In addition to that, the electrochemical measurements were also performed under different immersion time of 1, 12 and 24 hours at room temperature at a 7.35pH.

Table 10. The composition of simulated body fluid (SBF) at pH 7.35

Reagent	**Amount**
NaCl	7.996 g
$NaHCO_3$	0.350 g
KCl	0.224 g
$K_2HPO_4 \cdot 3H_2O$	0.228 g
$MgCl_2 \cdot 6H_2O$	0.305 g
1M-HCl	40 mL
$CaCl_2$	0.278 g
Na_2SO_4	0.071 g
$(CH_2OH)_3CNH_2$	6.057 g

5.4.1. Electrochemical properties analysis at 37°C body temperature

Potentiodynamic polarization in SBF solution

The potentiodynamic polarization experiment for DSS alloys and 304SS were performed in deareted SBF solution at 37°C after immersion duration of 1 hour under OCP at a scan rate of 1mV/sec. After 1h immersion, the steady conditions were obtained and the potentiodynamic polarization scan was carried out to investigate the formation and stability of protective passive layer of these alloys in the SBF solution. In the Fig.35. 304SS showed higher E_{corr} values than that of DSS alloys, however, the pitting potential E_{pit} values for all alloys were almost similar. The passive current density was observed to be similar for all DSS alloys and 304SS as well. However, alloy 2 shows higher passive current density than other DSS alloys and 304SS. The cathodic behavior of all alloys in the Fig.35 was similar.

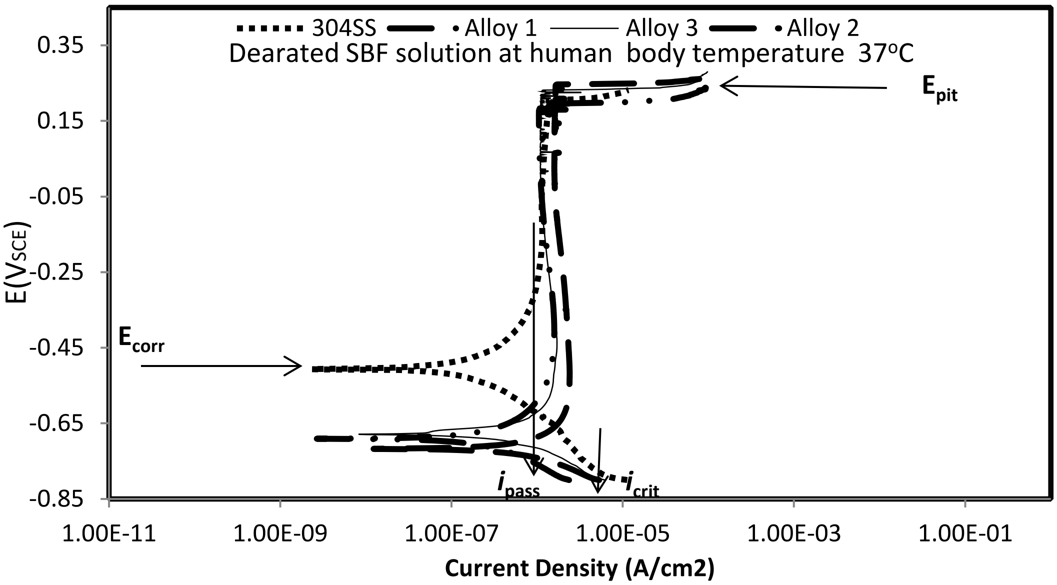

Fig.35. Potentiodynamic polarization curves of DSS alloys and 304SS in SBF at human body temperature.

The higher E_{corr} value of 304SS in SBF is attributed to the higher nickel content than other DSS alloys. Nickel content increases the E_{corr} value as the amount increase [78]. The pitting potential E_{pit} value of the DSS alloys depict that alloy 2 shows a slightly higher Epit value than other DSS alloys. Similarly, alloy 2 was observed to have higher current density than other alloys. This behavior can be attributed to the Cu-content of alloy 2 which is also reported [68,78] to have influence in the modification of thermodynamic properties due to uneven distribution on the surface of stainless steel.

Electrochemical Impedance spectrometry EIS in SBF solution

The impedance spectra of the DSS alloys and 304SS in SBF solution at 37°C were obtained after 1h immersion and followed by EIS experiment at open circuit potential, OCP. The Nyquist plots and bode curves are presented in the Fig.36 (a) and (b) respectively. The Nyquist plots show the passive behavior of 304SS and DSS alloys with larger values of real and imaginary components. The impedance values can be seen to increase in the order of Alloy 1 < Alloy 2 < Alloy 3 < 304SS.

According to the curves in Fig.36 (a), 304SS showed higher impedance values than DSS alloys. This is attributed to the composition of 304SS which contain a higher amount of nickel which helps in the passivity of the material **[78].** DSS alloys showed a good variation in the impedance value according to Mn and Cu content of the alloys. The amount of Mn decreases from alloy 1 > Alloy 2 > Alloy 3, however, the Cu content increases from alloy 1 < Alloy 2 < Alloy 3. Mn is reported to have a negative influence on the corrosion properties **[6,13,56,69],** hence as the Mn decreases the higher values of impedance was recorded. Similarly, the increase in impedance values was noted as the Cu content increases. Cu is reported to have both negative and beneficial effect on the corrosion properties of stainless steel **[68-70].** Copper is reported to suppress the anodic dissolution of stainless steel thus improves the stability of the passive layer.

Fig.35 (b) (i&ii). Shows EIS bode plots after immersion of 1hr at 37°C at 7.35pH conditions. The change in impedance response from bode plots shows a resistive behavior at higher frequencies, however, from middle to low frequencies a capacitive behavior was observed. 304SS showed an increase impedance at low frequency than DSS alloys. A bode-phase plot represents a one-time constant phase element conditions. Based on this observation an equivalent circuit of CPE in Fig.37 was established to simulate the measured impedance value in SBF solution presented in Table 10(b). The Equivalent circuit composed of model parameters such as polarization resistance Rp, solution resistance Rs, *n* represents a coefficient related with the homogeneity of the system and pseudocapacitance of the system Y_o (where n=1 for an ideal capacitor) **[79]**. The CPE impedance representation is given by

$$Z_{CPE} = 1/Y_o(j\omega)^n \qquad \textbf{[79]}$$

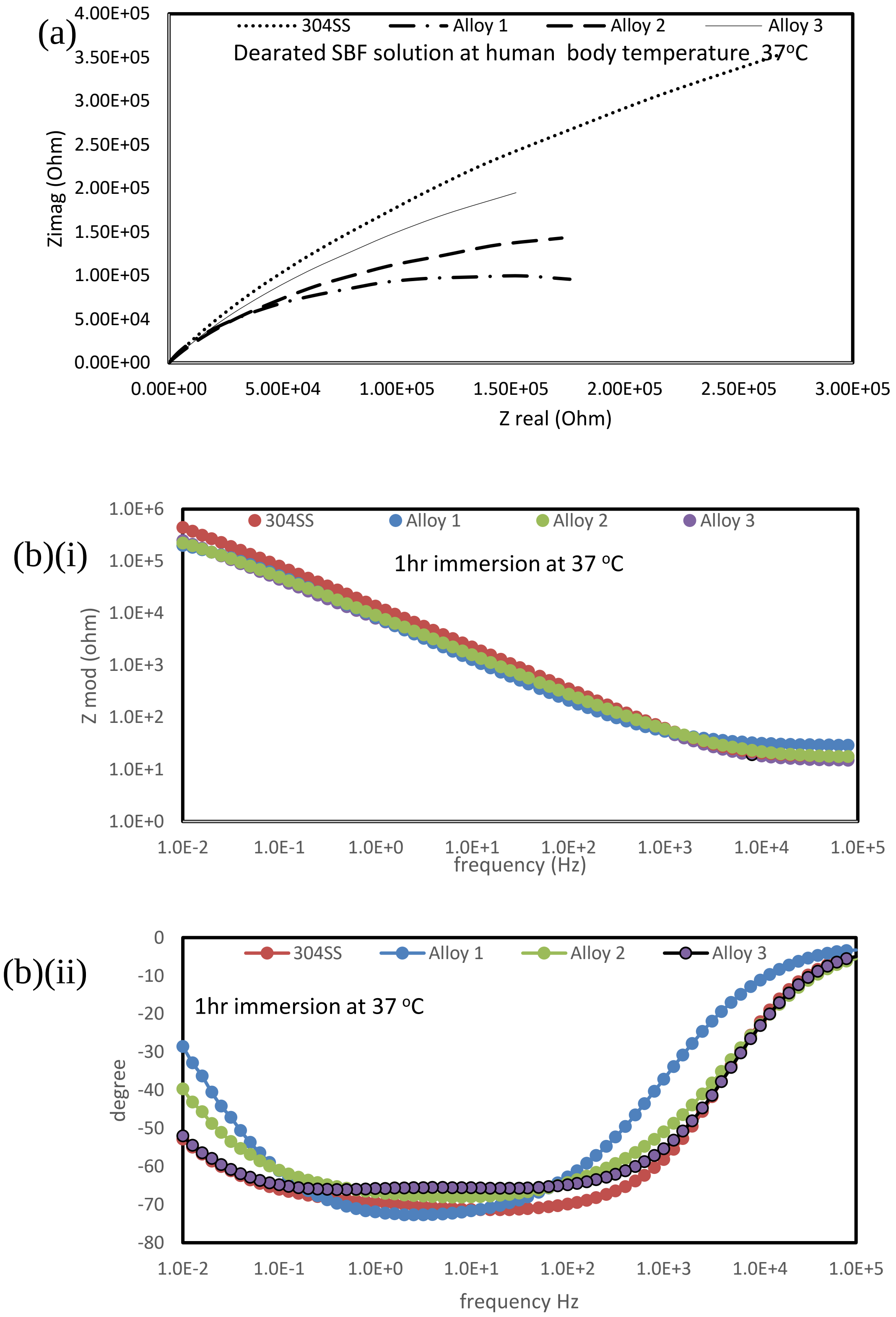

Fig.36. EIS (a) Nyquist and (b)(i) & (ii) Bode curves of DSS alloys and 304SS in SBF at human body temperature.

Table 11(a). Potentiodynamic polarization values in SBF solution at different conditions

Material	37^{o}C Human Body Temperature		20^{o}C Room Temperature					
	1 hr Immersion Time		1 hr Immersion Time		12 hr Immersion Time		24 hr Immersion Time	
	Polarization resistance, Rp (Ω)	Solution resistance, Ru(Ω)	Polarization resistance, Rp (Ω)	Solution resistance, Ru(Ω)	Polarization resistance, Rp (Ω)	Solution resistance, Ru(Ω)	Polarization resistance, Rp (Ω)	Solution resistance, Ru(Ω)
304SS	1.10E+06	16.56	7.16E+05	35.34	3.99E+05	51.73	1.66E+12	43.19
Alloy 1	2.73E+05	15.12	8.62E+04	32.18	1.36E+05	50.39	2.76E+05	45.28
Alloy 2	4.33E+05	17.04	1.05E+05	32.67	1.88E+06	50.27	1.71E+12	39.87
Alloy 3	9.13E+05	15.75	4.35E+05	33.06	3.88E+05	49.29	6.35E+12	46.1

Table 11(b). EIS analysis data obtained from fit with equivalent circuit (CPE) model

Material	37^{o}C Human Body Temperature		20^{o}C Room Temperature					
	1 hr Immersion Time		1 hr Immersion Time		12 hr Immersion Time		24 hr Immersion Time	
	E_{pit} (mV)	i_{pass} (A/cm2)	E_{pit} (mV)	i_{pass} (A/cm2)	E_{pit} (mV)	i_{pass} (A/cm2)	E_{pit} (mV)	i_{pass} (A/cm2)
304SS	226	1.144 E-6	357	6.66E-07	239	1.09E-06	384	1.20E-06
Alloy 1	198	1.140 E-6	167	5.41E-06	135	8.39E-06	210	4.32E-06
Alloy 2	229	1.602 E-6	331	2.58E-06	243	4.48E-06	304	1.87E-06
Alloy 3	225	1.139 E-6	324	2.57E-06	142	1.76E-06	385	1.18E-06

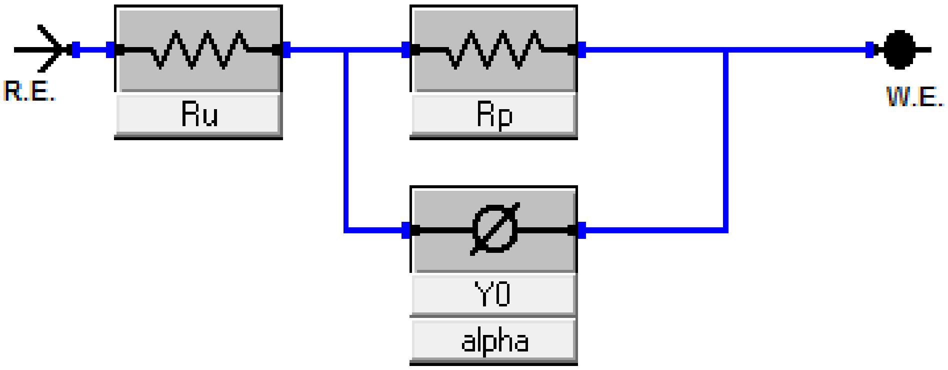

Fig.37. Equivalent circuit tested to the EIS experiment data in SBF solution

5.4.2. Electrochemical properties analysis at 20°C room temperature

Potentiodynamic polarization in SBF solution after 1 hr immersion under, OCP

The Fig.38 represents the results of potentiodynamic polarization after 1hr immersion under OCP at 20°C room temperature. The room temperature was measured prior to the test and the results showed that the E_{corr} was similar for both samples, however, E_{pit} was similar for 304SS and alloy 2, alloy 3 except for alloy 1 which depict less E_{pit} value. The passive current density i_{pass} was less for 304SS which indicate good corrosion properties and alloy 2 and 3 showed similar i_{pass} values, however, a higher value of i_{pass} was recorded for alloy 1. At 20°C room temperature alloy 1 showed poor corrosion properties due to lack of Cu content and higher amount of Mn in its composition [**6,13,56,68-70**]. 304SS showed less value of i_{pass} than other DSS alloys due to a higher amount of Nickel which increases the corrosion properties [**78**].

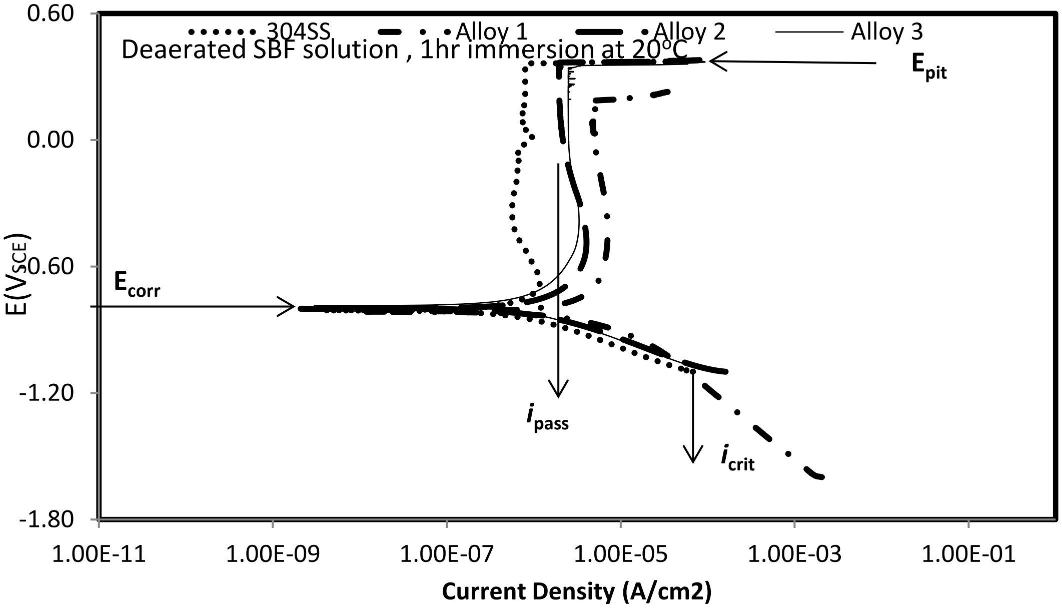

Fig.38. Potentiodynamic polarization curves of DSS alloys and 304SS after 1hour immersion in SBF at 20^{o}C room temperature.

EIS analysis in SBF solution after 1 hr immersion under, OCP

The Nyquist plot and Bode plot for EIS analysis after 1hr immersion under OCP at 20^{o}C room temperature are presented in the Fig.39. The Nyquist plot in the Fig.39 (a) shows the impedance spectra of 304SS and DSS alloys after 1hr immersion where 304SS has larger semicircle followed in a series of alloy 3> alloy 2 > alloy1. The spectra semicircle is directly proportional to polarization resistance thus good corrosion properties. Therefore, the polarization resistance i.e good corrosion resistance increases as 304SS > alloy 3 > alloy 2 > alloy 1.

In addition, an equivalent circuit was established to simulate the experimental condition to obtained impedance measurements values. Due to non-ideal capacitive behavior, a constant phase element CPE was established as shown in the previous Fig.37 of the equivalent circuit. The constant phase elements CPE impedance was presented as shown below as the variable explained in the previous similar equation.

$$Z_{CPE} = 1/Y_o(j\omega)^n \qquad \textbf{[79]}$$

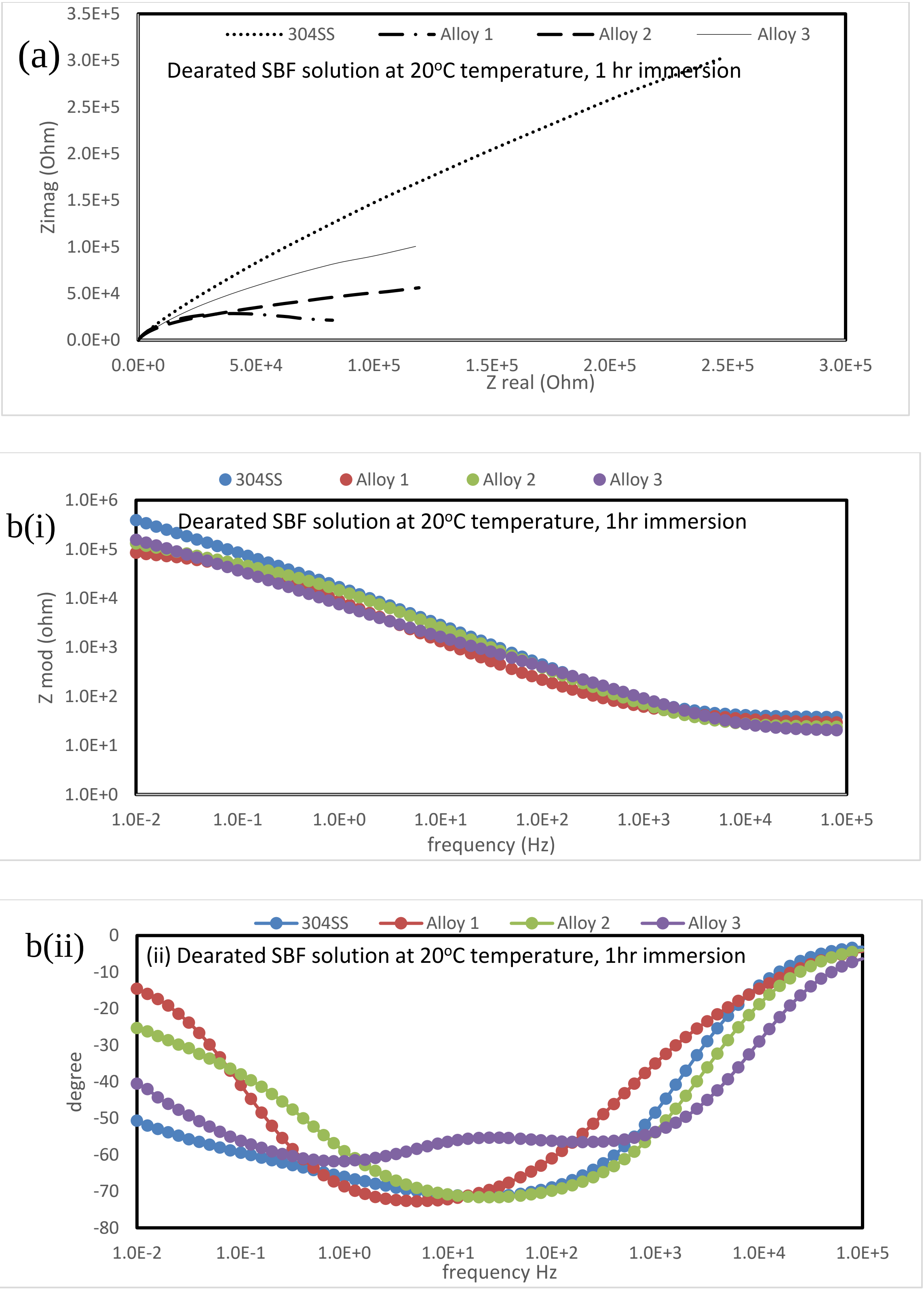

Fig.39. EIS (a) Nyquist and (b)(i) & (ii) Bode curves of DSS alloys and 304SS in SBF after 1hr immersion at 20°C room temperature.

Similar behavior is observed in the bode plots Fig.39 (b) (i) and (ii) whereby the impedance response showed resistive and capacitive behavior at a higher frequency and middle-low frequency respectively. The impedance values at low frequency were observed to be in the ascending order of alloy 1 < alloy 2 < alloy 3 < 304SS. Similarly, phase angle was observed in the same decreasing order of alloy 1 > alloy 2 > alloy 3 > 304SS. 304SS has a higher amount of Ni **[78]** contents as well as alloy 3 has higher Cu which enhancing the corrosion properties **[68-70].** As previously mentioned that, Mn has a detrimental effect on the corrosion properties of stainless steel, that is why the Mn content increase in Alloy 2and 3 can be an attribute to their low polarization resistance values.

Potentiodynamic polarization in SBF solution after 12 hr immersion under, OCP

In the Fig.40 the potentiodynamic polarization results were recorded after 12 hr immersion under OCP at 20^{o}C room temperature. The results showed that after 12 hr immersion the E_{corr} was almost similar for all alloys, however, E_{pit} values were not similar. 304SS and alloy 2 showed similar E_{pit} values and less E_{pit} values were observed for alloy 3 and the lowest E_{pit} value for alloy 1. The i_{pass} values were increasing in the series of 304SS < alloy3 < alloy 2 < alloy 1. Noted that the less i_{pass} value the better the corrosion properties. An increase in of i_{pass} value is attributed to Ni **[78]** for 304SS and Cu- content for DSS alloys **[68-70].** However, E_{pit} for alloy 2 was observed to have a higher value than that of alloy 3. The reason is attributed to the double effect of Cu which is reported to have both negative and positive effect on the corrosion properties [**26-28**]

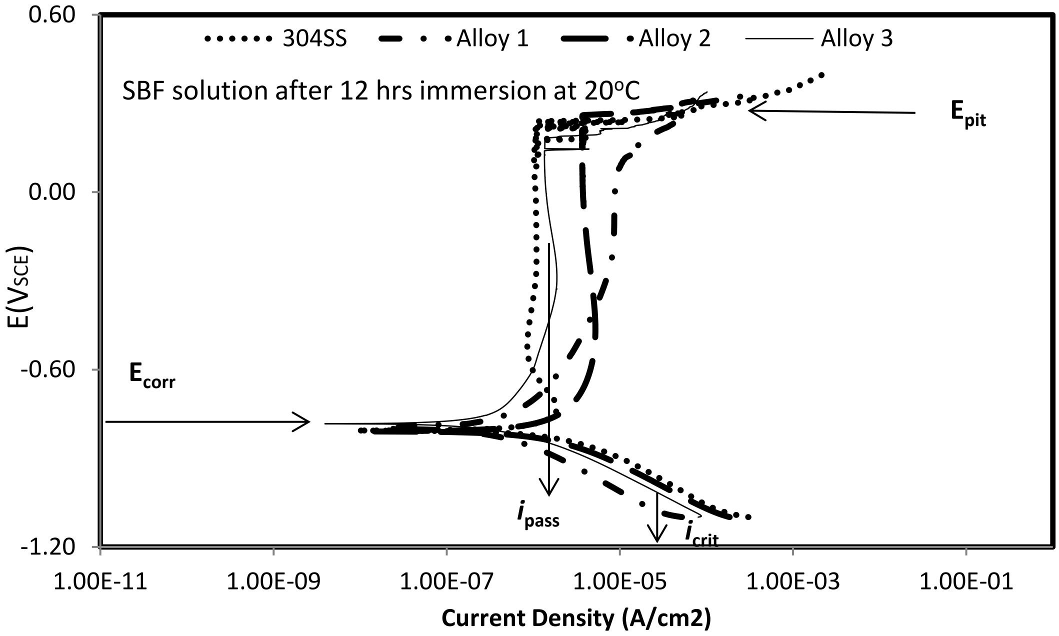

Fig.40. Potentiodynamic polarization curves of DSS alloys and 304SS after 12hr immersion in SBF at 20 °C room temperature.

EIS analysis in SBF solution after 12 hr immersion under, OCP

Fig.41. represent the EIS impedance spectra obtained after 12hr immersion under OCP at 20°C room temperature. In the Fig. 41(a). Nyquist spectra of 304SS and DSS alloys are observed after 12hr immersion at room temperature. The semicircle spectra represent the polarization resistance i.e corrosion resistance.

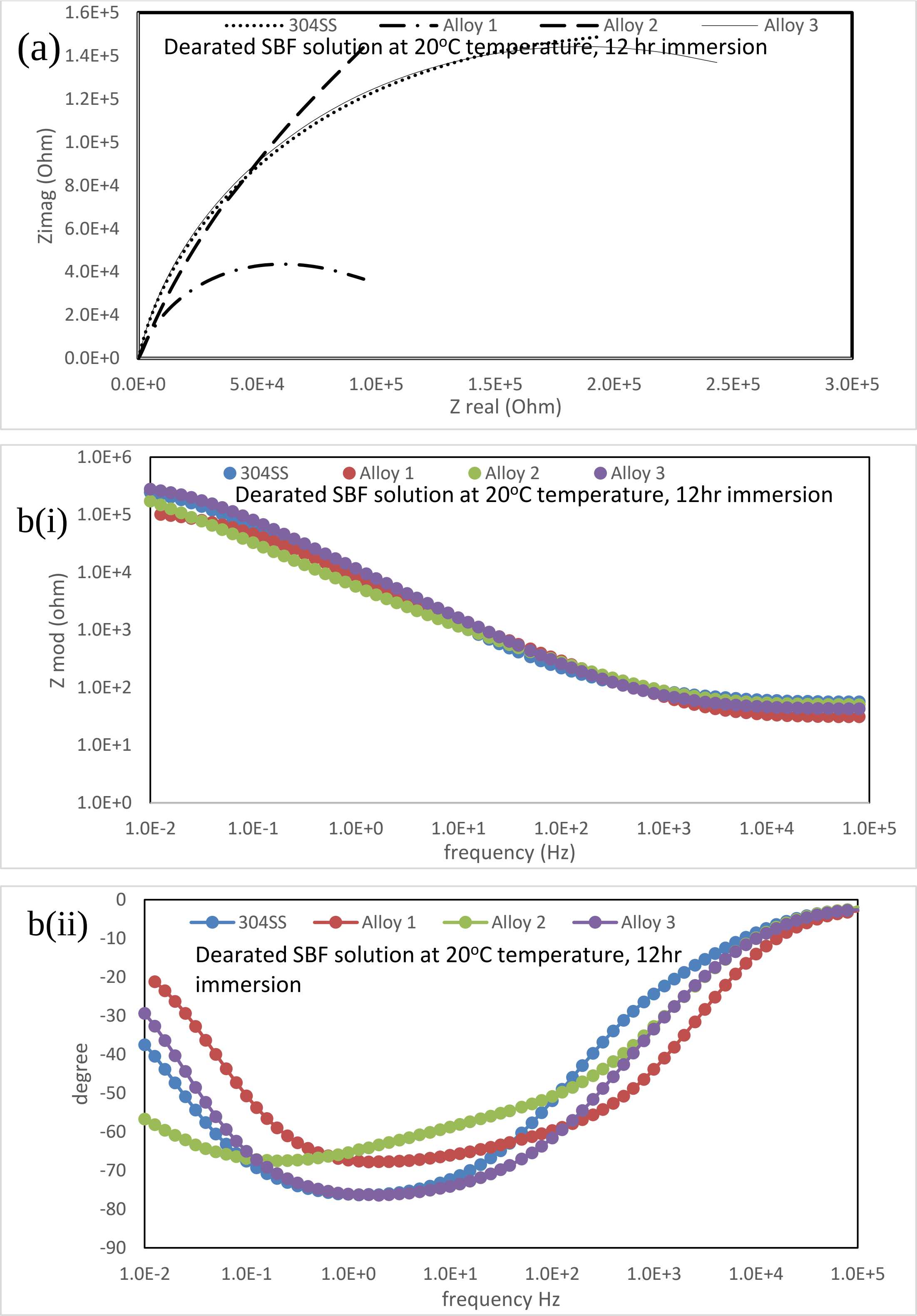

Fig.41. EIS (a) Nyquist and (b)(i) & (ii) Bode curves of DSS alloys and 304SS in SBF after 12hr immersion at 20 °C room temperature.

The higher semicircle which refers to higher polarization resistance was observed for alloy 2 followed by 304SS and alloy 3 and later alloy 1. Bode curves in the Fig.42 (b)(i&ii). Similar impedance response was observed whereby resistive behavior was observed in the higher frequency as well as a capacitive response at middle and low frequencies. Bode plots in the Fig.42 (b)(i) showed higher impedance values of 304SS and alloy 3 at low frequencies, however, the alloy 2 trend suggests increasing impedance values as the frequencies decrease. Cu effect on stainless steel is yet to be clarified whether is beneficial or harmful to their corrosion properties **[68-70].** However, after 12hr immersion in SBF solution alloy 2 with Cu-1% seems to have higher polarization resistance than alloy 3 and 304SS, despite the Ni content in 304SS. Similar constant phase element CPE in Fig.37 was established to simulate the experimental results to obtain impedance values.

Potentiodynamic polarization in SBF solution after 24 hr immersion under, OCP

Fig.42. shows the results of polarization resistance after 24hr immersion under OCP at 20^{o}C room temperature. The results show that the corrosion potential E_{corr} for all 304SS and DSS alloys to be similar except slight increase was observed for alloy 2. The pitting potential E_{pit} was almost similar for 304SS and alloy 3 under 24hr immersion. E_{pit} was observed to be less for alloy 2 and the lowest for alloy 1. The passive current density for 304SS and alloy 3 was similar and a decrease was observed for alloy 2 and more decrease for alloy 1. After 24hr immersion, the 304SS with a higher amount of nickel which is excellent in enhancing corrosion properties **[78]** and alloy 3 with a higher amount of Cu showed higher E_{pit} and i_{pass} values compared to alloy 1 and 2. Copper has a tendency of suppression anodic dissolution of stainless steel **[68-70],** therefore, it can be said after 24hr immersion Cu affect the alloys positively, and hence, higher corrosion resistance was observed

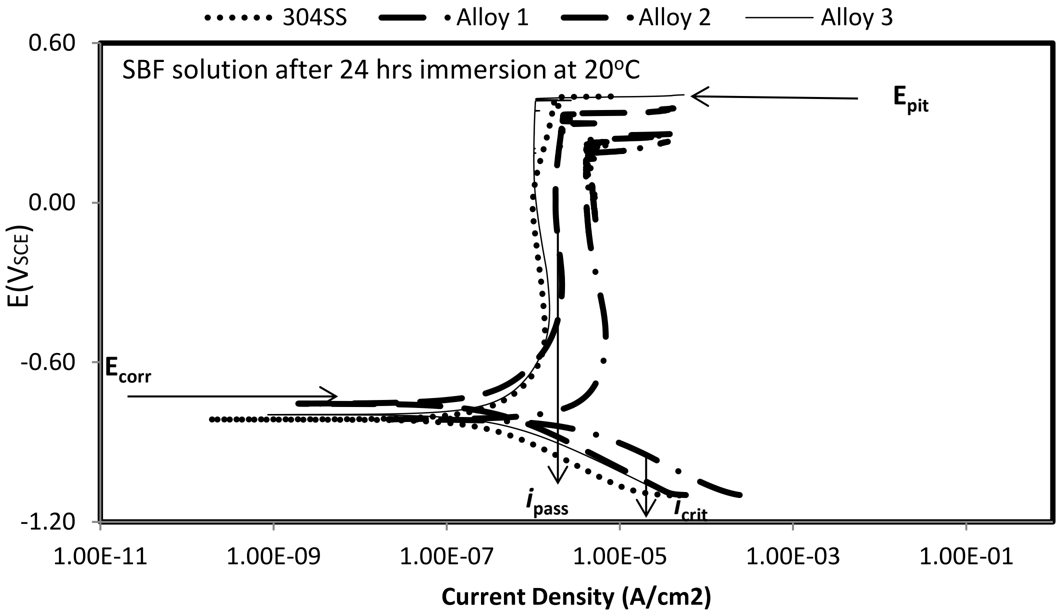

Fig.42. Potentiodynamic polarization curves of DSS alloys and 304SS after 24-hour immersion in SBF at 20^{o}C room temperature.

EIS analysis in SBF solution after 24 hr immersion under, OCP

The EIS results were recorded after 24hr immersion in Fig.42 (a &b) under OCP at 20^{o}C room temperature. The results show a Nyquist impedance curve in Fig.42 (a) in which alloy 3 recorded with big semicircle impedance spectra which refers to higher polarization resistance than alloy 2 and 304SS and followed by small semicircle for alloy 1. The higher polarization resistance for alloy 3 can be attributed to a large amount of Cu content and minimum amount of Mn than other alloys. Noted that in the previous discussion the detrimental effect of Mn and beneficial effect of Cu on the corrosion properties of stainless steel. However, after 24hr immersion, the alloy 3 with Cu-2% content seems to have a better polarization resistance. Copper tends to suppress the anodic dissolution of stainless steel, therefore, as the immersion time increases the better corrosion resistance was observed in the alloy 3. In the Fig. Fig.42 (b)(i&ii). Bode plots show the impedance response versus frequency. The resistive behavior at a higher frequency and capacitive nature at lower frequencies were depicted. Similarly, alloy 3 showed higher impedance values and low phase angle at low frequencies than other alloys. To obtain impedance values under simulated experimental condition a CPE was established like that in Fig.37.

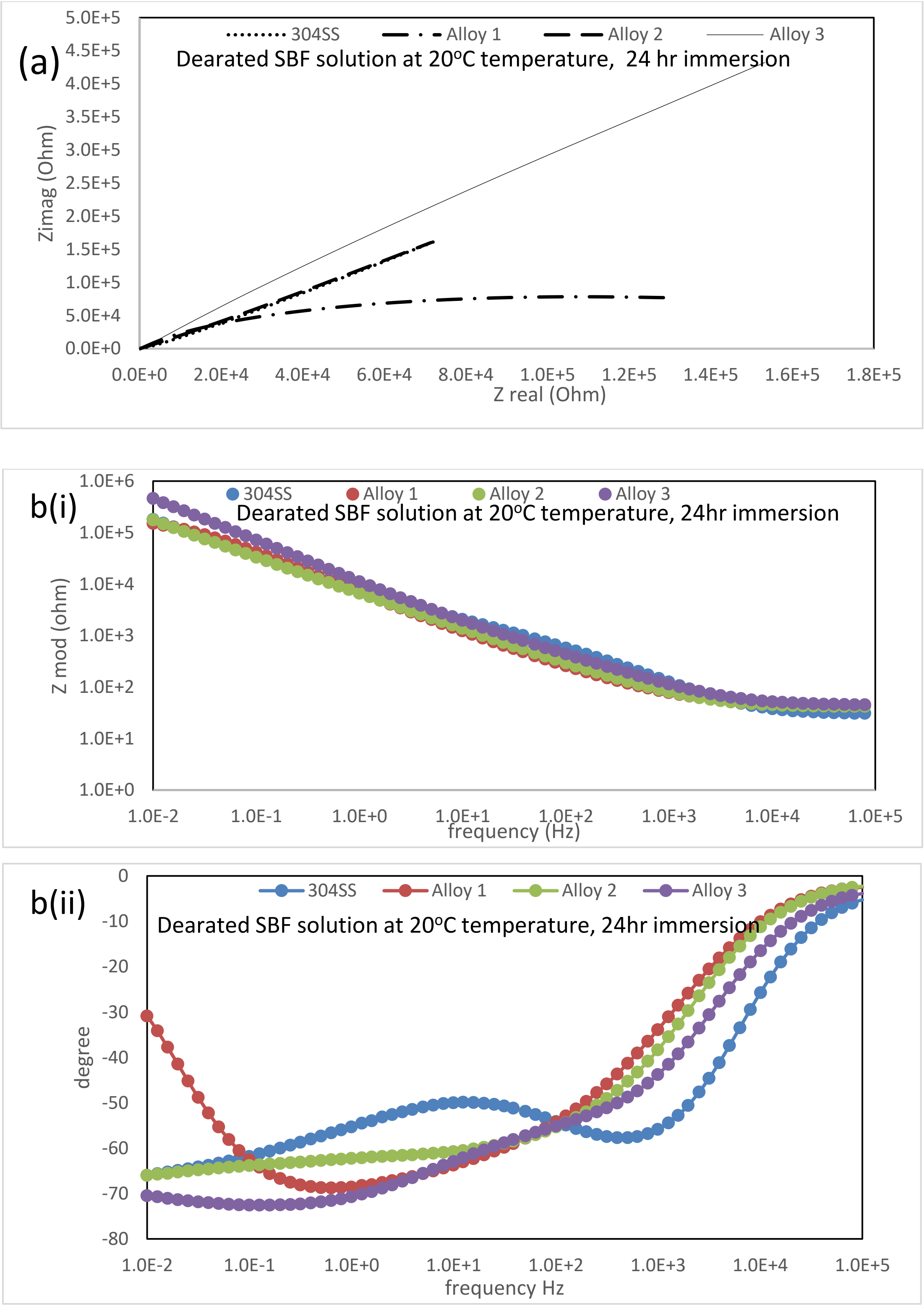

Fig.43. EIS (a) Nyquist and (b)(i) & (ii) Bode curves of DSS alloys and 304SS in SBF after 24hr immersion at 20 ° C room temperature.

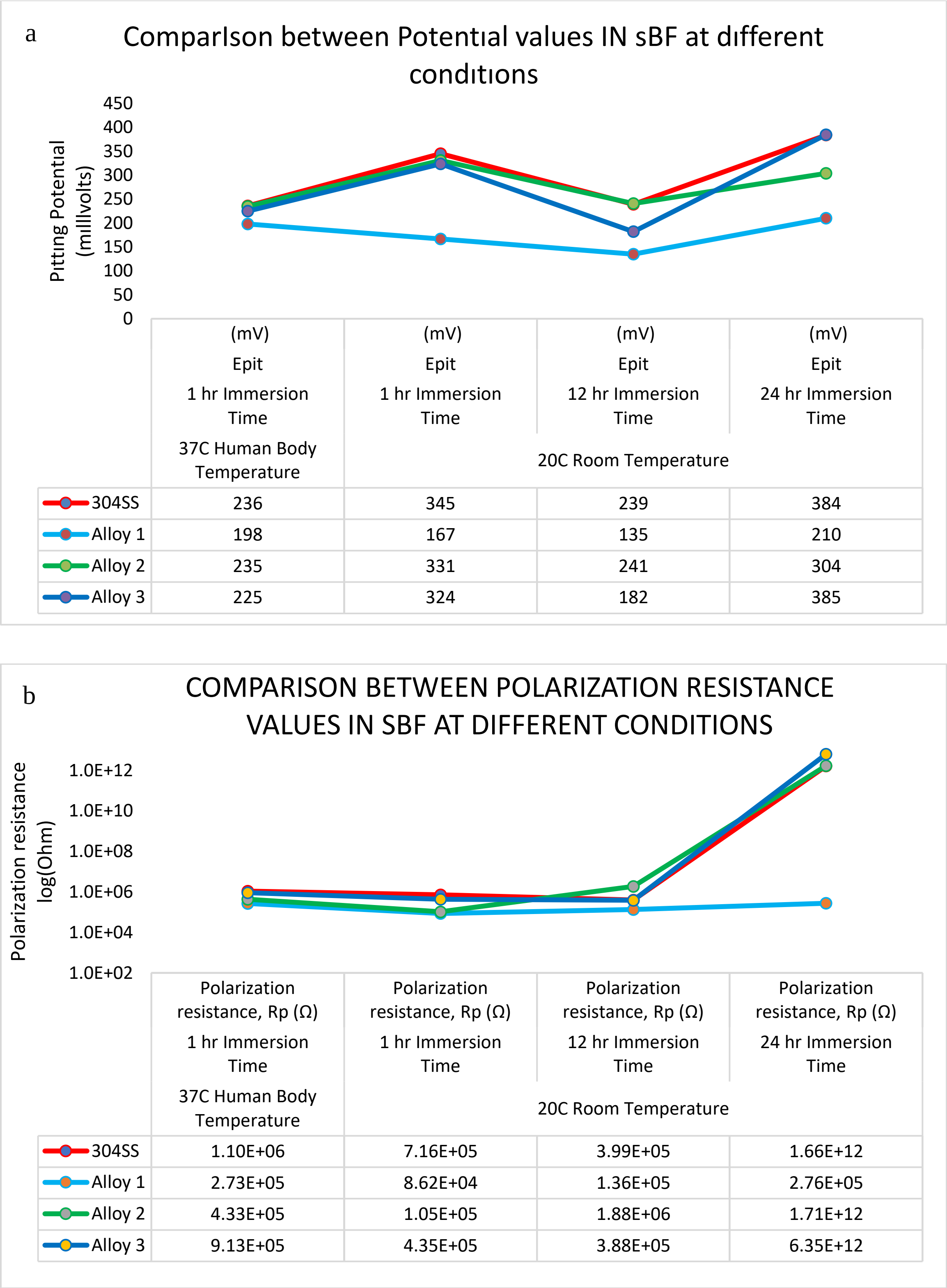

	(mV) Epit 1 hr Immersion Time 37C Human Body Temperature	(mV) Epit 1 hr Immersion Time 20C Room Temperature	(mV) Epit 12 hr Immersion Time 20C Room Temperature	(mV) Epit 24 hr Immersion Time 20C Room Temperature
304SS	236	345	239	384
Alloy 1	198	167	135	210
Alloy 2	235	331	241	304
Alloy 3	225	324	182	385

	Polarization resistance, Rp (Ω) 1 hr Immersion Time 37C Human Body Temperature	Polarization resistance, Rp (Ω) 1 hr Immersion Time 20C Room Temperature	Polarization resistance, Rp (Ω) 12 hr Immersion Time 20C Room Temperature	Polarization resistance, Rp (Ω) 24 hr Immersion Time 20C Room Temperature
304SS	1.10E+06	7.16E+05	3.99E+05	1.66E+12
Alloy 1	2.73E+05	8.62E+04	1.36E+05	2.76E+05
Alloy 2	4.33E+05	1.05E+05	1.88E+06	1.71E+12
Alloy 3	9.13E+05	4.35E+05	3.88E+05	6.35E+12

Fig.44. Comparison between (a) pitting potential values and (b) polarization resistance values of DSS alloys and 304SS in SBF solution at different conditions

5.4.3. Comparison between pitting potential values and polarization resistance values of DSS alloys and 304SS in SBF solution at different conditions

A comparison study was carried out between pitting potential values and polarization resistance values of DSS alloys and 304SS in SBF solution at different conditions. The results were shown in the Fig.44 (a & b).as pitting potential values and polarization resistance values comparison. In the Fig.44 (a) pitting potential E_{pit} values can be correlated with the temperature and immersion time.

Fig. 44(a) shows the variation of E_{pit} values after 1hr immersion at 37°C human body temperature and 20°C room temperature. The E_{pit} values at human body temperature seem to be less than that of room temperature. Temperature has affected negatively the E_{pit} values of 304SS and DSS alloys. Slightly difference was noted in alloy 1, with no Cu-content, in which its E_{pit} values decreased rather than an increase noted in other alloys.

For temperature variations in EIS experiment in Fig.44 (b), there was no significant effect of temperature on the impedance values i.e polarization resistance, however, a slight decrease in polarization resistance was noted at 20°C room temperature.

At 20°C room temperature, to analyze the effect of different immersion time, 304SS and DSS alloys were immersed in SBF solution at 1hr, 12hr, and 24hr. In Fig.44. (a) E_{pit} values at different immersion time seem to have a sharp decrease between 1hr to 12hr immersion time for all DSS alloys and a 304SS and sharp increase of E_{pit} values between 12hr and 24hrs immersion time. Alloy 3 with 2% Cu seems to have higher E_{pit} value after 24hr immersion than alloy 2, similarly, alloy 2 with 1%Cu seems to have higher E_{pit} value than alloy 3 after 12 hr immersion.

In Fig.44 (b) polarization resistance in EIS at 20°C room temperature was observed to have slightly decreased between 1hr and 12hr immersion time for 304SS, alloy 1 and alloy 3, however, an increase in polarization resistance was observed for alloy 2 with 1%Cu. After 24hr immersion time polarization resistance increase drastically for 304SS, alloy 2 and alloy 3 except for alloy 1 which had a slight increase in polarization resistance.

5.5. Effect of agitated conditions (revolution per minutes, rpm) on Electrochemical properties of DSS alloys and 304SS

The industrial application includes exposure of material into a slurry and in motion fluids which subject the material under not only corrosion hazards influenced by the chemical nature but also physical (effect) nature of fluids transported on it. In oil and gas industries during drilling solvents are injected into the reservoir at a higher pressure and speed to facilitate oil flow which in turn may influence in the corrosion of the pipes used in the wellbore **[80].** In the transportation of fluids such as crude, chemicals, benzene as well as inside fluids industrial facilities increase the chance of flow assisted corrosion. During fluid flow, a uniform corrosion or localized corrosion can be induced and be propagated this is sometimes considered to be erosion-corrosion i.e corrosion influence by flow velocity **[81]**.

Less work has been reported and researched on the effect rotation in chloride solution on the electrochemical properties of cast DSS alloys and 304SS. A commercial AISI 304SS has been used as comparison material to cast DSS alloys. In this work, a rotating fluid by electromagnetic stirrer has been used to simulate the influence of flow assisted corrosion in 0.2M NaCl solution. The electrochemical measurements such as Potentiodynamic polarization PDP and Electrochemical Impedance analysis have been used to study the effect of different rotation speed.

5.5.1. Influence of rotation speed (rpm) on the corrosion behavior of DSS alloys and 304SS during potentiodynamic polarization techniques

In the Fig.45 the results of potentiodynamic polarization obtained at different rotation speed and different concentration of Nevamine CP20 inhibitor. The rotation speeds were varied at three different speed such as 0, 500 and 1000 revolution per minutes. The experiments were performed in the deareted 0.2M NaCl solution. The results in Fig.45 and 31(a) showed that the decrease in pitting potential E_{pit} values at a different rotation speed from 0 to 1000 rpm without inhibitor. All DSS alloys and 304SS showed a similar trend of decrease in the E_{pit} values as the rpm speed increases.

The effect of rotation speed on the E_{pit} values of the alloys is observed to affect negatively the E_{pit} values which can be explained by the effect of moving solution. Stainless steel alloys have a tendency of forming a protective passive layer a higher potential. However, when rotation speed increases the protective passive film formed is weak and break up at less potential than at stagnant solution. Also, a dynamic fluid has higher shear stress on the surface of the alloys which in turn reduces the stability of passive film formed [**81,83,84**].

In the Fig.45 and 46(b) the corrosion potential E_{corr} results of DSS alloys and 304SS were recorded and plot in the graph. The corrosion potential E_{corr} was observed to have an increasing trend for all DSS alloys and 304SS in 0.2M NaCl when no inhibitor was used. The E_{corr} values seem to increase when the rotation speed increased from 0 to 1000 rpm for a solution without inhibitor.

The effect of rotation speed was observed for all material when rotation speed increased to 500 and 1000rpm at 20 ppm concentration. Effect of rotation speed on the E_{corr} values seems to be positive since there is increasing of E_{corr} values when rpm increases, hence, better corrosion resistance properties at higher potential values.

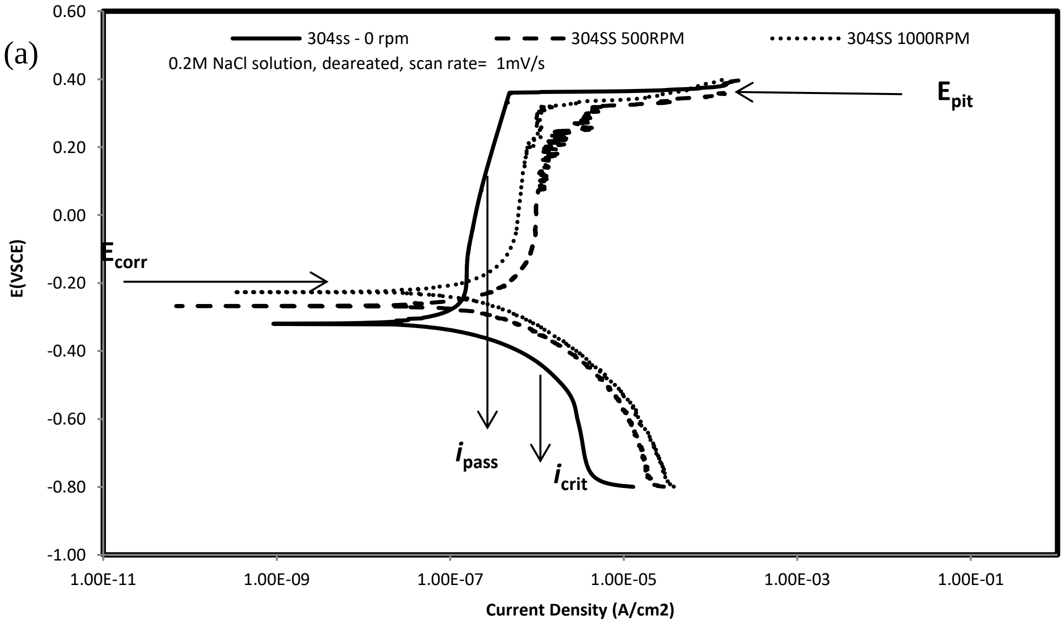

Fig.45 (a). Potentiodynamic polarization (PDP) curves of 304SS at different rotation speed (revolution per minutes, rpm)

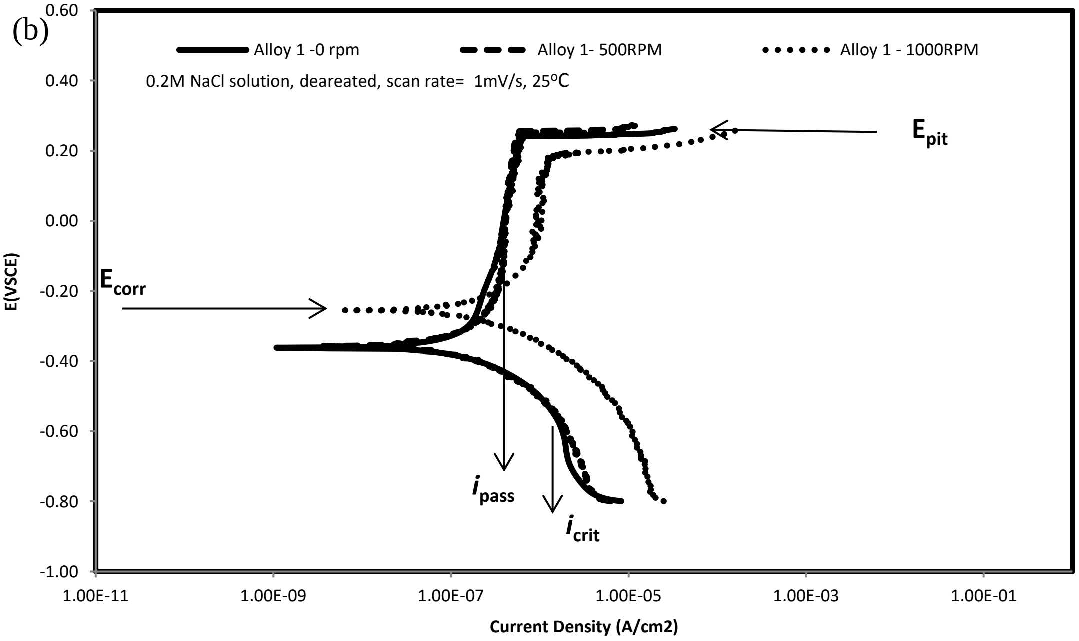

Fig.45(b). Potentiodynamic polarization (PDP) curves of Alloy1 at different rotation speed (revolution per minutes, rpm)

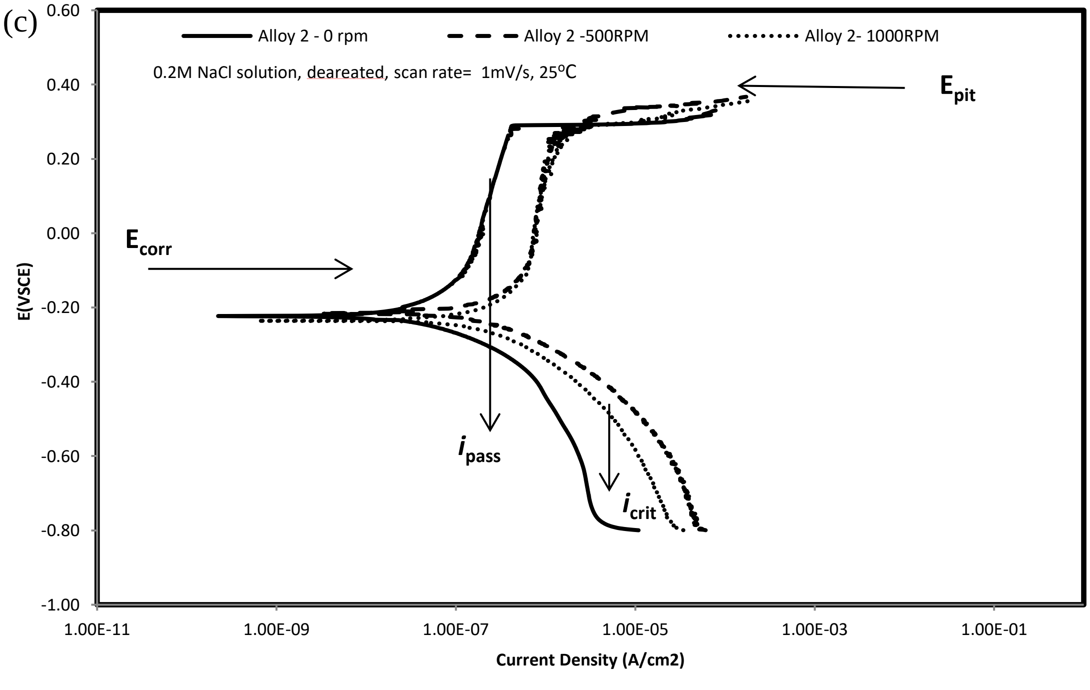

Fig.45(c). Potentiodynamic polarization (PDP) curves of Alloy 2 at different rotation speed (revolution per minutes, rpm)

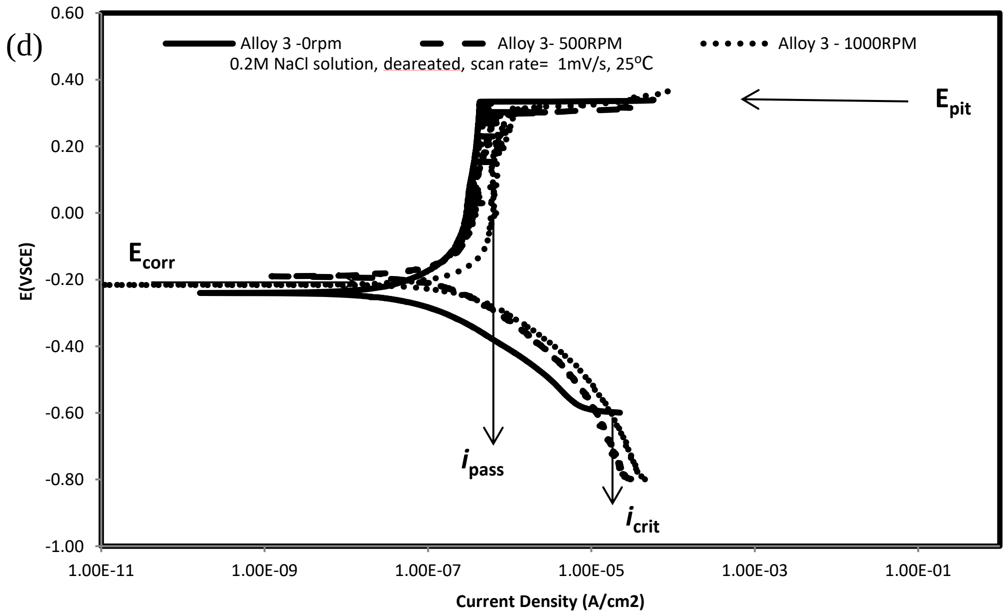

Fig.45. Potentiodynamic polarization (PDP) curves of Alloy 3 at different rotation speed (revolution per minutes, rpm)

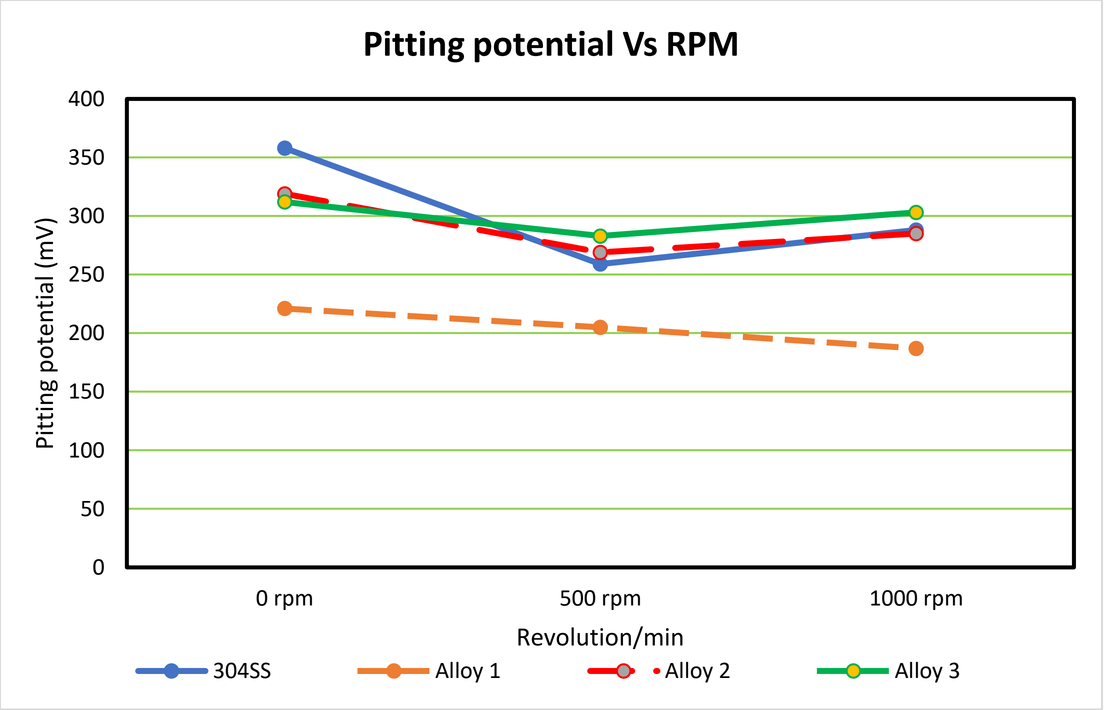

Fig.46. Variation of (a) pitting potential Epit and (b) corrosion potential Ecorr at different conditions.

5.5.2. Influence of rotation speed (rpm) on the corrosion behavior of DSS alloys and 304SS during EIS analysis

In the Fig.47 the EIS impedance Nyquist semi-circle spectra show the polarization resistance of the alloys at different rotation speed and different concentration of inhibitor. The Nyquist semi-circle curves are directly proportional to the polarization resistance i.e corrosion resistance. The bigger the semi-circle i.e large diameter the higher is the polarization resistance. From the Fig.47. Nyquist plots at different rotation speed without inhibitor seems to have bigger semi-circle at 0rpm for all DSS alloys except for 304SS and at higher rotation speed 500 and 1000rpm there was a decrease in the diameter of the curves. The EIS results show agreements with the previous results in Fig.45 and 46 on the effect of rotation speed which decreases the polarization resistance due to shear stress on the surface of alloys, hence, the weak protective passive film is formed [**81,83,84**].

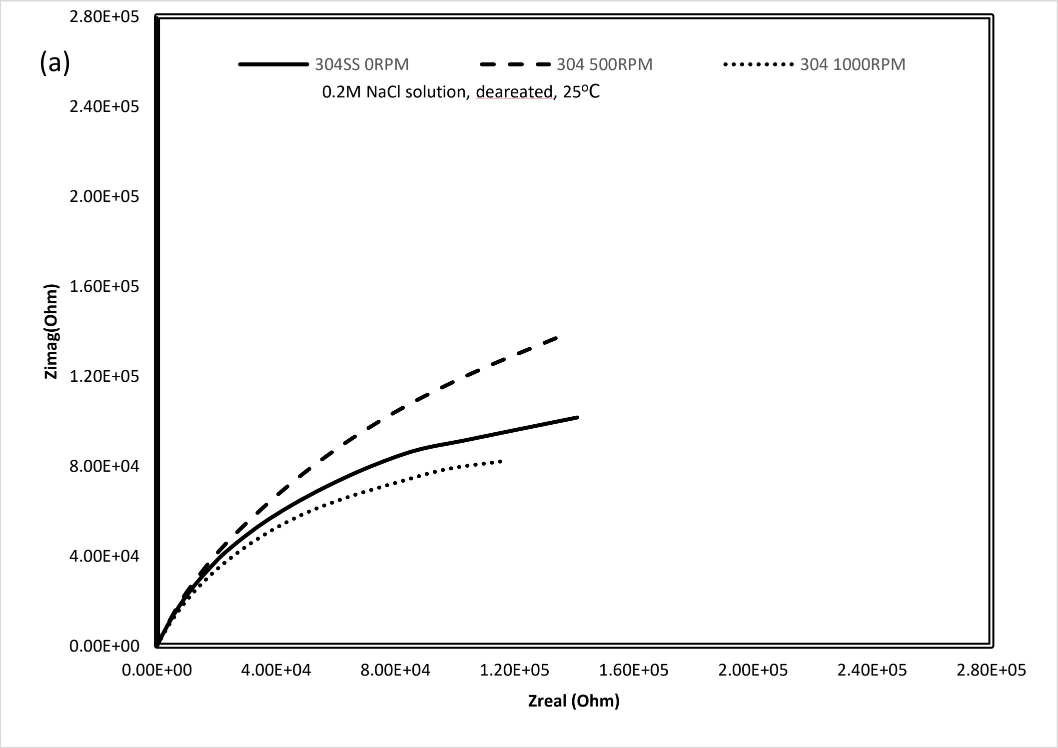

Fig.47(a). Electrochemical impedance (EIS) curves of 304SS at different rotation speed (revolution per minutes, rpm)

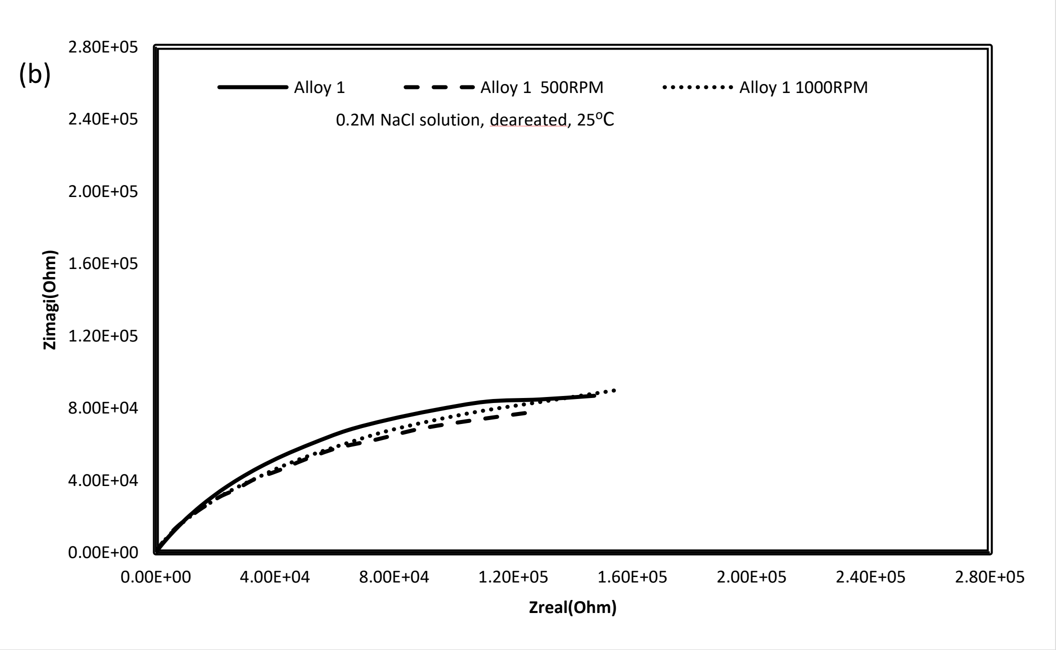

Fig.47(b). Electrochemical impedance (EIS) curves of Alloy1 at different rotation speed (revolution per minutes, rpm)

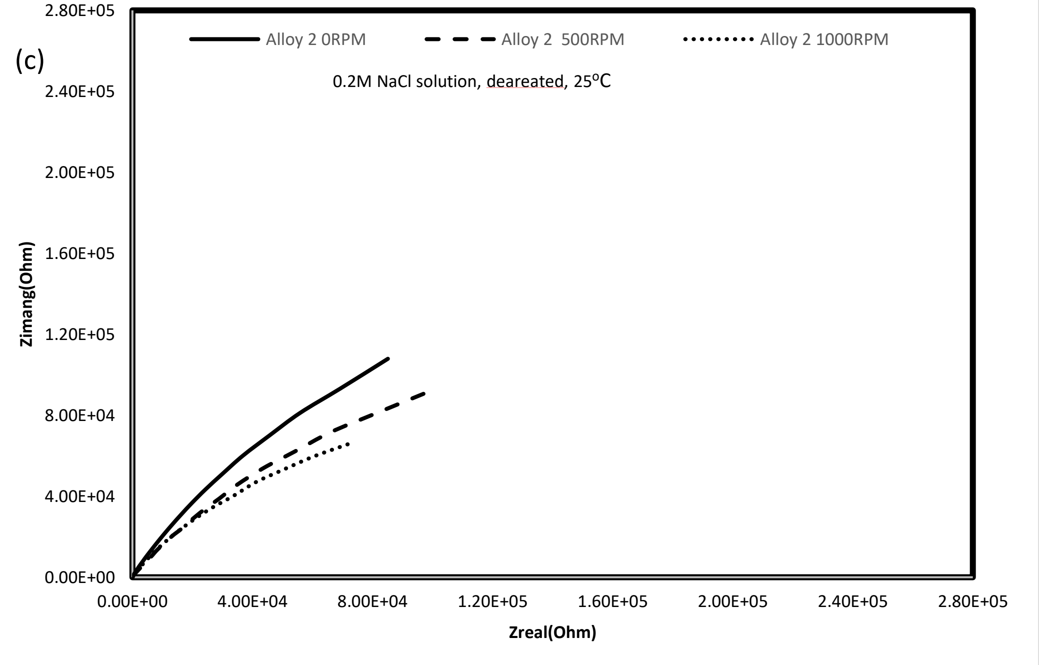

Fig.47(c). Electrochemical impedance (EIS) curves Alloy 2 at different rotation speed (revolution per minutes, rpm)

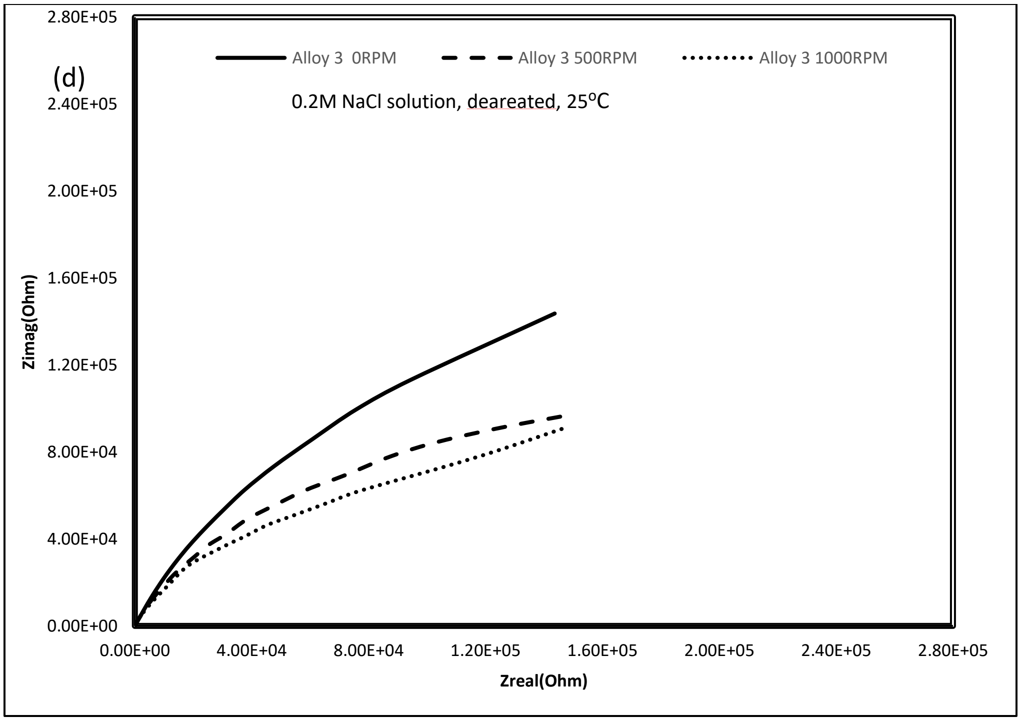

Fig.47(d). Electrochemical impedance (EIS) curves of Alloy 3 at different rotation speed (revolution per minutes, rpm)

CHAPTER 6

POWDER METALLURGY DUPLEX STAINLESS STEEL

6.1. Synthesis and phase evolution of nano-structured Duplex SSs

Recently more researchers have focused on the development of nano-structured duplex stainless steels alloys for different industrial and paramedical applications. In this chapter, we will focus on the synthesis of nano-structured duplex stainless steel from pure elemental powders by mechanical alloying. Element powders mixture of Fe, Cr, Mn, Mo, Si, Cu, Ni, and Nitrogen gas as atmosphere were mixed as shown in Table 9.

6.1.1. Mechanical alloying and powder characterization during milling process

The ball milling was carried out by Fritsch Pulverisette P-5 type of ball milling in Fig.24. The ball milling speed was 300rpm (revolution per minutes), milling time 20hr, ball to powder ration 12:1 and the composition of DSS alloys were presented in Table 9. Duplex stainless steel alloy compositions were designed and calculated by the help Schaeffler's diagram. The formula below can be a simple explanation of the alloys compositions. Powder particle size was reduced from micro to nano size particle after ball milled for 20hrs.

$$Fe_{(balance)}\text{-}Cr_{18}\text{-}Mn_{x}\text{-}Mo_{1}\text{-}Si_{1}\text{-}N_{0.22}\text{-}Cu_{y}\text{-}Ni_{z}\ (x = 6,\ y=0,\ 1\ ,\ z=3,\ 5)$$

Mechanical alloying was carried out for milling time of 20hr under nitrogen atmosphere which was purged after every 2hr of milling for 15minutes. The XRD of milled powder sample was conducted after 0, 2, 5, 10, 15 and 20hrs of milling to examine the phase evolution of designed alloys during the milling process and the changes occurred in the phases was discussed. In the Fig.48(a, b, c & d) which shows XRD pattern of all designed alloys and phase changes during milling. The sharp crystalline diffraction peaks started to be reduced and broadened continuously with milling time.

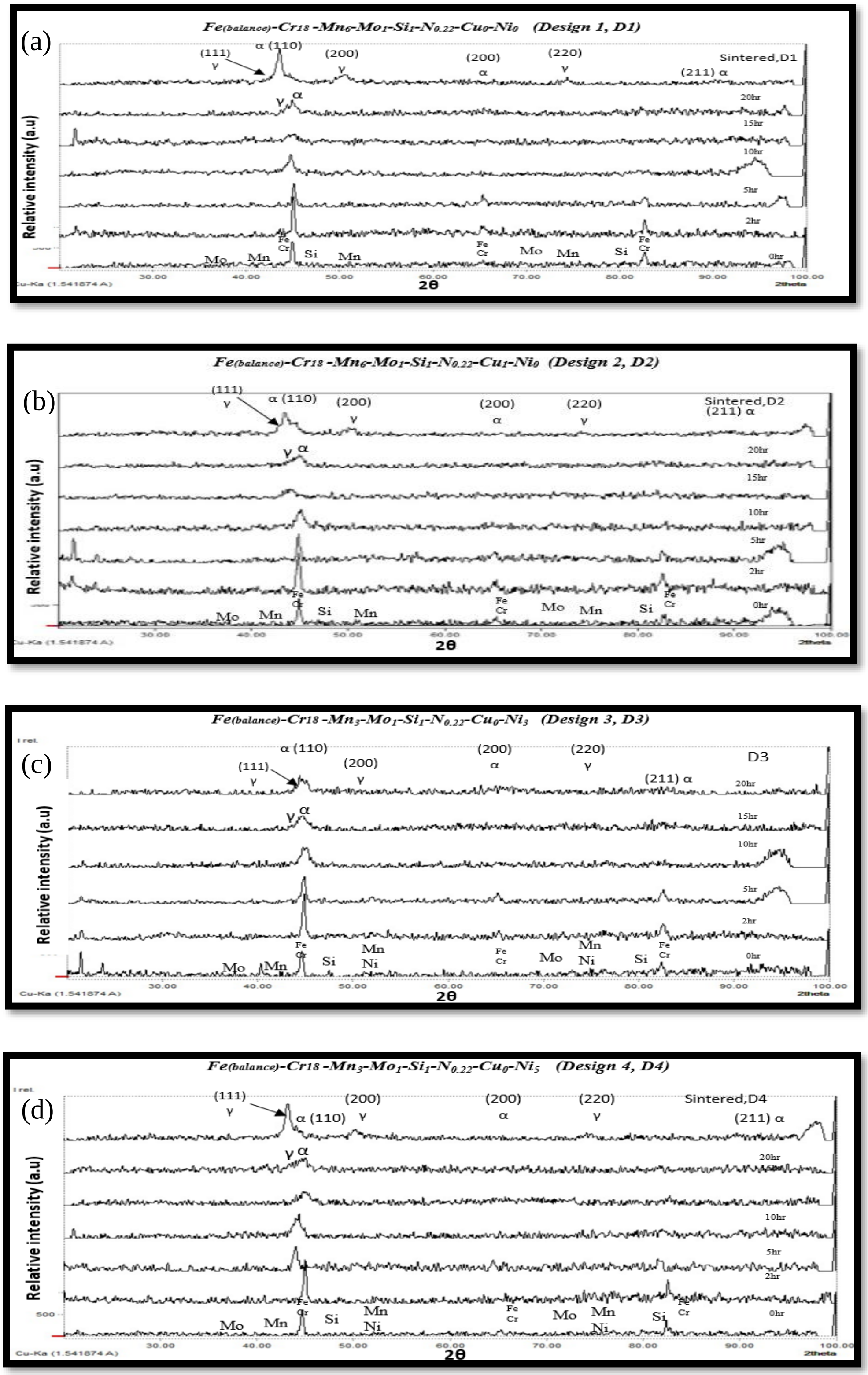

Fig.48. XRD patterns of ball milled (a)D1 (b)D2 (c) D3 and (d) D4 of Designed Duplex SS powder

The bottom XRD patterns in each figure show sharp peaks of Fe and Cr which later peak intensity was reduced as well as peak broadening occurred from 5hr of milling. This phenomenon occurs during milling process in the initial stages due to the dissolution of alloying elements into the Fe lattice, an increase of lattice strains due to continuously increase of structural defects as well as grain size reduction during milling **[23].** This phenomenon is visible from the initial stage until 10hr of milling where the duplex stainless-steel powder exhibit ferrite phase structure and later an amorphous structure is observed after 15hrs of milling. After 20hrs of milling phase transformation started to occur from ferrite phase peaks to an emergency of austenite phase peaks as shown in the XRD pattern in Fig.48(a, b, c & d). Crystallinity changes as the particle size diminished into nano-size as the time of milling increases.

6.1.2. Lattice parameter and crystalline size calculation

The lattice parameter of ball milled powder after 0, 2, 5 and 10hr were calculated by using a common equation shown $a = d*\surd h + k + l$. The value of d- spacing were calculated from the highest Braggs peak angle of (110) or (111) due to phase transformation occurs as the milling time increase. After 10hr of milling in Fig.49 (a) we can observe an increase in lattice parameter which signifies α to γ phase transformation during milling. In the initial stages of milling between 0 and 5hrs, the dominant phase was ferrite while as milling time increases there was peak displacement from (110) to (111) toward left. The displacement shows the emergence of austenite as milling time increase. From lattice parameter calculations, the values of lattice parameter increase from $2.86A^o$ of BCC iron to $3.51A^o$ of FCC iron.

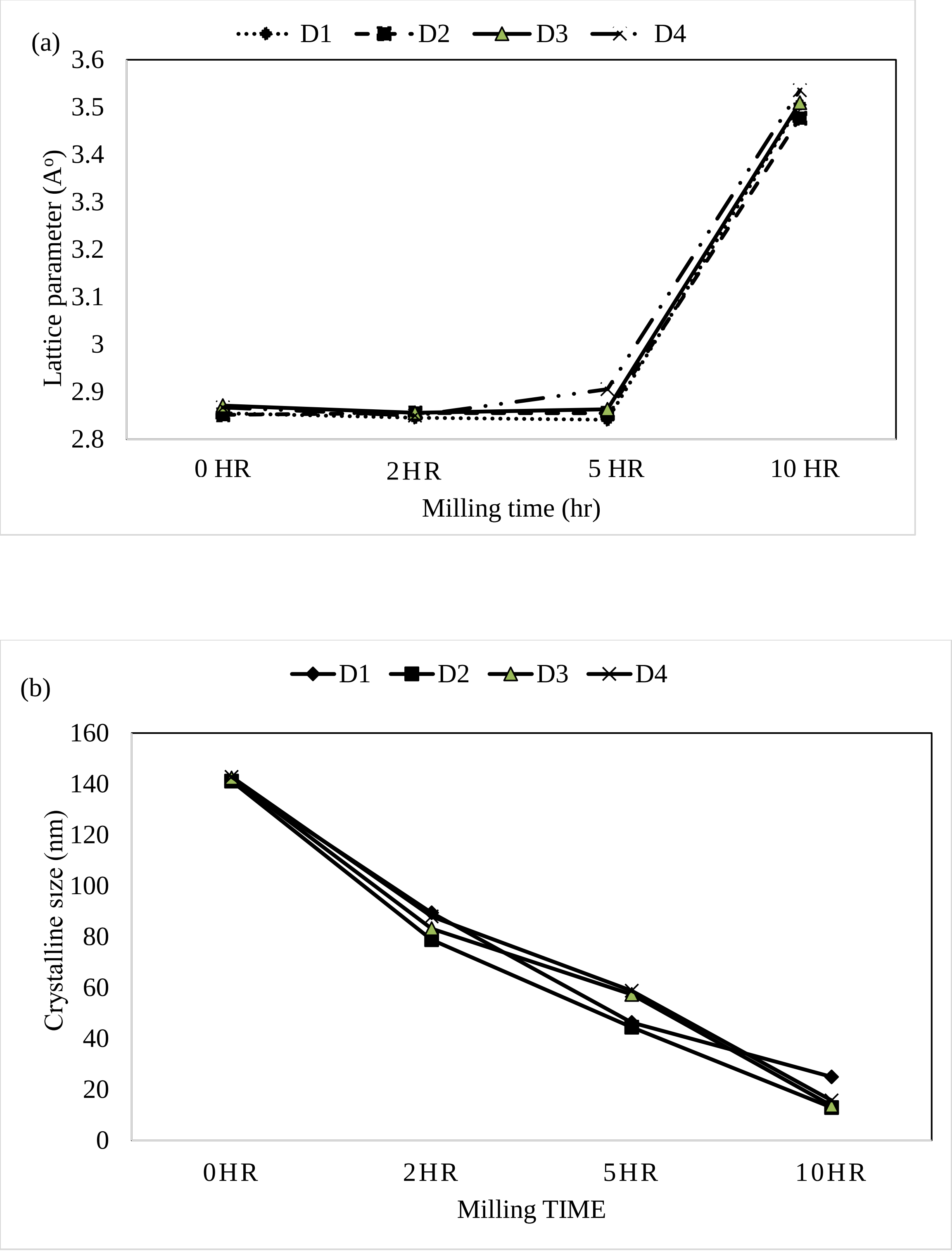

Fig.49. Variation of (a) lattice parameter and (b) Crystalline size with milling time during ball milling of DSS alloys.

Crystalline size of ball milled powder was calculated from the average of highest diffraction peaks using Scherrer equation ($D = 0.94\lambda / \beta\cos\theta$) where β is a full-width half maxima (FWHM), D is the crystallite size, λ is the wavelength of the X-ray used. The results in Fig.49(b) showed that the crystalline size decreases as the time for milling increases. After 10hr of ball milling, crystalline size attained saturation when peak broadening becomes dominant. The crystalline size becomes less than 15nm when milling time reached 10hr. Shashanka e.t al reported that when grain size of nanostructure stainless steel reached below 14nm the austenite phase becomes more stable and intense phase transformation can be expected **[19-21]**

6.1.3. Morphological analysis of ball milled powder

Scanning electron microscopy (SEM) was used to analyze the microstructure of milled powder taken after different time interval 0, 2, 5, 10, 15 and 20hr during ball of milling. The SEM micrographs of milled powder of D1 ($Fe\text{-}Cr_{18}\text{-}Mn_6\text{-}Mo_1\text{-}Si_1\text{-}N_{0.22}\text{-}Cu_0\text{-}Ni_0$), D2 ($Fe\text{-}Cr_{18}\text{-}Mn_6\text{-}Mo_1\text{-}Si_1\text{-}N_{0.22}\text{-}Cu_1\text{-}Ni_0$), D3 ($Fe\text{-}Cr_{18}\text{-}Mn_3\text{-}Mo_1\text{-}Si_1\text{-}N_{0.22}\text{-}Cu_0\text{-}Ni_3$) and D4 ($Fe\text{-}Cr_{18}\text{-}Mn_3\text{-}Mo_1\text{-}Si_1\text{-}N_{0.22}\text{-}Cu_0\text{-}Ni_5$) were represented in the Fig.50(a-f), Fig.51(a-f), Fig.52(a-f), and Fig.53(a-f) respectively. Before ball milling of alloys powder made from mix different elemental powder, their particle size was small, and their shapes were irregular. During the milling process, particles undergo cold welding and fracturing. After 2hr of milling, the particles were observed to agglomerate and became flat in shape. This behavior is associated with Fe ductility properties. As milling proceeds after 5hr, the flattened shape can be seen to cold-weld and join to form lamella shapes. After 10hr of milling, the flattened shape was fractured, and agglomeration can be seen in the SEM micrographs of all alloys after10hr of milling and the size of powder started to decrease in size. After 15hr of milling, powder gets work hardened and refine into small particle as well as the elemental powder in the alloy composition enters the Fe lattice. The particle reduction in size can be observed as it reaches nanoparticle size after 20hr. At this stage, the where the powder particle attained a nano-size more size reduction becomes difficult and some agglomerated powder particle of nano-size were present. The elemental distribution becomes homogenous when powder become nano-size.

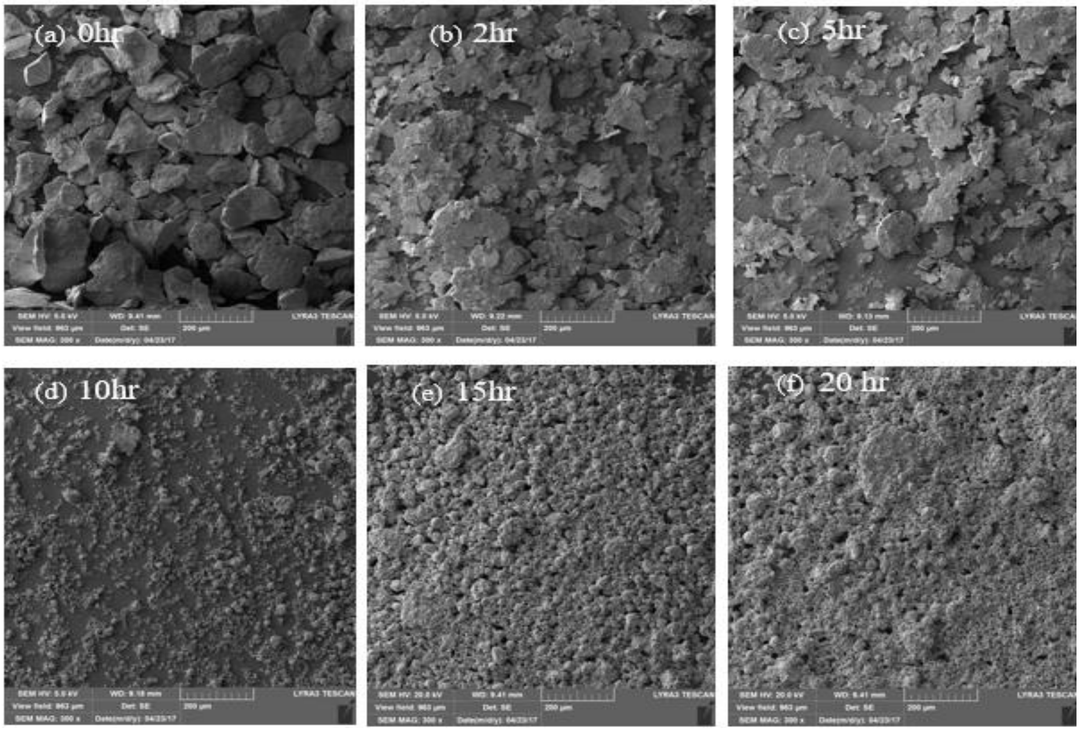

Fig.50. SEM image of ball milled powder D1 after (a)0hr (b) 2hr (c)5hr (d)10hr (e)15hr and (f)20hr of milling

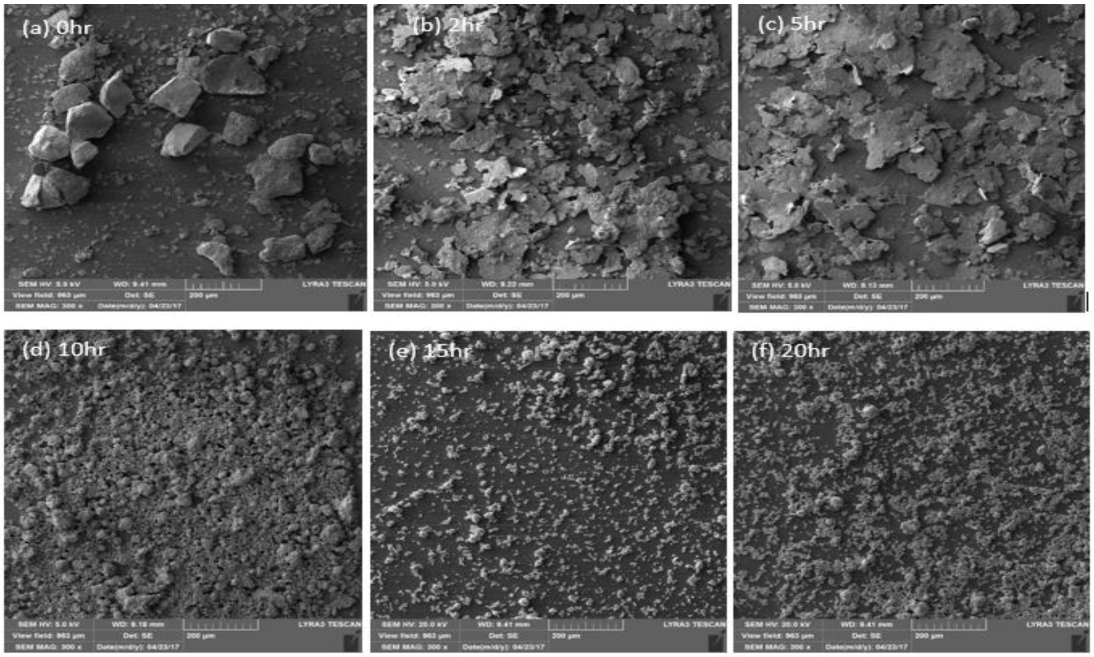

Fig.51. SEM image of ball milled powder D2 after (a)0hr (b) 2hr (c)5hr (d)10hr (e)15hr and (f)20hr of milling

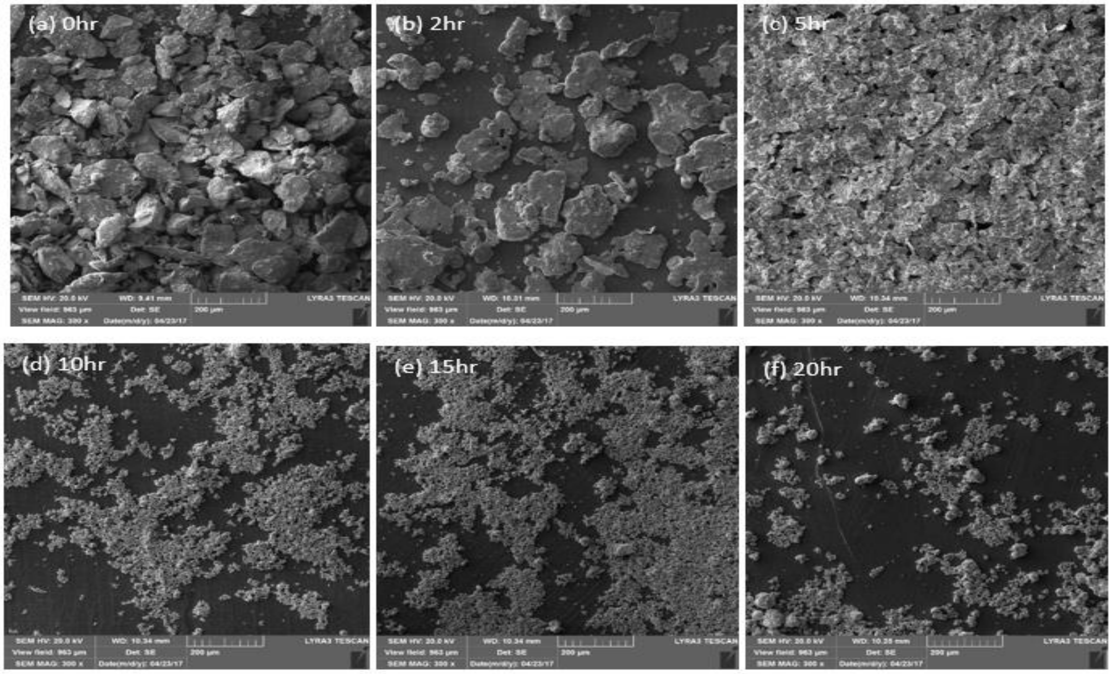

Fig.52. SEM image of ball milled powder D3 after (a)0hr (b) 2hr (c)5hr (d)10hr (e)15hr and (f)20hr of milling

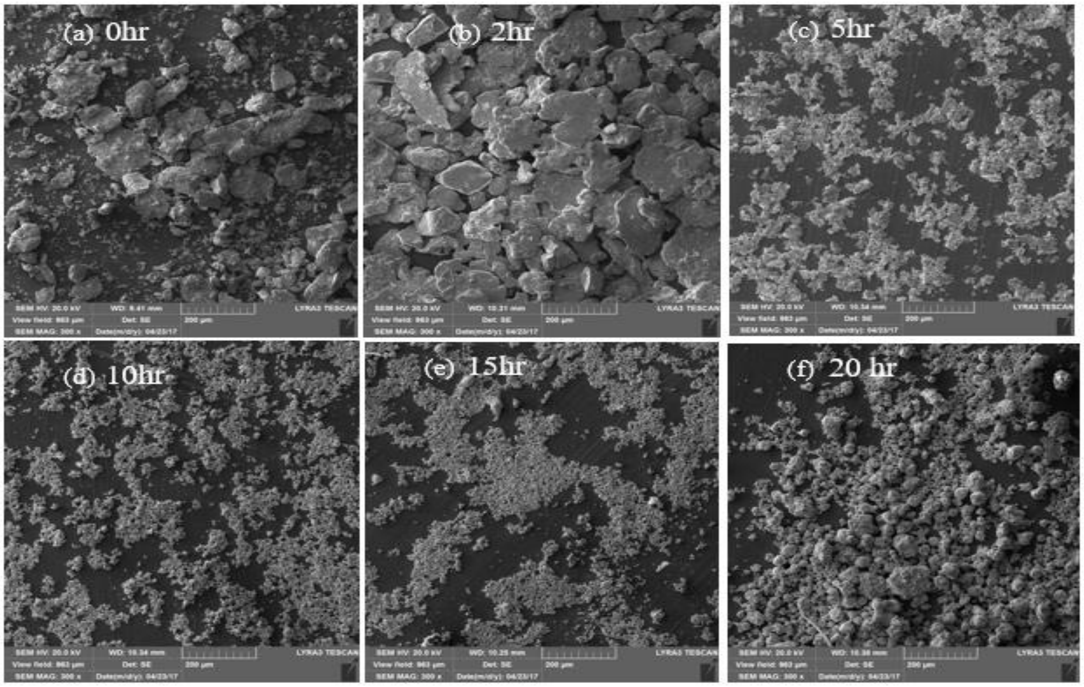

Fig.53. SEM image of ball milled powder D4 after (a)0hr (b) 2hr (c)5hr (d)10hr (e)15hr and (f)20hr of milling

EDX analysis and mapping of elemental distribution in the alloy composition were conducted to 10hr ball milled powder of alloy D1, D2, D3 and D4 represented in the Fig.54(a-i), Fig.55(a-i), Fig.41(a-i), and Fig.56(a-i) respectively. The EDX study showed the quantitative analysis results which confirm the presence of all alloying elements in the powder with approximately designed percentage composition. However, alloying elements such as Mo, Si, and Cu which were less than 1% percent in mixed ration were found to be less than expected. Elemental mapping shows a clear homogenous distribution of alloying elements in all alloy powders. Mapping results justify the presence and appropriate amount of each alloying element such as Fe, Cr, Mn, Mo, Si, N, Cu and Ni in the composition.

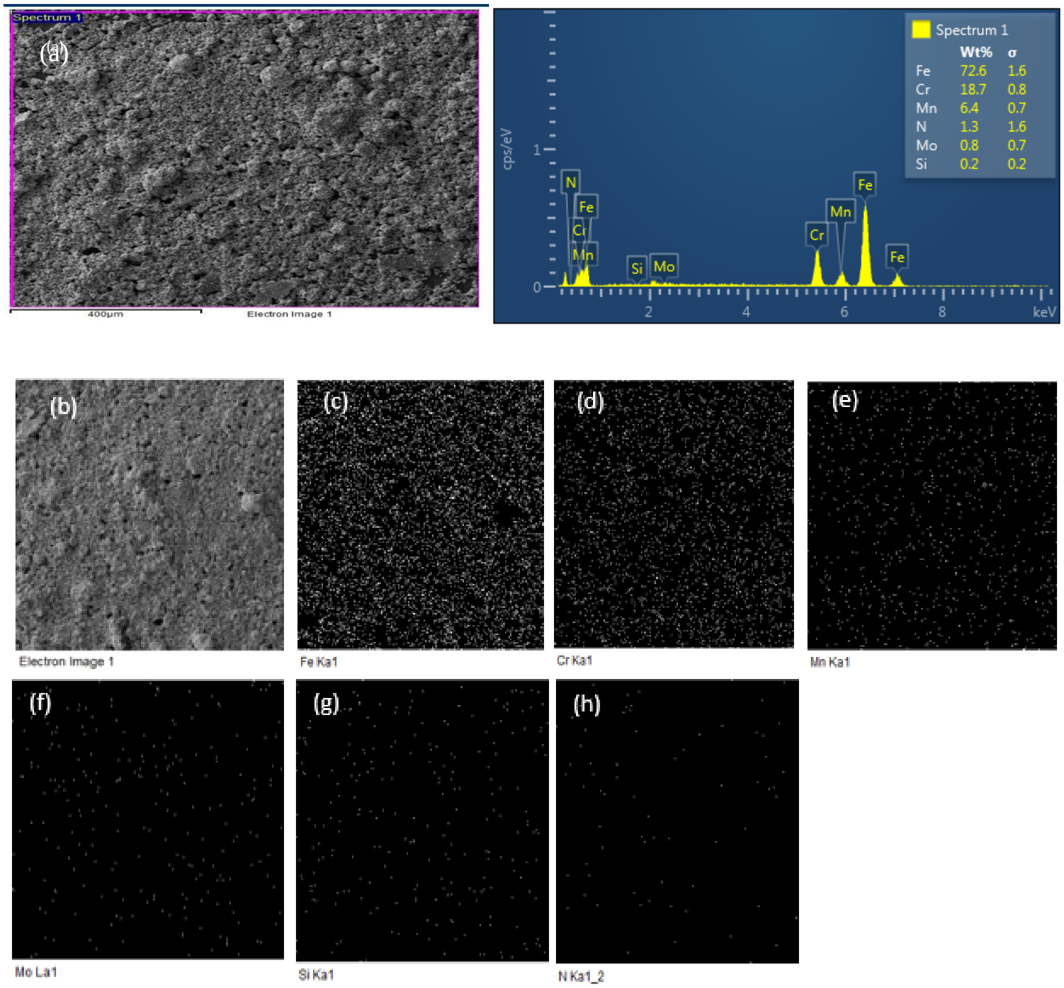

Fig.54. (a) EDX spectra and mapping of (b) 10hr milled powder showing elemental distribution such as (c)Fe (d) Cr (e)Mn (f) Mo (g) Si (h) Si in D1

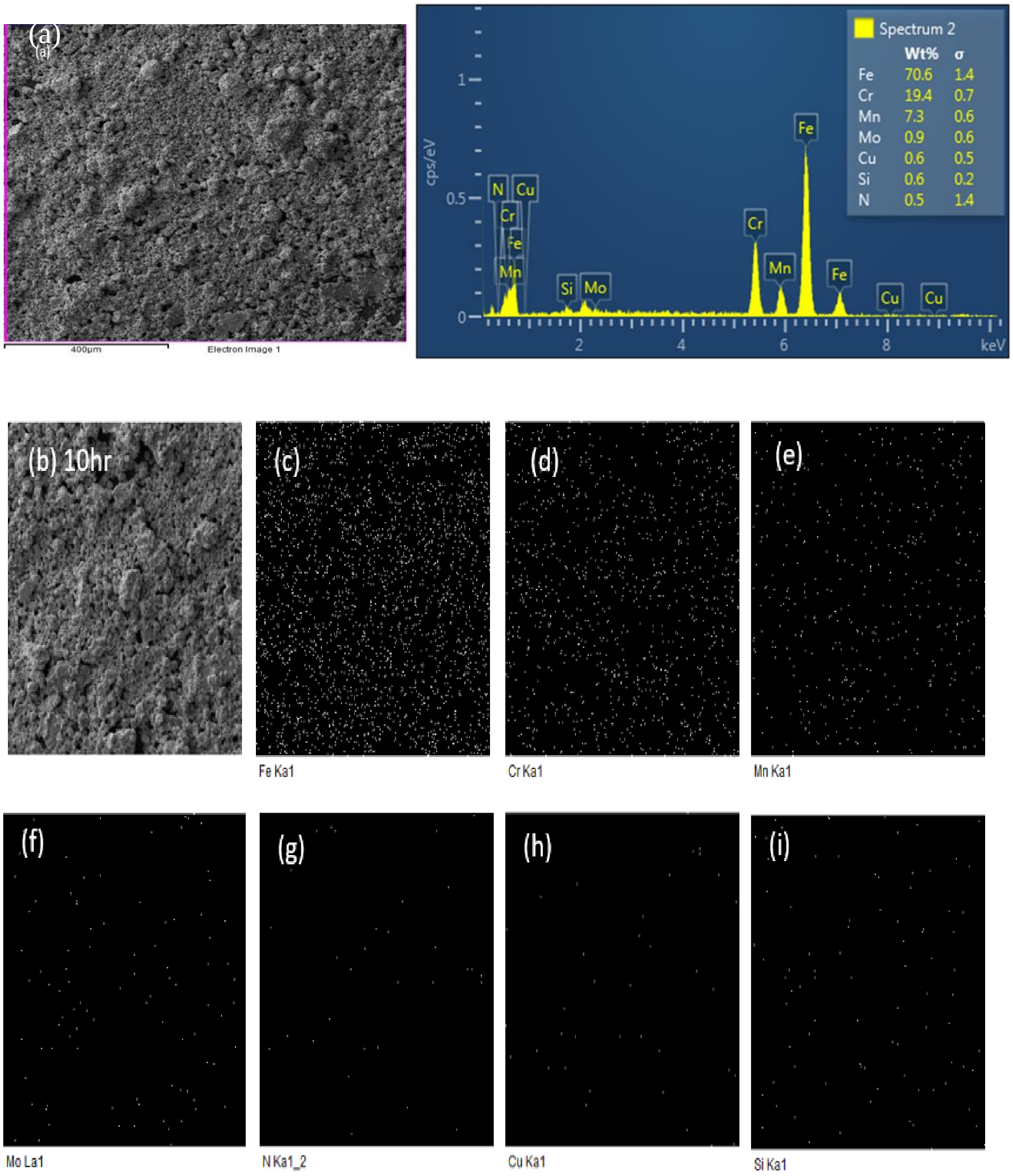

Fig.55. (a) EDX spectra and mapping of (b) 10hr milled powder showing elemental distribution such as (c)Fe (d) Cr (e)Mn (f) Mo (g) N (h) Cu (i) Si in D2

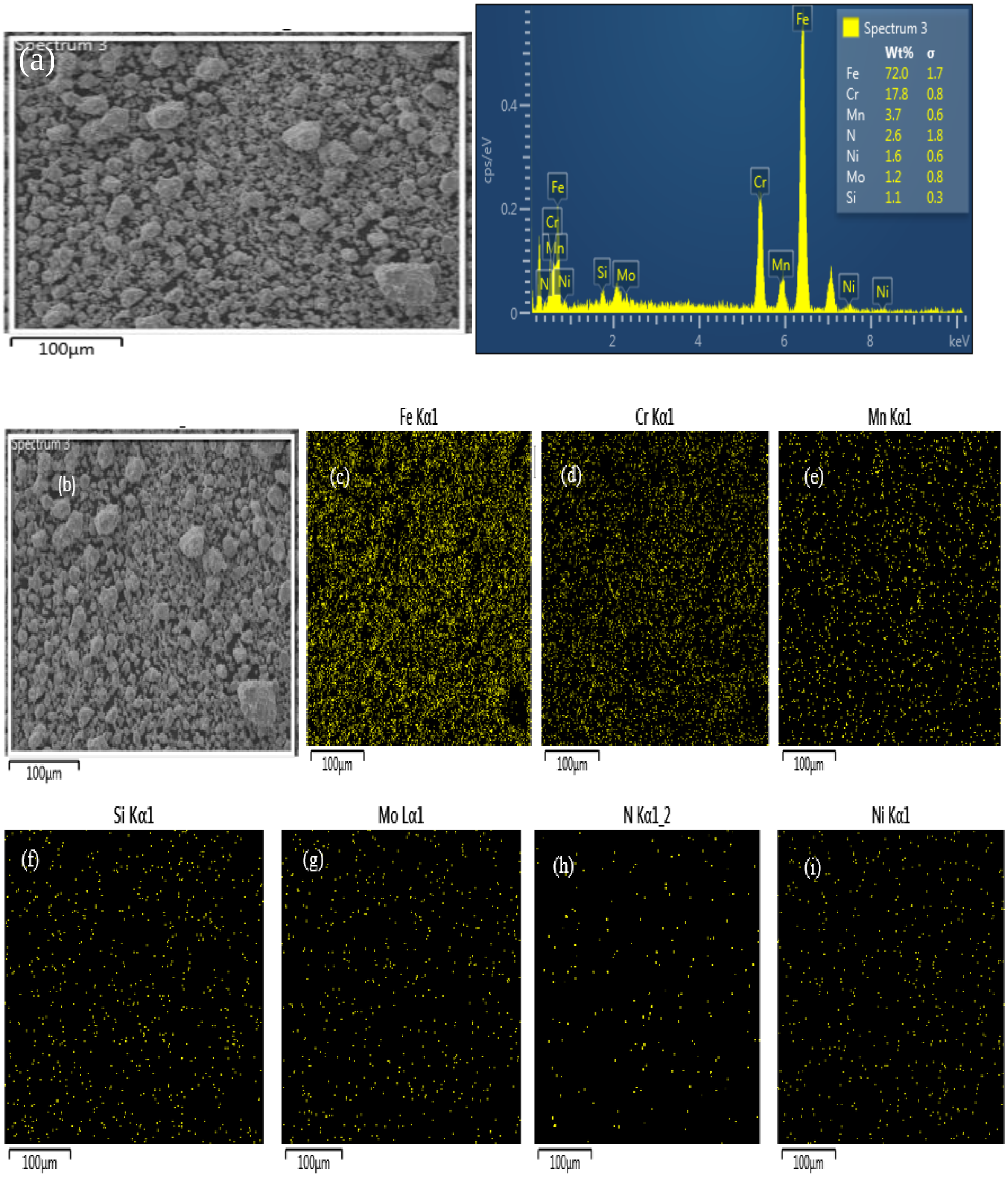

Fig.56. (a) EDX spectra and mapping of (b) 10hr milled powder showing elemental distribution such as (c)Fe (d) Cr (e)Mn (f)Si (g) Mo (h)N (i) Ni in D3

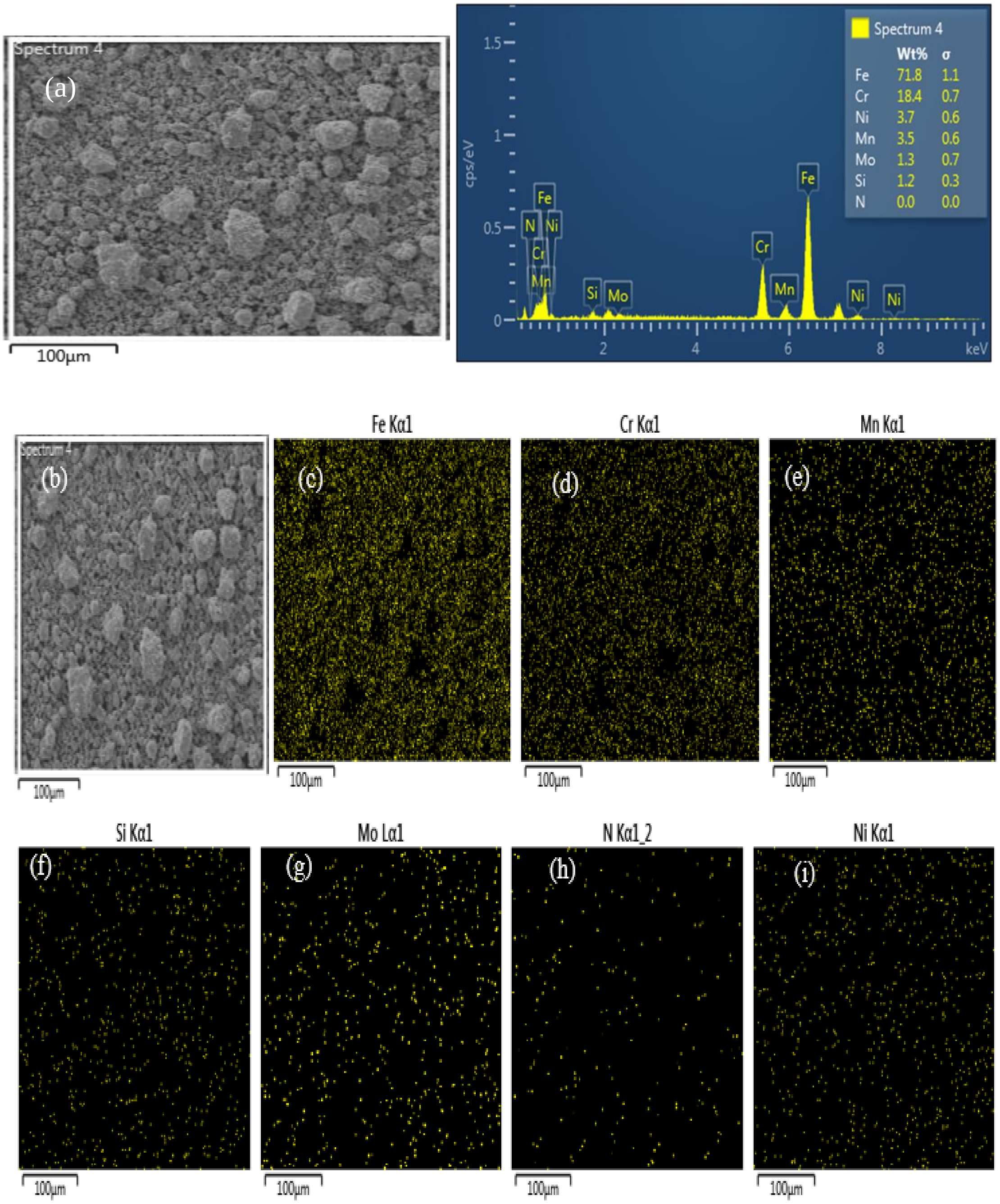

Fig.57. (a) EDX spectra and mapping of (b) 10hr milled powder showing elemental distribution such as (c)Fe (d) Cr (e)Mn (f)Si (g) Mo (h)N (i) Ni in D4

6.2. Consolidation of P/M DSS alloys

6.2.1. Temperature optimization during SPS

Ball milled powder of DSS alloys (D1, D2, D3 & D4) were sintered by Spark plasma sintering techniques (SPS). The sintering parameters were 1000^oC sintering temperature, heating rate 100^oC/min, holding time 10 minutes, the pressure of 50MPa and cooling rate of 200^oC/min. Since electrochemical properties depend on the densification of material, a temperature optimization to achieve higher density sintered sample was conducted. Ball milled powder of Alloy-D2 ($Fe\text{-}Cr_{18}$ $\text{-}Mn_6\text{-}Mo_1\text{-}Si_1\text{-}N_{0.22}\text{-}Cu_1\text{-}Ni_0$), was selected for temperature of optimization whereby sintering temperature was varied at 900^oC, 950 ^oC and 1000 ^oC and keeping other parameters constant as heating rate (100^oC/min), holding time (10 min), pressure (50MPa) and cooling rate (200^oC/min).

After sintering the density was calculated by Archimedes principle as shown in the Fig.31. The weight of sintered specimen was measured air and in a distilled water with a measured density of 0.9991 at 23 ^oC room temperature. The average density obtained from 6 reading was divided by the theoretical density of DSS alloys. In addition to that micro-hardness was calculated

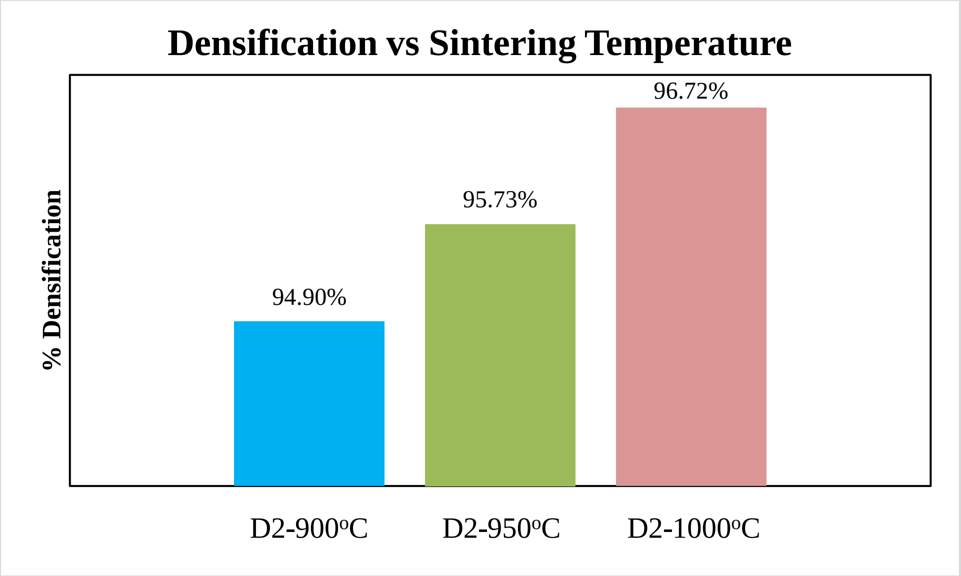

Fig.58(a). Densification at different Sintering temperature.

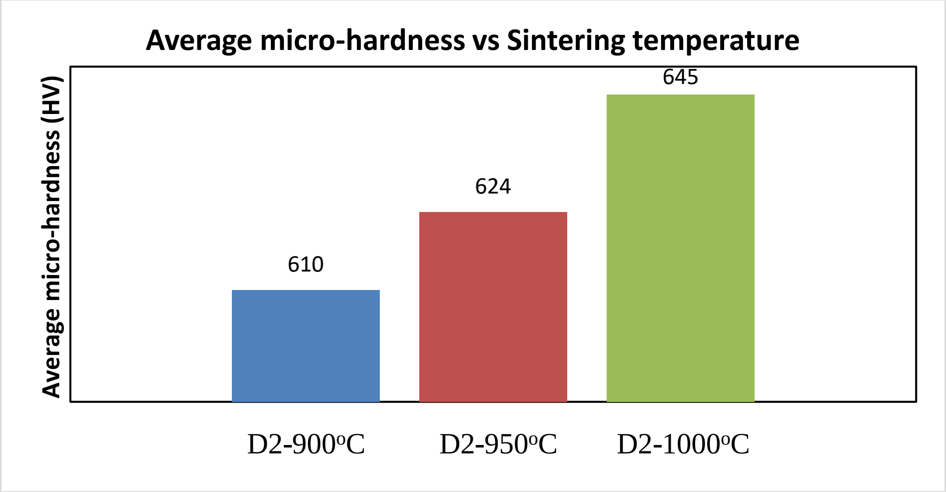

Fig.58(a). Micro-hardness variations at different Sintering temperature

The results in Fig.58 suggested that increase in the sintering temperature has a direct impact on the increase of densification of the alloys. During SPS sintering of Alloy D2, the maximum density was achieved when sintering temperature was 1000^{o}C while lowest was achieve at 900^{o}C. Further, optimization was performed by sintering at 1150^{o}C and 1100^{o}C, however, we observed that there was melting of powder which was going out of graphite die for SPS sintering and causes them to break up upon removing the sintered sample. The reason for higher densification as sintering temperature increase has been reported by Toor et.al [4] who worked on optimization of process parameter for SPS sintered nanostructured ferritic Fe-18Cr-2Si alloy. The maximum densification was achieved at 1100 ^{o}C, however, at 1200 ^{o}C the density decreased due to localized melting. Hussein et.al [85] investigate the effect of temperature on densification of Nb-Zr alloy. Zhang et.al [86] studied the effect of temperature on the densification of Fe-0.8C alloy and suggested that an increase in sintering temperature increase the densification and hardness of the alloy. Also, it has been reported by Liu et.al [87] that specimen sintered at low temperature consist of voids and micro-holes in their microstructure when studying on the density and microhardness of nanocrystalline alumina. Shashanka et.al [19] reported that the increase of sintering temperature increases density due to shrinkage of pore which reduces amount porosity and increases the rate of mass transport which lead to necking and better bonding between the powders. From the result of densification, we concluded that 1000^{o}C sintering temperature is an optimum temperature during our studies.

6.2.2. Spark plasma sintering (SPS) of ball milled powders (D1, D2, D3 &D4) Fe-Cr18 -Mn_x-Mo_1-Si_1-$N_{0.22}$-Cu_y-Ni_z (x = 6, y=0,1,z=3, 5)

Sintering temperature optimized from previous chapter 6.2.1 at 1000°C was used with other parameters such as heating rate 100°C/min, holding time 10 minutes, 50MPa pressure and cooling rate of 200°C/min to synthesize DSS alloys Fe-Cr_{18} -Mn_x-Mo_1-Si_1-$N_{0.22}$-Cu_y-Ni_z (x = 6, y=0, 1, z=3, 5).

6.2.2.1. Density calculations for sintered sample

After sintering the sample were cleaned and grinded to remove unwanted carbon then densities were measured. Density measurement was carried out through Archimedes principle in the equipment shown in the Fig. 31. The weight of each sintered specimen was measured in air and in distilled water and then percentage densities were calculated after taking an average of six readings for each specimen.

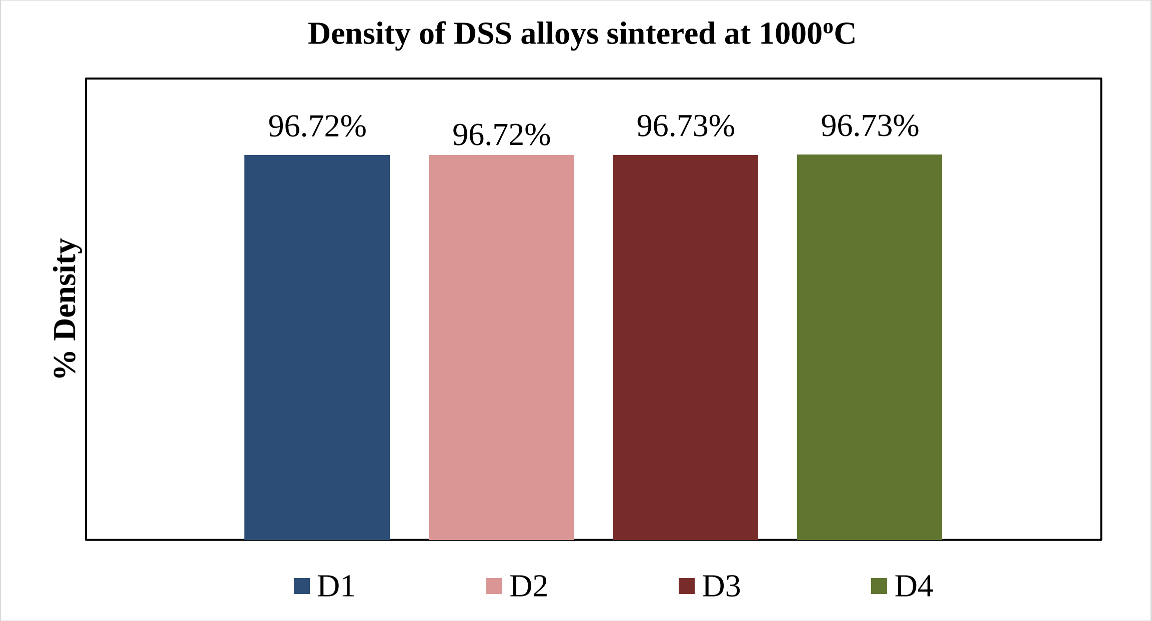

Fig.59. Percentage density of DSS alloys sintered at 1000°C.

The calculated percentage densities of sintered alloys in the Fig.59 shows that the percentage density for all alloys were almost similar except some insignificant fluctuations were observed. The results show the similarity of an influence sintering temperature for all alloys. The maximum percentage density achieved was 97.73% for alloy D4 while the minimum was 96.72% for alloy D2. The density variations do not show any dependable factor.

6.2.3. Characterization of Sintered sample

6.2.3.1. X-ray diffraction (XRD) of sintered samples

Fig.60 shows the XRD patterns of the sintered specimen of DSS alloys D1, D2, D3 and D4 from 20hr of ball-milled powder. The XRD pattern shows the presence of both sharp and crystalline diffraction peak of ferritic (110) and austenitic (111) phases of Duplex stainless steel structure. During ball milling, the DSS alloys powder had undergone structural defects, amorphization, strain, and reduction of a crystalline size which cause an increase in defect sites, shorter diffusion path and non-equilibrium state as well as broadening of diffraction peaks **[19, 88].** After Sintered, atom rearranges in a regular manner as well as the occurrence of sharp crystalline diffraction peaks caused by diffusion **[19, 88].** No evidence of secondary phases such as sigma phase, chi phases, carbides, nitrides, was observed in the XRD patterns of all DSS alloys samples.

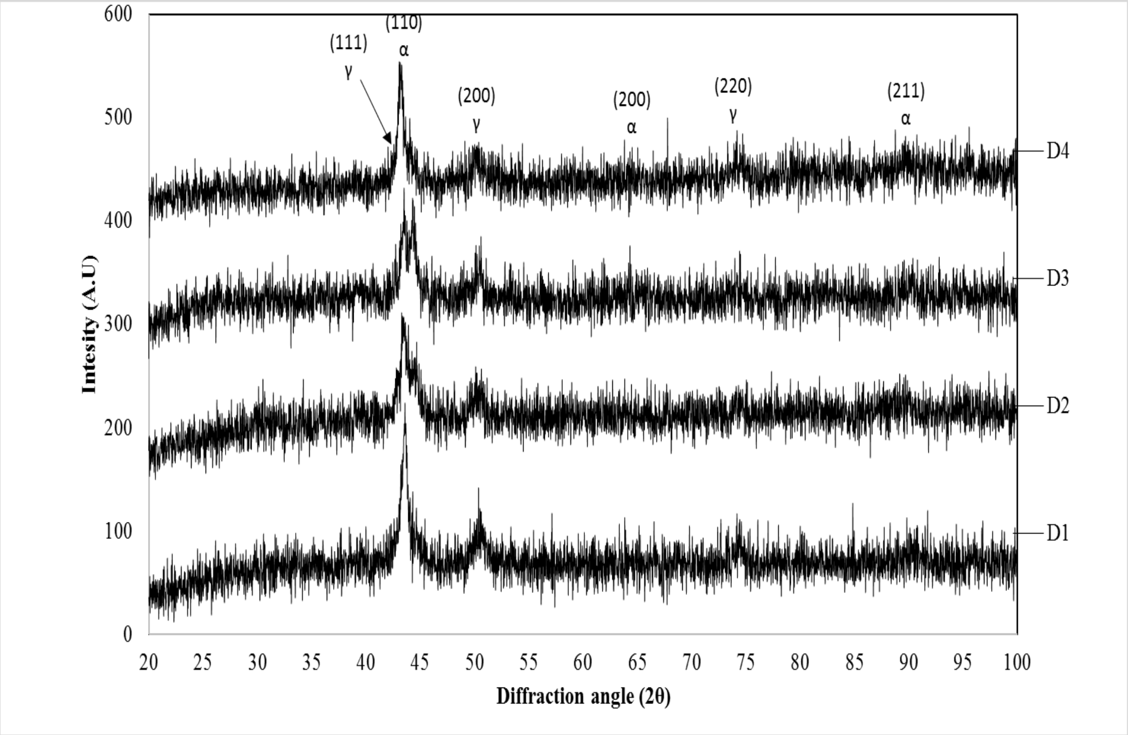

Fig.60. XRD pattern of sintered DSS alloys at 1000°C.

6.2.3.2. Microstructure analysis of Sintered sample

Optical microscope and FE-SEM was used to investigate the microstructure of sintered DSS alloys specimen at 1000^{o}C. The sintered samples were grinded, polished and then etched for 30seconds in glyceregia solution. Fig.61 and Fig.62 show the Optical micrographs and FE-SEM images after glyceregia etching of sintered sample respectively. Optical micrographs in Fig.61 shows the presence of ferrite (dark) and austenite (bright) phases which indicated the duplex microstructure of the sintered alloys. For further study of microstructure, FE-SEM image of one sintered sample was taken at a higher magnification of 140KX which showed the presence of pores in the microstructure. The micrographs image showing porosity is correlated with the reason for less percentage density results obtained for the sintered sample.

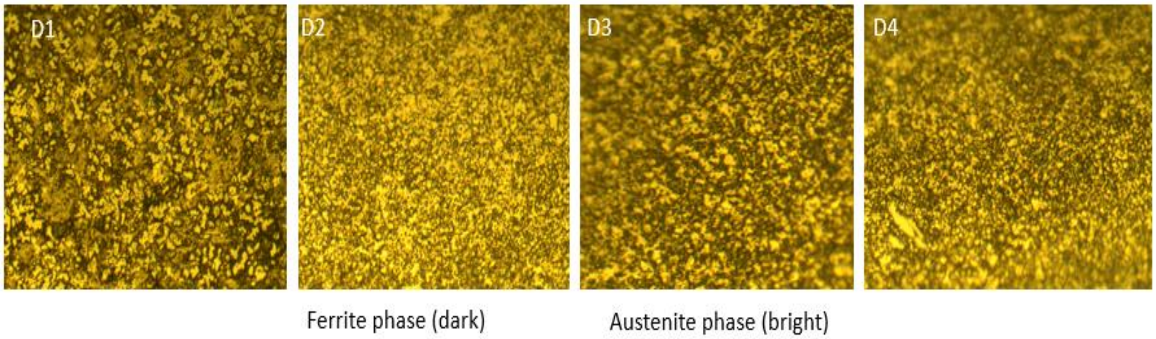

Fig.61. Optical microscope images of sintered DSS alloys at 1000^{o}C.

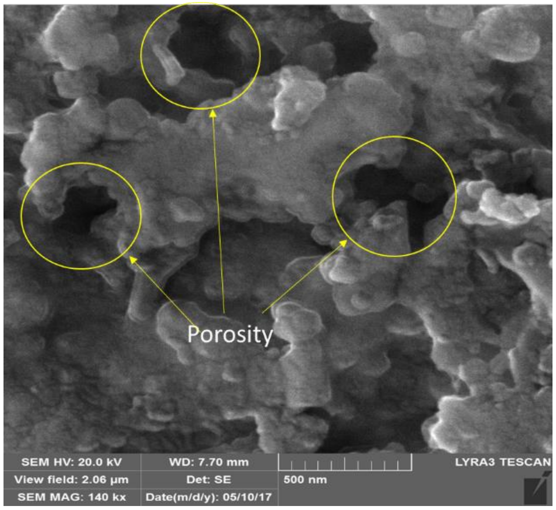

Fig.62. FE-SEM images of sintered DSS alloys specimen at 1000^{o}C.

6.3. Electrochemical investigations of sintered DSS alloys

In this chapter, we have investigated the electrochemical properties of sintered DSS alloys $Fe\text{-}Cr18\text{ -}Mn_x\text{-}Mo_1\text{-}Si_1\text{-}N_{0.22}\text{-}Cu_y\text{-}Ni_z$ *(x = 6, y=0, 1, z=3, 5)* specimens. The specimens were mounted, grinded with emery paper up to 600 grits and later polished with alumina for electrochemical measurements. Different electrochemical measurement techniques such as potentiodynamic polarization PDP and electrochemical impedance spectrometry EIS were carried out to determine corrosion performance of sintered specimen in 0.2M NaCl solution. A three-electrode electrochemical cell was used in corrosion measurements, a graphite rod was used as a counter electrode, saturated calomel electrode SCE was use reference electrode and sintered specimen as working electrode with an exposed surface area of 0.2 cm^2. The solution was de-aerated with nitrogen gas for 20min before the experiment and maintain continuous de-aeration during the experiment. To remove the primary oxide film formed on the surface exposed the specimens were cathodically cleaned for 10 min at – 1.0 V_{SCE} . All the electrode potentials are referred to the SCE scale.

Potentiodynamic polarization tests were performed per ASTM G 5 at a scan rate of 0.5mV/s. For electrochemical impedance spectrometry analysis at open circuit potential, an excitation voltage of 10 mV (peak-to-peak) and an applied frequency ranging from 10 kHz to 10 mHz were used.

Electrochemical measurements investigations were performed using a GAMRY reference 3000 potentiostat /galvanostat /ZRA.

6.3.1. Potentiodynamic polarization, PDP of Sintered alloys

In the Fig.63 represents the potentiodynamic polarization curves of sintered specimens D1, D2, D3 and D4 with the different elemental composition in de-aerated 0.2M NaCl solution. The general passive behavior of sintered alloys was observed for all alloys. Table.2. shows the composition of sintered alloys during designing by the help Schaeffler diagram in Fig.13. The difference in composition of sintered alloys is D1 (6%Mn, 0%Cu), D2 (6%Mn, 1%Cu), D3 (3% Mn, 3%Ni) and D4(3%Mn, 5%Ni).

The results of potentiodynamic polarization in Fig.63 and Table 12 show that all sintered specimen have shown similarity in corrosion potential (E_{corr}) values except for specimen D3(-803mV) which has the lowest E_{corr} value. D1 showed the lowest corrosion current density (i_{corr}) value i.e better corrosion resistance properties and D1 shows the highest value i.e poor corrosion resistance property. The values of i_{corr} increases in the trend of D1 < D3 <D4 <D3. The pitting potential (E_{pit}) values were observed to increase in the trend of D2 < D1 < D3 < D4. The maximum value of E_{pit} was observed in alloy D4 (-390mV) which consist higher amount of Ni (noble element). The passive current density (i_{pass}) values showed that alloy D4 has a less passive current density which implies to have better corrosion resistance properties than other alloys as shown in the trend D4 < D3 < D1 and D2. However, D2 did not show passive behavior trend like other sintered alloys.

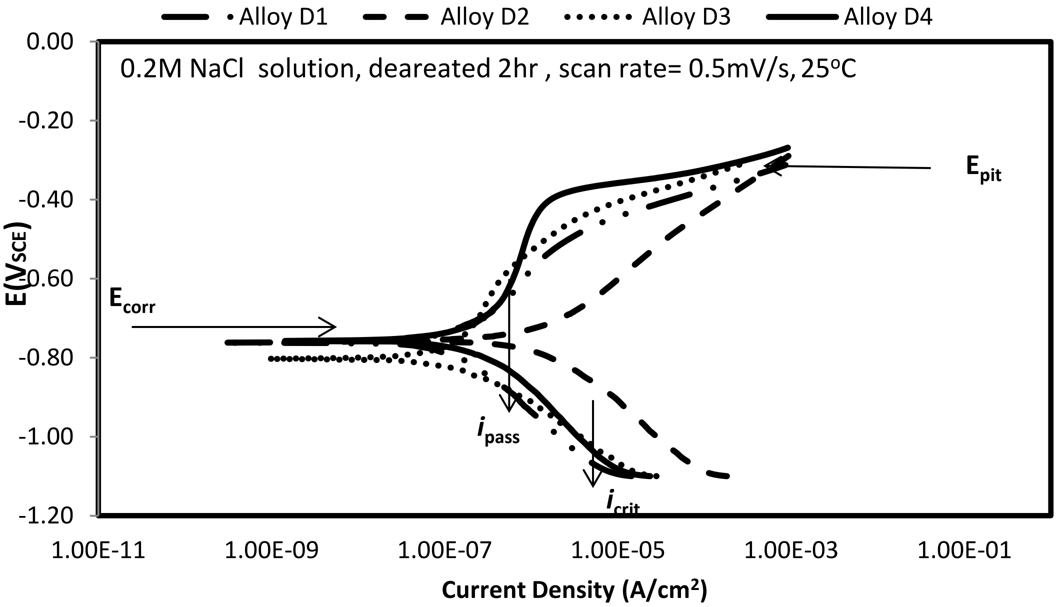

Fig. 63. Potentiodynamic polarization (PDP) curve of sintered DSS alloys in 0.2M NaCl

The phenomenon in the Fig.63 can be explained by the influence of alloying elements on the corrosion properties of sintered alloys. The higher E_{pit} value was recorded for D4 and then followed D3 which has Ni content. Azuma et.al [**78**] reported that Ni increase increases corrosion resistance thus E_{pit} increases. The lower E_{pit} was reported for D1 and D2 which has a higher amount of Mn (active element) than D3 and D4. Mn has a negative impact on corrosion resistance hence the increase in Mn decrease the pitting potential

[8,27,90,91]. The passive current density i_{pass} of alloy D4 was the highest followed by D3 in which its content has the amount of Ni. Nickel increase had a positive impact on the pitting potential **[78,98]** hence the Epit of D4 (5%Ni) was the highest and then followed by D3(3%Ni). The decrease in Mn amount of D4 and D3 has also increased the E_{pit} values. It is believed that Mn enhances formation of Mn sulfide and oxide which initiates pitting formation hence decrease pitting potential [**6,8,17,27,90-92**]. This reason can also be attributed to the lower pitting potential of D1 and D2 alloys which consist of 6% Mn in their composition. The activeness behavior of alloy D2 in Fig.63 in comparison to other sintered alloys is attributed to the Cu content in its composition. It has been reported by Ujiro et.al [**68**] and Sourisseau et.al [**69**] that Cu has both harmful and beneficial effect on the corrosion properties of stainless steel. The tendency of alloy D2 can be attributed to the harmful effect of copper on the corrosion resistance properties of stainless steel. Banas et.al [**70]** that the increase in copper content in stainless steel can stimulate the active-passive transition of the alloy.

Table.12. Corrosion measurements values of DSS after PDP in 0.2M NaCl

Specimen	**E_{corr} (mV)**	**i_{corr} (A/cm^2)**	**i_{pass} (A/cm^2) at -525 mV**	**E_{pit} (mV)**
Alloy D1	-762	2.48 E-10	1.82 E-6	-505
Alloy D2	-755	1.33 E-8	2.60 E-5	-571
Alloy D3	-803	9.08 E-10	1.07 E-6	-467
Alloy D4	-757	1.56 E-9	7.93 E-7	-390

6.3.2. Electrochemical Impedance Spectrometry, EIS

In the Fig.64, the electrochemical impedance spectrometry analysis was carried out in 0.2M NaCl solution under open circuit potential at room temperature. The Nyquist impedance spectra during EIS analysis in Fig.64 shows the semicircle spectra of the sintered specimens. The larger the semicircle spectra the higher is the polarization resistance i.e better corrosion resistance property of the alloy. The impedance values are recorded for alloy D4 and the lowest for alloy D2 as shown in Table13 calculated from one-time constant phase element (CPE) equivalent circuit. The impedance values increase in the trend of D2 < D1 < D3 < D4. Nyquist plot of sintered alloy D1, D3, and D4 shows the passive behavior of the alloys while sintered alloy D2 showed an active behavior.

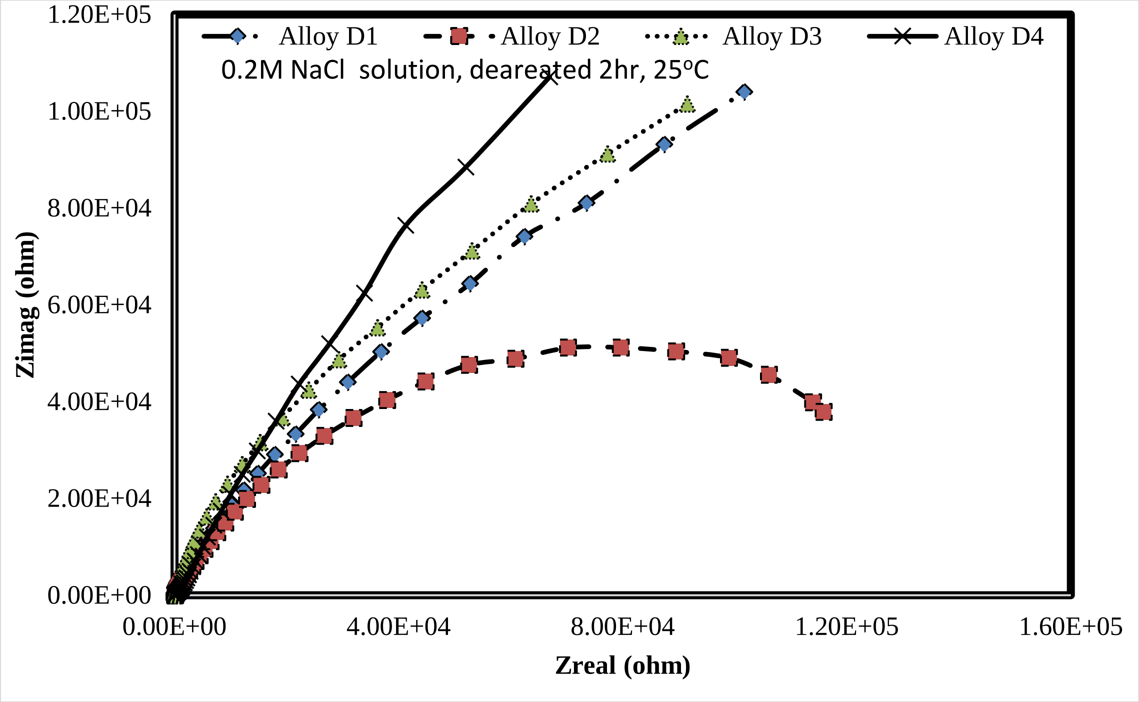

Fig.64. EIS spectra of sintered alloys in the 0.2M NaCl.

The higher polarization resistance of alloy D4 is due to higher amount of Ni **[78,98]** which makes its passive film more stable than D3 and other alloys (D1 & D2). Alloy D1 and D2 have small spectra due to higher Mn (6%) content which decreases the stability of passive film from inclusions such as MnS and MnO **[6,8,17,27].** Toor et.al **[90,91]** reported on the effect of Mn on passivation of stainless steel to be caused by nanosize MnO precipitates formed on the passive film. These precipitates act as pitting initiation site which later propagates and reduces the resistance of the passive film. Alloy D2 was observed to have small semicircle spectra in comparison to alloy D1 with the same amount of Mn except for D' has 1%Cu. The less polarization resistance of D2 is reported due to the harmful effect of Cu on the corrosion resistance of stainless steel. Ujiro et. al [68] reported that chlorides ions reduce the stability of Cu deposited on the passive film.

A CPE equivalent circuit in Fig.66 was established to simulated the measured impedance values of sintered alloys in 0.2M NaCl solution. The Equivalent circuit composed of model parameters such as polarization resistance Rp, solution resistance Rs, *n* represents a coefficient related with the homogeneity of the system and pseudocapacitance of the system Y_o (where n=1 for an ideal capacitor) **[79]**. The CPE impedance representation is given by

$$Z_{CPE} = 1/Y_o(j\omega)^n \qquad \textbf{[79]}$$

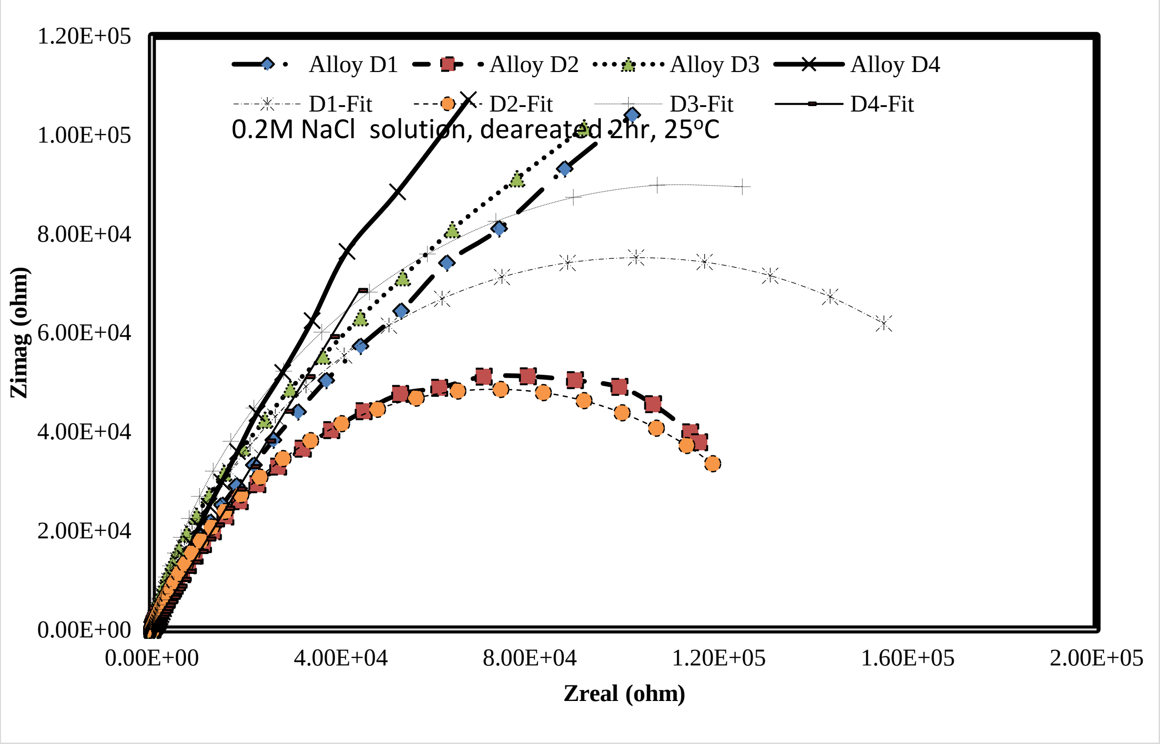

Fig.65. EIS spectra with a CPE equivalent circuit fitting of sintered alloys in the 0.2M NaCl.

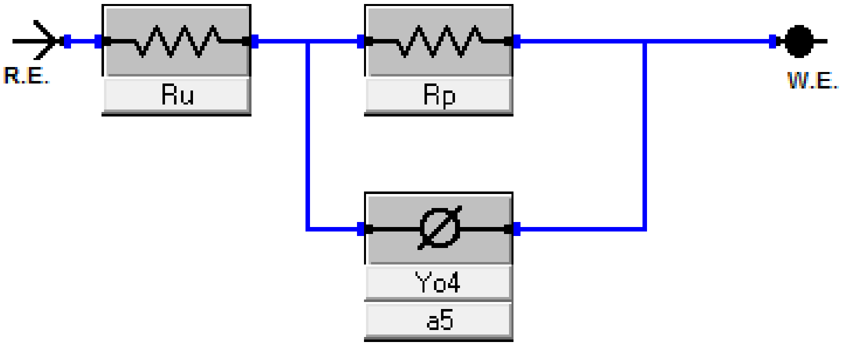

Fig.66.CPE equivalent circuit tested in EIS data of sintered alloys

Table.13. EIS analysis data from fit of CPE equivalent circuit

Specimen	**Polarization Resistance Rp (Ohm)**	**Solution resistance (Ohm)**
Alloy D1	2.06 E5	32.81
Alloy D2	1.45 E5	31.65
Alloy D3	2.28 E5	36.71
Alloy D4	1.69 E11	29.01

CHAPTER 7

CONCLUSIONS

Duplex stainless steels alloys were developed by casting and powder metallurgy technique to attain better corrosion resistance properties. Cast DSS were produced in vacuum induction furnace with variation in their composition as shown in Table 3 to form ingots. To obtain microstructure of 40% ferrite and 60% austenite the alloys were solution annealed at 1120^{o}C. To analyze the presence of intermetallic (secondary) phases in the alloys a heat treatment (aging) was carried out at 1050^{o}C.

Powder metallurgy samples were prepared from pure elements powder by a mechanical alloying technique by using planetary ball milling and then followed by spark plasma sintering. During ball milling phase evolution and ball milled powder morphology were investigated. Spark plasma sintering process parameters were optimized to obtain higher densification of the alloy for better electrochemical properties.

Electrochemical properties of fabricated cast and powder metallurgy alloys were investigated in different solutions such chloride, acidic and simulated body fluid (SBF). Electrochemical measurements used to investigate the corrosion properties were potentiodynamic polarization, electrochemical impedance spectrometry, and electrochemical noise analysis.

The followings can be concluded from this study:

7.1. Cast Duplex stainless steel

- Optical microscope and SEM images showed that clear duplex structure of ferrite and austenite phase was present with no evidence of secondary phases. EDX analysis showed the proper distribution of alloying elements in ferrite and austenite phase responsible for their formation.
- XRD results showed that DSS alloys were free of inclusions and secondary phases such as sigma phase after aging for 50hrs and nitrides precipitate after aging for 3hrs from 600^{o}C – 900^{o}C. The reason for this was due to less amount of Cr, N and Mo used which contribute to the formation of sigma and nitride phase.

- PDP, EIS and ENA experiments performed indicated that, among the designed alloys, Alloy 2 with composition (Bal.Fe-18Cr-5Mn-1Mo-1Si-1Cu-0.22N) showed good corrosion resistance properties in comparison to AISI 304SS, with lower production cost (with the optimum amount of alloying elements).
- In Simulated body fluid test at different temperatures and immersion times, Alloy 2 and 304 SS showed similar E_{pit} values while EIS results showed that polarization resistance Rp increased as immersion time increased for all alloys.
- In agitated condition at different flow rate corrosion properties decreased as the rotation speed increased from 0 to 1000 rpm. The flow of solution decreased the corrosion resistance properties (E_{pit}) of the Alloys due to the shear stress acting on a passive film formed the surface.

7.2. Powder metallurgy of Duplex stainless steel

- Mechanical alloying of pure elements such as Fe, Cr, Mn, Mo, Si, Cu and Ni under N_2 atmosphere led to the development of nanocrystalline Duplex Stainless steels by ball milling of mixed elemental powder of different compositions for 20hr.
- Characterization of ball milled powder picked after 0, 5, 10, 15 and 20 hours was conducted by XRD and SEM for phase evolution and morphological investigations. XRD showed the transformation of ferrite to austenite phase during ball milling. Morphological analysis of ball milled powder showed fracturing, cold welding, and agglomeration during mechanical alloying.
- Crystalline size and lattice parameter variation during ball milling resulted in ferrite to austenite phase transformation after 10hrs of milling.
- Temperature optimization was performed by measuring density variation at different sintering temperature. Maximum percentage (%) density of 92.72% (in comparison to theoretical density 7.805 g/cm^3) was achieved at 1000 ^oC.
- XRD spectra of sintered alloys showed the presence of ferrite and austenite phases (duplex structure) and no evidence of secondary phases were observed.
- Electrochemical properties of sintered alloys were investigated in 0.2M NaCl solution. In PDP, alloy D4 showed better corrosion properties such as higher E_{pit}

due to its higher Ni content and EIS results showed higher polarization resistance for Alloy D4 due to its higher Ni content.

- Alloy D2 exhibited active behavior due to the negative effect of Cu on its composition.

REFERENCES

1. Klar, E., Samal, P. (2007). Powder Metallurgy Stainless Steel, Processing, Microstructure, and Properties. *ASM International*.
2. Wronski, A. S., & Mascarenhas, J. M. G. (2004). Recent Developments in the Powder Metallurgy Processing of Steels. *Materials Science Forum*, *455–456*, 253–257.
3. Froideval, A., Iglesias, R., Samaras, M., Schuppler, S., Nagel, P., Grolimund, D., Hoffelner, W. (2007). Magnetic and structural properties of FeCr alloys. Physical Review Letters, 99(23), 5–8.
4. Toor, I.H., Ahmed, J., Hussein, M. A., & Al-Aqeeli, N. (2016). Optimization of process parameters for spark plasma sintering of nanostructured ferritic Fe-18Cr-2Si alloy. *Powder Technology*, *299*(May), 62–70.
5. Alvarez armas, I. (2008). Duplex Stainless Steels : Brief History and Some Recent Alloys. *Recent Patents on Mechanical Engineering*, *1*, 51–57.
6. Wen, S. (2001). Metallurgical Evaluation of Cast Duplex Stainless Steels and Their Weldments.
7. Datta, P., & Upadhyaya, G. S. (2001). Sintered duplex stainless steels from premixes of 316L and 434L powders. *Materials Chemistry and Physics*, *67*(1-3), 234–242.
8. Li, J., Zhang, Z., Chen, H., Xiao, X., Zhao, J., & Jiang, L. (2012). New economical 19Cr duplex stainless steels. *Metallurgical and Materials Transactions A: Physical Metallurgy and Materials Science*, *43*(2), 428–436.
9. Jiang, D. Wei, Ge, C. Sheng, Zhao, X. Juan, Li, J., Shi, L. Lu, & Xiao, X. shan. (2012). 22Cr High-Mn-N Low-Ni Economical Duplex Stainless Steels. *Journal of Iron and Steel Research International*, *19*(2), 50–56.
10. Hanninen, H., Romu, J., Ilola, R., Tervo, J., & Laitinen, A. (2001). Effects of processing and manufacturing of high nitrogen-containing stainless steels on their mechanical, corrosion and wear properties. *Journal of Materials Processing Technology*, *117*(3), 424–430.

11. Li, J., Zhang, Z., Chen, H., Xiao, X., Zhao, J., & Jiang, L. (2012). New economical 19Cr duplex stainless steels. Metallurgical and Materials Transactions A: Physical Metallurgy and Materials Science, 43(2), 428–436.

12. Jiang, D. Wei, Ge, C. Sheng, Zhao, X. Juan, Li, J., Shi, L. Lu, & Xiao, X. Shan. (2012). 22Cr High-Mn-N Low-Ni Economical Duplex Stainless Steels. Journal of Iron and Steel Research International, 19(2), 50–56. http://doi.org/10.1016/S1006-706X(12)60059-4

13. Toor, I. ul H., Hyun, P. J., & Kwon, H. S. (2008). Development of high Mn-N duplex stainless steel for automobile structural components. Corrosion Science, 50(2), 404–410.

14. Zhang, Z. Xing, Ran, Q. Xuan, Xu, Y. Lai, Yu, X. Jiang, Jiang, D. Wei, & Xiao, X. Shan. (2014). A New Series of Mo-free 21. 5Cr-3. 5Ni-x W-0. 2N Economical Duplex Stainless Steels. Journal of Iron and Steel Research International, 21(1), 69–75.

15. Chen, H., Ding, T. Zuo, Li, J., Xiao, X. Shan, Zhao, J. Liang, & Jiang, L. Zhu. (2011). A New Economical Sigma-Free Duplex Stainless Steel 19Cr-6Mn-1. 0Mo-0. 5Ni-0. 5W-0. 5Cu-0. 2N. Journal of Iron and Steel Research International, 18(4), 52–57.

16. Ran, Q., Li, J., Xu, Y., Xiao, X., Yu, H., & Jiang, L. (2013). Novel Cu-bearing economical 21Cr duplex stainless steels. Materials and Design, 46, 758–765.

17. Garcia, C., Martin, F., Blanco, Y., de Tiedra, M. P., & Aparicio, M. L. (2009). Corrosion behavior of duplex stainless steels sintered in nitrogen. Corrosion Science, 51(1), 76–86.

18. Dobrzanski, L. A., Brytan, Z., Actis Grande, M., & Rosso, M. (2007). Corrosion behavior of vacuum sintered duplex stainless steels. *Journal of Materials Processing Technology*, *191*(1–3), 161–164.

19. Shashanka, R., & Chaira, D. (2015). Development of nano-structured duplex and ferritic stainless steels by pulverisette planetary milling followed by pressureless sintering. Materials Characterization, 99, 220–229.

20. Shashanka, R., & Chaira, D. (2015). Optimization of milling parameters for the synthesis of the nano-structured duplex and ferritic stainless steel powders by high energy planetary milling. Powder Technology, 278, 35–45.
21. Shashanka, R., & Chaira, D. (2014). Phase transformation and microstructure study of nano-structured austenitic and ferritic stainless steel powders prepared by planetary milling. *Powder Technology*, *259*, 125–136.
22. Amini, R., Hadianfard, M. J., Salahinejad, E., Marasi, M., & Sritharan, T. (2009). Microstructural phase evaluation of high-nitrogen Fe-Cr-Mn alloy powders synthesized by the mechanical alloying process. *Journal of Materials Science*, *44*(1), 136–148.
23. Tehrani, F., Abbasi, M. H., Golozar, M. A., & Panjepour, M. (2011). The effect of particle size of iron powder on α to γ Transformation in the nanostructured high nitrogen Fe-Cr-Mn-Mo stainless steel produced by mechanical alloying. *Materials Science and Engineering A*, *528*(12), 3961–3966.
24. Haghir, T., Abbasi, M. H., Golozar, M. A., & Panjepour, M. (2009). Investigation of α to γ transformation in the production of a nanostructured high-nitrogen austenitic stainless steel powder via mechanical alloying. *Materials Science and Engineering A*, *507*(1–2), 144–148.
25. Brytan, Z., Dobrzanski, L. A., Grande, M. A., & Rosso, M. (2007). Influence of sintering parameters on the properties of duplex stainless steel, *20*(2), 231–234.
26. Enayati, M. H., & Bafandeh, M. R. (2008). Phase transitions in nanostructured Fe-Cr-Ni alloys prepared by mechanical alloying. *Journal of Alloys and Compounds*, *454*(1–2), 228–232.
27. Llorca Isern, N., Lopez Luque, H., Lopez Jimonez, I., & Biezma, M. V. (2016). Identification of sigma and chi phases in duplex stainless steels. *Materials Characterization*, *112*, 20–29.
28. Association, I. M. (2009). Practical Guidelines for the Fabrication of Duplex Stainless Steel. *International Molybdenum Association*, 1–.
29. Merello, R., Botana, F. J., Botella, J., Matres, M. V., & Marcos, M. (2003). Influence of chemical composition on the pitting corrosion resistance of non-

standard low-Ni high-Mn–N duplex stainless steels. *Corrosion Science*, *45*(5), 909–921.

30. Liou, H., Pan, Y., Hsieh, R., & Tsai, W. (2001). Effects of Alloying Elements on the Mechanical Properties and Corrosion Behaviors of 2205 Duplex Stainless Steels. *Journal of Materials Engineering and Performance*, *10*(April), 231–241.
31. Kah, P., & Martikainen, J. (2013). Influence of shielding gases in the welding of metals. *International Journal of Advanced Manufacturing Technology*, *64*(9-12), 1411–1421.
32. Potgieter, J. H., Olubambi, P. A., Cornish, L., Machio, C. N., & Sherif, E. S. M. (2008). Influence of nickel additions on the corrosion behavior of low nitrogen 22% Cr series duplex stainless steels. *Corrosion Science*, *50*(9), 2572–2579.
33. Chan, K. W., & Tjong, S. C. (2014). Effect of secondary phase precipitation on the corrosion behavior of duplex stainless steels. *Materials*, *7*(7), 5268–5304.
34. Yang, Y., Cao, J., & Gu, Y. (2015). Investigation on the solution treated behavior of economical 19Cr duplex stainless steels by Mn addition. *Materials and Design*, *83*, 820–828.
35. Lee, J.S., Kim, S.T., Lee, I.S., Kim, G.T., Kim, J.S., & Park, Y.S. (2012). Effect of Copper Addition on the Active Corrosion Behavior of Hyper Duplex Stainless Steels in Sulfuric Acid. *Materials Transactions*, *53*(6), 1048–1055.
36. Reis, G. S., Jr, A. M. J., & Balancin, O. (2000). Influence of the Microstructure of Duplex Stainless Steels on their Failure Characteristics During Hot Deformation 2. Materials and Experimental Procedures. *Materials Research*, *3*(2), 31–35.
37. Nirosta, K. T. (2001). *Practical Guidelines for the Fabrication of Duplex Stainless Steels*.
38. Paulraj, P., & Garg, R. (2015). Effect of Intermetallic Phases on Corrosion Behavior and Mechanical Properties of Duplex Stainless Steel and Super-Duplex Stainless Steel. *Advances in Science and Technology Research Journal*, *9*(27), 87–105.
39. Magnabosco, R. (2009). Kinetics of sigma phase formation in a Duplex Stainless Steel. *Materials Research*, *12*(3), 321–327.

40. Hsieh, C.-C., & Wu, W. (2012). Overview of Intermetallic Sigma (?) Phase Precipitation in Stainless Steels. *ISRN Metallurgy*, *2012*(4), 1–16.
41. Hwang, T. H., Kim, J. H., Kim, K. H., Moon, W. J., & Kang, C. Y. (2014). Effect of R-phase on impact toughness of 25Cr-7Ni-4Mo super duplex stainless steel. *Metals and Materials International*, *20*(1), 13–17.
42. Ramirez, a J., Lippold, J. C., & Brandi, S. D. (2003). The relationship between chromium nitride and secondary austenite precipitation in duplex stainless steels. *Metallurgical and Materials Transactions A*, *34*(8), 1575–1597.
43. Maetz, J.-Y., Douillard, T., Cazottes, S., Verdu, C., & Kléber, X. (2016). M23C6 carbides and Cr2N nitrides in aged duplex stainless steel: A SEM, TEM and FIB tomography investigation. *Micron*, *84*, 43–53.
44. Sahu, J. K., Krupp, U., Ghosh, R. N., & Christ, H. J. (2009). Effect of 475 ^{o}C embrittlement on the mechanical properties of duplex stainless steel. *Materials Science and Engineering A*, *508*(1-2), 1–14.
45. Suryanarayana, C., Ivanov, E., & Boldyrev, V.. (2001). The science and technology of mechanical alloying. Materials Science and Engineering: A, 304–306, 151–158.
46. Suryanarayana, C. (1995). Mechanical Alloying and Milling. *Key Engineering Materials*, *103*, 113–124.
47. V. Monov, B. Sokolov, S. Stoenchev, Grinding in Ball Mills: Modeling and Process Control I. *Introduction*, 12 (2012) 51–68.
48. Keller, C., Tabalaiev, K., Marnier, G., Noudem, J., Sauvage, X., & Hug, E. (2016). Influence of spark plasma sintering conditions on the sintering and functional properties of an ultra-fine grained 316L stainless steel obtained from ball-milled powder. *Materials Science and Engineering A*, *665*(October), 125–134.
49. Munir, Z. A., Anselmi-Tamburini, U., & Ohyanagi, M. (2006). The effect of electric field and pressure on the synthesis and consolidation of materials: A review of the spark plasma sintering method. *Journal of Materials Science*, *41*(3), 763–777.
50. Pakseresht, A. H., Javadi, A. H., Bahrami, M., Khodabakhshi, F., & Simchi, A. (2016). Spark plasma sintering of a multilayer thermal barrier coating on Inconel

738 superalloy: Microstructural development and hot corrosion behavior. *Ceramics International*, *42*(2), 2770–2779.

51. Fc Tokita, M. (1994). Mechanism of Spark Plasma Sintering. *Proceeding of NEDO International Symposium on Functionally Graded Materials*, (Mmc), 22.
52. E. McCafferty, Introduction to corrosion science. *Springer*, 2010.
53. Ha, H. Y., Jang, M. H., Lee, T. H., & Moon, J. (2014). Interpretation of the relation between ferrite fraction and pitting corrosion resistance of commercial 2205 duplex stainless steel. *Corrosion Science*, *89*(C), 154–162.
54. García, C., Martin, F., & Blanco, Y. (2012). Effect of sintering cooling rate on the corrosion resistance of powder metallurgy austenitic, ferritic and duplex stainless steels sintered in nitrogen. *Corrosion Science*, *61*, 45–52.
55. Datta, H. P. A. (1999). The sintering of duplex PM. *Corrosion*, (January), 0–2.
56. Lo, K. H., Shek, C. H., & Lai, J. K. L. (2009). Recent developments in stainless steels. *Materials Science and Engineering R: Reports*, *65*(4-6), 39–104.
57. Wen, S. (2001). Metallurgical Evaluation of Cast Duplex Stainless Steels and Their Weldments.
58. Dorofeev, G. A., Sapegina, I. V, Ladyanov, V. I., Pushkarev, B. E., Pechina, E. A., & Prokhorov, D. V. (2012). Mechanical alloying and severe plastic deformation of nanocrystalline high-nitrogen stainless steels. *Phys. Metals Metallog. 113*(10), 963–973.
59. Martin, F., Garcia, C., & Blanco, Y. (2011). Effect of chemical composition and sintering conditions on the mechanical properties of sintered duplex stainless steels. *Materials Science and Engineering A*, *528*(29–30), 8500–8511.
60. Cisneros, M. M., Lopez, H. F., Mancha, H., Rincon, E., Vazquez, D., Perez, M. J., & De La Torre, S. D. (2005). Processing of Nanostructured High Nitrogen Stainless Steel by Mechanical Alloying. *Metallurgical and Materials Transactions A*, *36*(5), 1309–1316.
61. Toor, I. ul H. (2016). Effect of sintering holding time on the corrosion properties of nanostructured Fe-18Cr-2Si Alloy prepared by SPS. *International Journal of Electrochemical Science*, *11*(4), 2897–2908.

62. Ciuca, O. P., Ota, M., Deng, S., & Ameyama, K. (2013). Harmonic Structure Design of a SUS329J1 Two-Phase Stainless Steel and Its Mechanical Properties, *54*(9), 1629–1633.

63. Cui, G., Wei, X., Olevsky, E. A., German, R. M., & Chen, J. (2016). Preparation of high-performance bulk Fe-N alloy by spark plasma sintering. *Materials and Design*, *90*(October), 115–121.

64. Schaeffler, A.L. (1949). Constitution diagram for stainless steel weld metal. *Metal Progress, 56 (11) (1949), p. 680*
65. Long, C.J. & DeLong, W.T... (1973). The ferrite content of austenitic stainless steel weld metal. *Welding Journal, 52 (7) (1973), p. 281 July*
66. Andersson, J. O., Helander, T., Hoglund, L., Shi, P., & Sundman, B. (2002). THERMO-CALC & DICTRA, Computational Tools for Materials Science. *Calphad*, *26*(2), 273–312.
67. Lin, H., Tsai, W., & Lee, J. (1992). The electrochemical and corrosion behavior of austenitic stainless steel containing Cu, *33*(5), 691–697.
68. Ujiro, T., Satoh, S., Staehle, R. W., & Smyrl, W. H. (2001). Effect of alloying Cu on the corrosion resistance of stainless steels in chloride media. *Corrosion Science*, *43*(11), 2185–2200.

69. Sourisseau, T., Chauveau, E., & Baroux, B. (2005). Mechanism of copper action on pitting phenomena observed on stainless steels in chloride media. *Corrosion Science, 47*(5), 1097–1117.

70. Banas, J., & Mazurkiewicz, A. (2000). The effect of copper on passivity and corrosion behavior of ferritic and ferritic-austenitic stainless steels. *Materials Science and Engineering A*, *277*(1–2), 183–191.

71. Escriba, D. M., Materna Morris, E., Plaut, R. L., & Padilha, A. F. (2009). Chi phase precipitation in a duplex stainless steel. *Materials Characterization*, *60*(11), 1214–1219.

72. Pettersson, N., Pettersson, R. F. A., & Wessman, S. (2015). Precipitation of Chromium Nitrides in the Super Duplex Stainless Steel 2507. *Metallurgical and Materials Transactions A: Physical Metallurgy and Materials Science*, *46*(3), 1062–1072.

73. Fuji Electronic Industrial Co., Ltd. http://sps.fdc.co.jp/whats/whats4.html

74. Chew, K.K. (2012). The corrosion scenario in the human body: Stainless steel 316L orthopedic implants. Natural Science, 4(3), 184–188.

75. Talha, M., Behera, C. K., & Sinha, O. P. (2013). A review on nickel-free nitrogen containing austenitic stainless steels for biomedical applications. Materials Science and Engineering C, 33(7), 3563–3575.

76. Yang, K., & Ren, Y. (2010). Nickel-free austenitic stainless steels for medical applications. Science and Technology of Advanced Materials, 11(1), 14105.

77. Dewidar, M. M., Khalil, K. A., & Lim, J. K. (2007). Processing and mechanical properties of porous 316L stainless steel for biomedical applications. Transactions of Nonferrous Metals Society of China, 17(3), 468–473.

78. Azuma, S., Kudo, T., Miyuki, H., Yamashita, M., & Uchida, H. (2004). Effect of nickel alloying on crevice corrosion resistance of stainless steels. *Corrosion Science*, *46*(9), 2265–2280.

79. Lopez, D. A., Duran, A., & Cere, S. M. (2008). Electrochemical characterization of AISI 316L stainless steel in contact with simulated body fluid under infection conditions. Journal of Materials Science: Materials in Medicine, 19(5), 2137–2144.

80. Evgeny, B., Hughes, T., & Eskin, D. (2016). Effect of surface roughness on corrosion behavior of low carbon steel in inhibited 4M hydrochloric acid under laminar and turbulent flow conditions. Corrosion Science, 103, 196–205.

81. Schmitt, H. G., & Bakalli, M. (2010). Flow-assisted corrosion. Shreir’s Corrosion, (m), 954–987.

82. Malik, A. U., Ahmad, S., Andijani, I., & Asrar, N. (1997). Acid cleaning of some diesel units at Al-Jubail plant, (February 1997), 1575–1618.

83. Buchweishaija, J., & Mkayula, L. (2008). The Effect of Rotation and Temperature on the Inhibition Performance of Cashew (Anacardium Occidentale L.) Nut Shell Liquid on Co2 Corrosion of Carbon Steel. Tjet, 2(2), 121–129. Retrieved from

84. Ballesteros, D. Y. P., Camacho, Y. E. M., & Hernandez, L. V. B. (2016). Evaluation of the synergistic effect of erosion-corrosion on AISI 4330 steel in saline-sand multiphase flow by electrochemical and gravimetric techniques. *International Journal of Electrochemistry*, *2016*, 1–7.

85. Hussein, M. A., Suryanarayana, C., Arumugam, M. K., & Al-Aqeeli, N. (2015). Effect of sintering parameters on microstructure, mechanical properties and electrochemical behavior of Nb-Zr alloy for biomedical applications. *Materials and Design*, *83*, 344–351.

86. Zhang, H. W., Gopalan, R., Mukai, T., & Hono, K. (2005). Fabrication of bulk nanocrystalline Fe-C alloy by spark plasma sintering of mechanically milled powder. *Scripta Materialia*, *53*(7), 863–868.

87. Liu, Z. F., Zhang, Z. H., Lu, J. F., Korznikov, A. V., Korznikova, E., & Wang, F. C. (2014). Effect of sintering temperature on microstructures and mechanical properties of spark plasma sintered nanocrystalline aluminum. *Materials and Design*, *64*, 625–630.

88. Rajendrachari Shashanka, Debasis Chaira, & Dibyendu Chakravarty. (2016). Fabrication of Nano-Yttria Dispersed Duplex and Ferritic Stainless Steels by Planetary Milling Followed by Spark Plasma Sintering and Non-Lubricated Sliding Wear Behaviour Study. *Journal of Materials Science and Engineering B*, *6*(3), 111–125.

89. Oleszak, D., Grabias, A., Pekała, M., Świderska-Środa, A., & Kulik, T. (2007). Evolution of structure in austenitic steel powders during ball milling and

subsequent sintering. *Journal of Alloys and Compounds*, *434–435*(SPEC. ISS.), 340–343.

90. Toor, I. U. H. (2014). Effect of Mn content and solution annealing temperature on the corrosion resistance of stainless steel alloys. *Journal of Chemistry, 2014*.
91. Toor, I.-H., Park, Jk. J., & Kwon, H. (2007). Manganese Effects on Repassivation Kinetics and SCC Susceptibility of High Mn–N Austenitic Stainless Steel Alloys. *Journal of the Electrochemical Society, 154*(9), C494.
92. Stewart, J., & Williams, D. E. (1992). The initiation of pitting corrosion on austenitic stainless steel: on the role and importance of sulphide inclusions. *Corrosion Science*, *33*(3).
93. Kim, J. J., & Young, Y. M. (2013). Study on the Passive Film of Type 316 Stainless Steel. *International Journal of ELECTROCHEMICAL SCIENCE, 8*(2013), 11847–11859.
94. Pardo, A., Merino, M. C., Carboneras, M., Viejo, F., Arrabal, R., & Munoz, J. (2006). Influence of Cu and Sn content in the corrosion of AISI 304 and 316 stainless steels in H2SO4. *Corrosion Science*, *48*(5), 1075–1092.
95. Lai, W. Y., Zhao, W. Z., Yin, Z. F., & Zhang, J. (2012). EIS and XPS studies on passive film of AISI 304 stainless steel in dilute sulfuric acid solution. *Surface and Interface Analysis*, *44*(4), 418–425.
96. Oguzie, E. E., Li, J., Liu, Y., Chen, D., Li, Y., Yang, K., & Wang, F. (2010). The effect of Cu addition on the electrochemical corrosion and passivation behavior of stainless steels. *Electrochimica Acta*, *55*(17), 5028–5035.
97. Kim, M. J., Lee, S. H., Kim, J. G., & Yoon, J. B. (2010). Effect of Manganese on the Corrosion Behavior of Low Carbon Steel in 10 wt. % Sulfuric Acid. *Electrochemical Ssc, 9312*(December), 1–9.
98. Adams, F. V., Olubambi, P. A., Potgieter, J. H., & Van Der Merwe, J. (2010). Corrosion resistance of duplex stainless steels in selected organic acids and organic acid/chloride environments. *Anti-Corrosion Methods and Materials*, *57*(3), 107–117.

Vitae

Name : Farid Munir Abdallah

Nationality : Tanzanian

Date of Birth : 9/5/1987

Email : farid.munir(a)yahoo.com

Address : P.O BOX 22567 Mathuradas, Upanga, Ilala, Dar es salaam, TANZANIA

Academic Background : In 2013, I finished my Bachelor degree from Istanbul Technical University in the field of Metallurgical and material engineering. After that, I worked as a coating inspector with the WorleyParsons Resources & Energy company for 1 years in Mtwara-Dar-es-salaam gas pipeline and plants construction. I have acquired dissimilar experience as well through internship programs in Turkish Airline Maintenance Company in aircraft maintenance department in Istanbul. In January 2015, I joined Master degree in King Fahd University of Petroleum & Mineral in the field of Material engineering. I took several courses such as Advanced Corrosion, Material Characterization, Material Structure and defects, Thermodynamics, Tribology, Corrosion in oil and petrochemical industries and welding which helped me to accomplish my thesis work titled “ Development and Investigations of electrochemical properties of lean Duplex stainless steel alloys”.

RESEARCH ACHIEVEMENTS:

F.M. Abdallah, I.U.H Toor. “Development of an economical Duplex stainless steel for Industrial Applications”. Poster presentation in Middle East Corrosion Conference (Won “ Best Poster” award)